UNIVERSITY of CALIFORNIA
Santa Barbara

A Macroscopic Mechanical Resonator Operated in the Quantum Limit

A dissertation submitted in partial satisfaction of the
requirements for the degree of

Doctor of Philosophy

in

Physics

by

Aaron D. O'Connell

Committee in charge:

Professor Andrew N. Cleland, Chair
Professor John M. Martinis
Professor Andreas Ludwig

December 2010

The dissertation of Aaron D. O'Connell is approved:

Professor John M. Martinis

Professor Andreas Ludwig

Professor Andrew N. Cleland, Chair

December 2010

A Macroscopic Mechanical Resonator Operated in the Quantum Limit

Aaron D. O'Connell

To my parents:

Ralph and Bryna

Acknowledgements

I would like to thank all of my friends for their help. Specifically, Jennifer Dewalt for her support and guidance and Hieu Nguyen for his unrelenting pursuit of knowledge. Also, I would like to thank Arnaud Berube for his assistance in building a xenon difluoride etcher and for helping to measure many mechanical resonators. Of course, this work would not have been possible if it were not for the expertise and instruction of my advisors Andrew N. Cleland and John M. Martinis. Finally, I would like to thank my co-workers, graduate students and post-docs, whose detailed directions made seemingly insurmountable tasks sound easy.

Curriculum Vitæ

Aaron D. O'Connell

Education

2010 (exp.)	Doctor of Philosophy, Physics, University of California, Santa Barbara
2005	Bachelor of Science, Physics and Mathematics, Eckerd College

Honors and Awards

2010	Invited participant of Science Foo Camp 2010 (O'Reilly Media, Nature Publishing Group, Google Inc.)
2005	Natural Sciences Collegium Scholarship and Service Award, Eckerd College, St. Petersburg, Florida
2005	Meacham Mathematics Memorial (M^3) Award, Eckerd College, St. Petersburg, Florida
2005	Pi Mu Epsilon Mathematical Honorary Society

Publications

T. Yamamoto, M. Neeley, E. Lucero, R. C. Bialczak, J. Kelley, M. Lenander, M. Mariantoni, A. D. O'Connell, D. Sank, H. Wang, M. Weides, J. Wenner, Y. Yin, A. N. Cleland, J. M. Martinis. Quantum process tomography of two-qubit controlled-Z and controlled-NOT gates using superconducting phase qubits. *PRB* **82**, 184515 (2010).

Erik Lucero, J. Kelley, R. C. Bialczak, M. Lenander, M. Mariantoni, M. Neeley, A. D. O'Connell, D. Sank, H. Wang, M. Weides, J. Wenner, T. Yamamoto, A. N. Cleland, J. M. Martinis. Reduced phase error through optimized control of a superconducting qubit. *PRA* **82**, 042339 (2010).

Matthew Neeley, Radoslaw C. Bialczak, M. Lenander, E. Lucero, M. Mariantoni, A. D. O'Connell, D. Sank, H. Wang, M. Weides, J. Wenner, T. Yamamoto, Y. Yin, A. N. Cleland, J. M. Martinis. Generation of Three-Qubit Entangled States

using Superconducting Phase Qubits. *Nature* **467**, 570-573 (2010).

R. C. Bialczak, M. Ansmann, M. Hofheinz, E. Lucero, M. Neeley, A. D. O'Connell, D. Sank, H. Wang, J. Wenner, M. Steffen, A. N. Cleland, John M. Martinis. Quantum Process Tomography of a Universal Entangling Gate Implemented with Josephson Phase Qubits. *Nature Physics* **6**, 409-413 (2010).

A. D. O'Connell, M. Hofheinz, M. Ansmann, Radoslaw C. Bialczak, M. Lenander, Erik Lucero, M. Neeley, D. Sank, H. Wang, M. Weides, J. Wenner, John M. Martinis, A. N. Cleland. Quantum ground state and single-phonon control of a mechanical resonator. *Nature* **464**, 697-703 (2010).

H. Wang, M. Hofheinz, M. Ansmann, R. C. Bialczak, Erik Lucero, M. Neeley, A. D. O'Connell, D. Sank, M. Weides, J. Wenner, A. N. Cleland, John M. Martinis Decoherence Dynamics of Complex Photon States in a Superconducting Circuit. *Physical Review Letters* **103**, 3200404 (2009).

H. Wang, M. Hofheinz, J. Wenner, M. Ansmann, R. C. Bialczak, M. Lenander, E. Lucero, M. Neeley, A. D. O'Connell, D. Sank, M. Weides, A. N. Cleland, John M. Martinis. Improving the Coherence Time of Superconducting Coplanar Resonators. *Applied Physics Letters* **95**, 233508 (2009).

Markus Ansmann, H. Wang, Radoslaw C. Bialczak, Max Hofheinz, Erik Lucero, M. Neeley, A. D. O'Connell, D. Sank, M. Weides, J. Wenner, A. N. Cleland, John M. Martinis. Violation of Bell's inequality in Josephson phase qubits. *Nature* **461**, 504-506 (2009).

Matthew Neeley, Markus Ansmann, Radoslaw C. Bialczak, Max Hofheinz, Erik Lucero, Aaron D. O'Connell, Daniel Sank, Haohua Wang, James Wenner, Andrew N. Cleland, Michael R. Geller, John M. Martinis. Emulation of a Quantum Spin with a Superconducting Phase Qudit. *Science* **325**, 722 (2009).

Max Hofheinz, H. Wang, M. Ansmann, Radoslaw C. Bialczak, Erik Lucero, M. Neeley, A. D. O'Connell, D. Sank, J. Wenner, John M. Martinis, A. N. Cleland. Synthesizing arbitrary quantum states in a superconducting resonator. *Nature* **459**, 546-549 (2009).

H. Wang, M. Hofheinz, M. Ansmann, R. C. Bialczak, E. Lucero, M. Neeley, A. D. O'Connell, D. Sank, J. Wenner, A. N. Cleland, John M. Martinis. Measurement

of the decay of Fock states in a superconducting quantum circuit. *Physical Review Letters* **101**, 240401 (2008).

Max Hofheinz, E. M. Weig, M. Ansmann, Radoslaw C. Bialczak, Erik Lucero, M. Neeley, A. D. O'Connell, H. Wang, John M. Martinis, A. N. Cleland. Generation of Fock states in a superconducting quantum circuit. *Nature* **454**, 310-314 (2008).

Nadav Katz, Matthew Neeley, M. Ansmann, Radoslaw C. Bialczak, M. Hofheinz, Erik Lucero, A. O'Connell, H. Wang, A. N. Cleland, John M. Martinis, Alexander N. Korotkov. Reversal of the Weak Measurement of a Quantum State in a Superconducting Phase Qubit. *Physical Review Letters* **101**, 200401 (2008).

Matthew Neeley, M. Ansmann, Radoslaw C. Bialczak, M. Hofheinz, N. Katz, Erik Lucero, A. O'Connell, H. Wang, A. N. Cleland, John M. Martinis. Process tomography of quantum memory in a Josephson-phase qubit coupled to a two-level state. *Nature Physics* **4**, 523-526 (2008).

Aaron D. O'Connell, M. Ansmann, R. C. Bialczak, M. Hofheinz, N. Katz, Erik Lucero, C. McKenney, M. Neeley, H. Wang, E. M. Weig, A. N. Cleland, J. M. Martinis. Microwave Dielectric Loss at Single Photon Energies and milliKelvin Temperatures. *Applied Physics Letters* **92**, 112903 (2008).

Erik Lucero, M. Hofheinz, M. Ansmann, Radoslaw C. Bialczak, N. Katz, Matthew Neeley, A. D. O'Connell, H. Wang, A. N. Cleland, John M. Martinis. High-fidelity gates in a Josephson qubit. *Physical Review Letters* **100**, 247001 (2008).

Matthew Neeley, M. Ansmann, Radoslaw C. Bialczak, M. Hofheinz, N. Katz, Erik Lucero, A. D. O'Connell, H. Wang, A. N. Cleland, John M. Martinis. Transformed Dissipation in Superconducting Quantum Circuits. *Physical Review B* **77**, 180508(R) (2008).

Radoslaw C. Bialczak, R. McDermott, M. Ansmann, M. Hofheinz, N. Katz, Erik Lucero, Matthew Neeley, A. D. O'Connell, H. Wang, A. N. Cleland, John M. Martinis. 1/f Flux Noise in Josephson Phase Qubits. *Physical Review Letters* **99**, 187006 (2007).

Abstract

A Macroscopic Mechanical Resonator Operated in the Quantum Limit

by

Aaron D. O'Connell

We report the experimental results of a superconducting quantum bit coupled to a macroscopic mechanical resonator. The coupled sample was cooled in a dilution refrigerator to $T = 25$ mK. At this temperature, we measured the phonon occupation of the mechanical resonator and found it to be in the quantum ground state with high probability $P_0 > 93$ %. We then excited the mechanical resonator from its ground state $|0\rangle$ to the single phonon state $|1\rangle$ by transferring a single quantum excitation from the quantum bit to the mechanical resonator. Using this ability, we probed the energy lifetime of the mechanical resonator, $T_{1\mathrm{M}} = 6.1$ ns, by monitoring the decay of a single phonon state. Next, we measured the decay of the superposed phonon state $(|0\rangle + |1\rangle)/\sqrt{2}$ in order to extract the phase coherence time $T_{2\mathrm{M}} \approx 2T_{1\mathrm{M}}$. Finally, we explored higher phonon energy levels by directly exciting the mechanical resonator with a classical microwave source, thus creating a mechanical coherent state.

Contents

List of Figures

List of Tables

Chapter 1

Introduction

The theory of quantum mechanics makes a number of predictions that seem to run contrary to common sense. However, these predictions have been experimentally verified again and again. Since quantum theory has been used with a great deal of success to describe the physical world, it stands to reason, then, that the perceived peculiarity must stem from the physical world itself. This is not such strange assertion considering quantum theory was predominantly developed to describe single particle phenomena; mostly in the context of electrons and photons. Since single particles are not readily observable, one should not expect a description of these particles to be subject to the same notions one may have regarding macroscopic objects.

However, since its inception in the early 20^{th} century, there has been a heated

debate over the extent to which quantum mechanics can be applied to objects in our everyday world. This idea is usually conceptualized in the context of cats, specifically, Schrödinger's cat [43]. While we will not go into the details here, the main idea of the thought experiment is to highlight the difficulty faced when attempting to adequately describe the interplay between the seemingly incongruous concepts of quantum and classical mechanics. What was thought at the time, and is arguably still the prevailing notion of our time, was that microscopic objects obey quantum mechanics, macroscopic objects obey classical mechanics (à la the correspondence principle), and quantum coherence is destroyed when the microscopic interact with the macroscopic.

The idea, then, of a superposed macroscopic mechanical object strikes a chord with the imaginative. However, the observation of such macroscopic quantum effects is technically challenging, hindered by the fact that most macroscopic objects are strongly coupled to an environment that masks or destroys quantum behavior. It may turn out that this environmental coupling is the primary factor prohibiting macroscopic objects from displaying quantum behavior as opposed to some fundamental size limitation imposed by quantum mechanics [19, 54]. However, sufficient evidence supporting this claim has yet to be seen.

We have performed a series of measurements on one such sufficiently isolated mode of a macroscopic mechanical object; the fundamental dilatational mode of

a film bulk acoustic resonator (FBAR). The results of these measurements are consistent with the standard quantum description of a harmonic oscillator, the appropriate model for the mechanical resonant mode. Although these measurements constitute the first observations of quantum behavior in a macroscopic mechanical oscillator, such large scale mechanical quantum behavior should be observable in other systems as well. In recent years, there have been a number of experiments, on disparate physical systems, that have produced promising results near the quantum limit [17, 36, 12, 13, 41, 37].

Chapter 2

The state of the art

The goal of measuring a mechanical resonator in the quantum ground state has received much attention in recent years and has helped fuel the rapidly growing field of quantum limited motion detection. The motivation to reach the quantum ground state of a mechanical object is twofold. On one hand, the observation of quantum effects in macroscopic mechanical systems probes some of the fundamental paradoxes of quantum measurement theory, an esoteric goal, and on the other hand, the observation of the mechanical ground state necessitates the use of extremely sensitive displacement sensing, a pragmatic engineering feat. The innate challenges encountered when attempting to observe quantum effects in relatively large mechanical systems have lead researches to pursue a diverse set of experimental approaches. We will examine the criteria necessary for the obser-

vation for non-classical behavior. From there, we will briefly introduce some of the more promising physical systems that may eventually meet all these criterion: Fabry-Pérot cavities formed from micro-mirrors atop flexural resonators, flexural beam resonators parametrically coupled to coplanar wave guide resonators, and laser cooled toroidal micro-resonators.

2.1 Quantum ground state considerations

Historically, it has been possible to model macroscopic mechanical systems entirely within the context of classical mechanics. This is not entirely surprising because mechanical systems are composite structures formed from the interaction of a tremendous number of particles. The quantum to classical transition readily occurs when a given system is strongly coupled to the "large" objects that compose our everyday world, and while it is relatively easy to isolate ions in harmonic traps, it has proven challenging to sufficiently decouple larger mechanical systems.

The basic approach is to first identify a resonant mode of a mechanical system that is well separated in the frequency from the other mechanical modes. Once a particular mode has been chosen, the degree to which this mode is decoupled from the "environment" can be characterized by its quality factor [33],

$$Q = 2\pi \frac{\text{energy stored}}{\text{energy lost per cycle}}. \tag{2.1}$$

For $Q < 1$, quantum effects would be smeared out by rapid energy loss and

associated decoherence. However, for $Q > 1$ the resonator enters the underdamped regime where it is possible to store well defined quantum excitations in the oscillator's phonon number states.

Since the aim here is to observe non-classical effects, ignoring all other factors, it may seem optimal to choose a system with the highest possible Q. In most mechanical systems, it is experimentally found that higher quality factors can be attained with lower resonant frequencies, $Q \sim 1/\Omega_{\mathrm{M}}$, where Ω_{M} is the mechanical resonant frequency [38]. Although it may be tempting to choose a low frequency mechanical mode with correspondingly high quality factor, to do so would overlook a fundamental issue.

Even with weak coupling to the environment, given a sufficient duration of time, the mechanical resonant mode will come into thermal equilibrium with its surroundings. A mechanical resonator in thermal equilibrium at a temperature T, will contain, on average, a phonon number that follows the Bose distribution

$$\langle n \rangle = \frac{1}{e^{\hbar\Omega_{\mathrm{M}}/k_B T} - 1}, \tag{2.2}$$

where $\hbar$ is Plank's constant divided by 2π and k_B is Boltzmann's constant. The corresponding thermal state will act to conceal quantum effects. Therefore, it is necessary to rid the oscillator mode of these thermally induced phonons in order to observe quantum behavior. In other words, before well defined non-classical phonon states can be observed, the mechanical resonator must be in the quantum

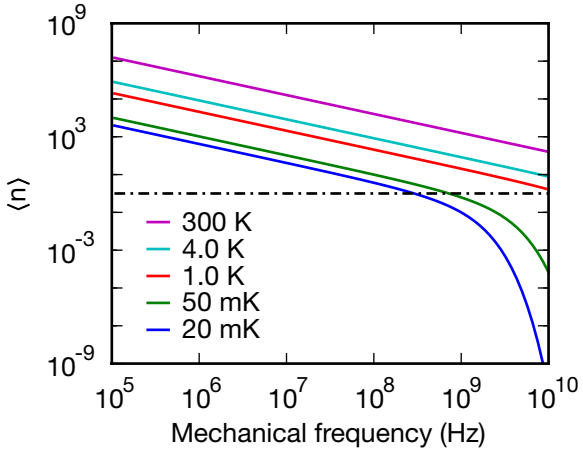

Figure 2.1: The expected phonon number of the mechanical resonant mode is displayed for temperatures that roughly correspond to room temperature, L^4He, L^4He evaporation, salt pillar adiabatic demagnetization, and ^3He dilution refrigeration. The dotted line is drawn at $\langle n \rangle = 1$.

ground state, $\langle n \rangle \ll 1$.

It is clear form the Bose distribution that the quantum ground state can be reached only when the energy level spacing of the harmonic oscillator is significantly greater than the thermal energy $\hbar\Omega_{\rm M} > k_B T$. In Fig. 2.1 we show the expected phonon number for some common cryogenic temperatures. It is readily apparent that for $\Omega_{\rm M} \lesssim 1$ GHz the mechanical mode with not be in the ground state when the system is in thermal equilibrium.

However, even with $\Omega_{\rm M} < 1$ GHz, it is still possible to reach the quantum ground state if additional cooling techniques are employed. Currently, there are two standard avenues pursued when attempting to cool below dilution refrigerator temperatures. Temperatures much below 10 mK can be achieved by attaching

a nuclear demagnetization unit from the cold stage of a standard cryogenic refrigerator. However, this setup is rather complicated and incapable of providing continuous cooling power. The second approach leaves the environmental temperature unchanged while selectively cooling the mechanical resonant mode.

One way to achieve mode selective active cooling is to couple the mechanical resonator to an electromagnetic cavity. Since preparation of non-classical states could be facilitated by such a coupling scheme, active cooling has received more attention than adiabatic demagnetization. The drawback, of course, is that this technique incorporates an electromagnetic cavity and increases the overall complexity of the system. In some systems, coupling between mechanical and electromagnetic resonant modes occurs naturally. However, even when coupling does not occur naturally it may be possible to engineer.

A schematic example of one such specifically engineered system is illustrated in Fig. 2.2 (a). In a configuration of this type, a Fabry-Pérot cavity is created by trapping light between a large fixed mirror and a micron-sized mirror. The micron-sized mirror is physically attached to a mechanical resonator, depicted there as a mass on the end of a spring, so that the position of mechanical resonator determines the optical path length of the cavity. As the mechanical oscillator vibrates, the frequency of the optical mode is modulated, parametrically coupling the two.

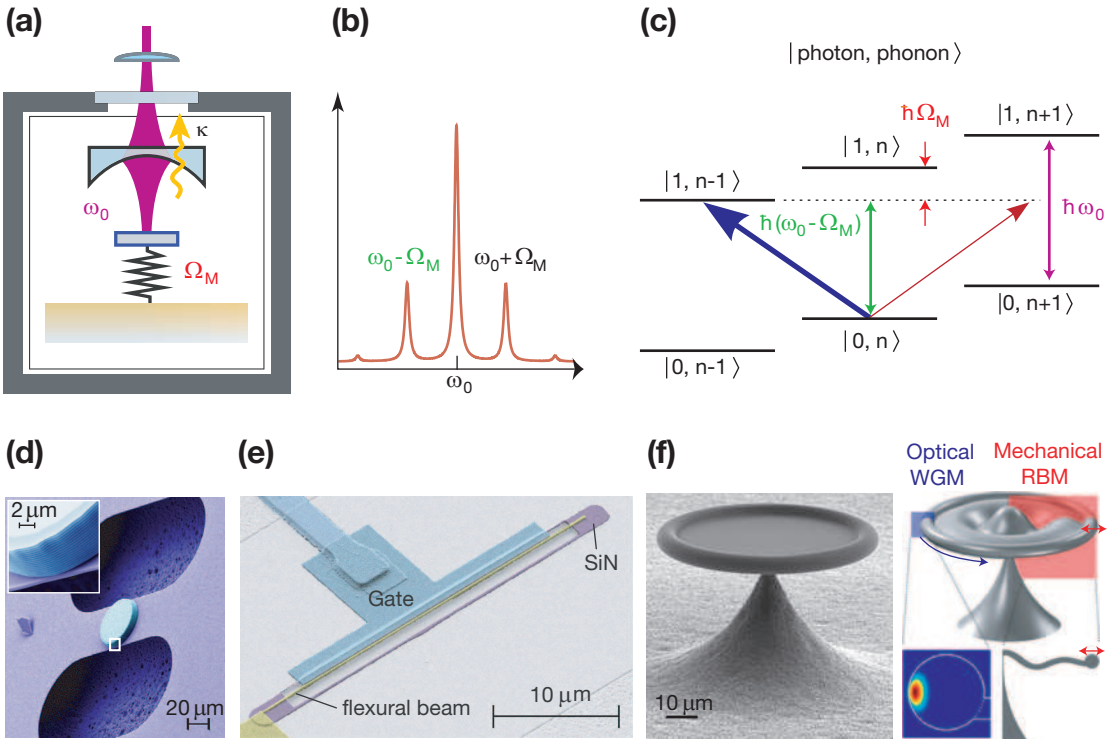

Figure 2.2: **a** the canonical setup depicting a mechanical resonator with oscillation frequency Ω_M attached to a micro-mirror. The micro-mirror constitutes half of the optical cavity formed between it and the larger fixed mirror (adapted from [12]). **b**, spectroscopic response of the optical cavity in the resolved sideband limit. The cavity frequency ω_0 is split from interaction with mechanical resonator (as in [42]). **c**, energy level diagram for coupled optomechanical system. Cooling occurs when a laser drives the lower sideband preferentially causing the system to loose a phonon to the optical mode (adapted from [42]). **d**, SEM of a Bragg micro-mirror attached to a SiN doubly-clamped flexural beam resonator [13]. **e**, SEM of a SiN doubly-clamped flexural beam resonator capacitively couped through the gate electrode to a superconducting microwave resonator [37]. **f**, SEM of a silica toroidal optomechanical resonator (left) and illustration of relevant optical whispering gallery mode and mechanical radial breathing mode (right) [42].

A situation of practical interest arises when the frequency of the mechanical resonator is greater than the optical linewidth κ. When this condition is met, the system is said to be in the resolved sideband limit and spectroscopic determination of the combined resonant modes will produce three distinct frequencies in the optical band as depicted in Fig. 2.2 (b). The center frequency corresponds to the geometrically determined resonance of the optical mode ω_0. The two distinct sidebands at $\omega_0 \pm \Omega_{\mathrm{M}}$ result from the photon-phonon interaction.

Cooling can be achieved by exciting the system with a laser frequency tuned to the lower sideband $\omega_0 - \Omega_{\mathrm{M}}$. Since the laser is detuned from the frequency of the principal optical mode, incident photons will not have enough energy to excite the optical resonance unless accompanied by the simultaneous absorption of a thermal phonon [52, 7]. This scenario is depicted in Fig. 2.2 (c). Each absorption event removes one phonon from the mechanical mode and creates one photon in the optical mode. The loss of phonons from the mechanical mode effectively cools the mechanical oscillator, with a resulting effective temperature determined by the detailed balance between sideband cooling and thermal repopulation [29].

2.2 Experimental attempts

Resolved sideband cooling has been used in a number of recent experiments in order to obtain low phonon populations. In one such experiment, a Bragg micro-

mirror was fabricated atop a doubly clamped flexural beam resonator [12, 13]. As described schematically above, this micro-mirror formed one side of a Fabry-Pérot cavity. A scanning electron micrograph (SEM) of a completed device is shown in Fig. 2.2 (d). The Bragg micro-mirror was composed of 36 alternating layers of Ta_2O_5 and SiO_2, and the flexural beam resonator was formed from SiN that had been released from the underlying substrate with a timed exposure to XeF_2 gas. The mechanical resonant frequency was measured to be $\Omega_M/2\pi = 945$ kHz with a corresponding quality factor of $Q \approx 30,000$ at 5.3 K. By measuring the noise power spectra it was seen that the mechanical mode could be cooled from an initial temperate of 5.3 K to an effective temperature of approximately 1.5 mK, corresponding to an expected phonon state containing $\langle n \rangle = 32 \pm 4$ [12].

Resolved sideband cooling of mechanical modes is not unique to optical cavities. In recent experiments conducted on mechanical resonators coupled to superconducting microwave resonators, very low phonon numbers were observed [47, 37]. A SEM of one such device is shown in Fig. 2.2 (e). Instead of the position of the mechanical resonator changing the path length of an optical cavity, in this configuration, the position of the beam alters the total capacitance of the microwave cavity. Since the resonant frequency of the microwave cavity is proportional to the total capacitance $\omega_\mu \propto 1/\sqrt{C}$, the mechanical motion creates a time-varying capacitance that modulates the microwave resonant frequency. Side-

band cooling is carried out in a similar fashion, where a microwave tone is applied at the lower sideband frequency $\omega_\mu - \Omega_{\rm M}$. The thermal phonons are converted to microwave photons and cooling proceeds as before. An average phonon number $\langle n \rangle = 3.8 \pm 1.3$ was reported for the $\Omega_{\rm M}/2\pi = 6.3$ MHz flexural resonant mode, cooled from an initial environmental temperature of $T = 146$ mK [37] to an effective temperature of approximately 1.3 mK.

In both of the experimental systems discussed so far, the coupling between mechanical resonator and electromagnetic cavity had to be specifically engineered. However, such coupling may naturally arise in some systems, such as the toroidal resonators shown in Fig. 2.2 (f). These resonators were formed from silica and support both high quality optical whispering gallery modes and mechanical radial breathing modes. The toroids were excited by a laser and displayed a sideband resolved spectrum indicating a coupled mechanical resonant mode at $\Omega_{\rm M} = 73.5$ MHz with a corresponding quality factor $Q \approx 30,000$. By exciting the lower side band, the mechanical mode was cooled from an initial temperature of 1.65 K to a final effective temperature of approximately 220 mK, corresponding to a state with on average $\langle n \rangle = 63 \pm 20$ phonons [41].

Chapter 3

The coupled qubit-FBAR approach

Active sideband cooling was a common theme running through the experiments just described. While the use of this technique to cool a mechanical mode to the quantum ground state is a promising future direction, the rate of cooling achieved in the preceding experiments was insufficient to overcome thermal repopulation. Instead of starting with a thermally excited mechanical mode, we took a different approach and focused our efforts on circumventing thermal activation. We sidestepped the issue of selective mode cooling by adapting our experiment to use only proven commercial refrigeration techniques. This was accomplished through the use of high frequency mechanical resonators, with resonant frequencies well into the microwave regime. At temperatures easily reached with a dilution refrigerator, these high frequency mechanical resonators should be found in the

quantum ground state. For example, the Bose distribution predicts an average phonon number of $\langle n \rangle < 10^{-4}$ for a 6 GHz mechanical mode cooled to $T = 25$ mK.

The details of experiments conducted on one such high frequency mechanical resonator coupled to a superconducting phase qubit, as well as a good deal of theoretical background, are to be published in a Springer book on optomechanics, edited by Markus Aspelmeyer, Tobias Kippenberg, and Florian Marquardt. A preprint of this book chapter is presented below and composes the majority of this dissertation. After the presentation of this book chapter, the next chapter of this dissertation completes the story by filling in any relevant details that did not find their way into the book.

Microwave-frequency mechanical resonators operated in the quantum limit

Aaron D. O'Connell and Andrew N. Cleland

Abstract In this chapter, we describe fully an experiment in which the quantum ground state of a mechanical resonator was reached when the structure was cooled in a dilution refrigerator to $T \sim 25$ mK. The resonator had a fundamental dilatational resonance frequency in excess of 6 GHz, so once cooled, the omnipresent bath of thermal phonons was unable to supply enough energy to measurably excite the mechanical resonator out of its quantum ground state. These

results are a direct consequence of the high resonance frequencies obtainable with the class of mechanical resonator used in the experiment, which is known as a film bulk acoustic resonator, or FBAR. In this chapter, we begin by briefly describing the mechanics of bulk acoustic resonance and FBAR structures, and we present a simple electrical circuit model for the resonator. Experimental measurements of this type of mechanical resonator, measured in the classical regime, are then presented. Next, we introduce the Josephson phase quantum bit (qubit), a device which forms the heart of the measurement scheme used to probe the mechanical resonator in the quantum regime, and we describe the coupling mechanism between the qubit and a mechanical resonator. Lastly, we present the experimental measurements of the resonator in the quantum regime, where the qubit was used to both prepare and measure non-classical mechanical states in the resonator.

3.1 Film bulk acoustic resonators

Film bulk acoustic resonators are dilatational-mode mechanical resonators fabricated using piezoelectric materials. Voltages applied to the electrodes on the surface of the resonator cause piezoelectric strain, either dilating or contracting the volume of the resonator. When the voltage is made to oscillate at a frequency corresponding to a natural mechanical resonance of the structure, large and sustained oscillations can be generated. The nature of the piezoelectric ma-

terial means that the converse is also true: A mechanical resonance will generate voltages on the same electrodes, which can be detected externally, allowing one to monitor the state of vibration of the resonator.

These types of structures are of great interest in the telecommunications industry, where they are used to mechanically filter electrical signals. Using mechanical resonators in this fashion provides filtering that is significantly superior to purely electronic filters. Strong coupling between the electrical signal and the mechanical vibration is best achieved with film-like resonators, i.e. structures with large lateral dimensions and small thicknesses, with thin-film metal electrodes applied to the top and bottom surface of the film. The structure is typically driven in a thickness-mode vibration, meaning that the top and bottom surfaces alternately approach and recede from one another, at a frequency that is proportional to the speed of sound in the material, divided by the thickness of the structure. With typical sound speeds of $\sim$ 5 km/s, resonance frequencies in the GHz telecommunications band thus require structures with thicknesses of order 1 μm. For example, the structure depicted in Fig. 3.1 might have a radius r that is a few tens of micrometers, while the thickness of the piezoelectric layer d may be less than a micron. When a voltage is applied across the electrodes, a nearly uniform electric field is formed between the plates, a field that points along the z axis. The piezoelectric material between the plates reacts to the imposed electric field

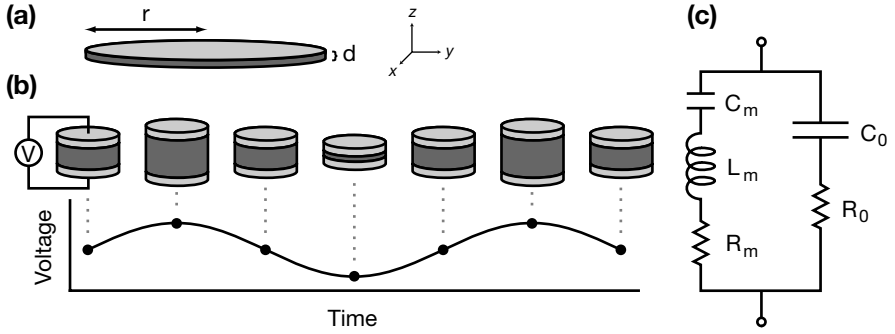

Figure 3.1: Film bulk acoustic resonator geometry, piezoelectric response, and model circuit representation. **a**, idealized geometry of a mechanical resonator, comprising a piezoelectric material of thickness d with infinitely thin metal plates, or electrodes, on both the top and bottom surfaces. **b**, sketch illustrating the dilatational response of the piezoelectric structure to an externally-imposed voltage, which generates an electric field between the electrodes; light gray indicates metal electrodes, while dark gray represents piezoelectric material. The thickness dimension is grossly exaggerated for illustrative purposes, and the metal electrodes are shown here with non-zero thickness. **c**, Equivalent electrical circuit model for mechanical response near the fundamental dilatational mechanical resonance. C_m, L_m, and R_m are the mechanical capacitance, mechanical inductance, and mechanical resistance (representing mechanical energy dissipation), respectively. The electrical branch is composed of a capacitor C_0 representing the geometric capacitance of the structure, and a resistor R_0 representing electrical dissipation with value R_0. The capacitance is given by $C_0 = \epsilon_0 \epsilon A/d$, where A is the area of an electrode, ϵ is the dielectric constant, and ϵ_0 is the permittivity of free space.

by polarizing, which due to the piezoelectric response generates strain (displacement) in the material. The electric field thus causes the piezoelectric to expand or contract proportional to the sign and magnitude of the field. This is illustrated in Fig. 3.1 **b** for the quasi-static case of a slowly varying voltage.

We would like to examine the electrical response that occurs near a mechanical resonance. Consider a piezoelectric material contained within ideally thin

electrodes, vibrating at angular frequency ω close to a mechanical resonance frequency. The electrical impedance Z across the metal plates can be determined in the dissipation-free limit by solving the electro-mechanical equations of motion for an acoustic angular frequency ω to yield [38],

$$Z(\omega) \approx \frac{1}{i\omega C_0}\left(1 - \frac{\tan(\omega d/2\nu)}{\omega d/2\nu} k_{\text{eff}}^2\right) \tag{3.1}$$

where C_0 is the geometric capacitance of the structure, k_{eff}^2 is the so-called piezoelectric coupling efficiency, typically of order 0.01, and ν is the speed of sound in the piezoelectric medium. The impedance is a strong function of frequency for frequencies near the mechanical thickness resonances $\omega_n/2\pi = n\nu/2d$, where $n = 1, 3, 5, ...$, with the magnitude of the impedance $|Z|$ displaying a minimum and a maximum near these frequencies; the even-number modes do not appear because their symmetry does not generate an electrical signal for symmetrically placed electrodes, as in Fig. 3.1. In this model equation, the maxima occur exactly at the mechanical resonance frequencies ω_n, which correspond to the surface-stress free normal thickness modes of the structure. A local maximum of the impedance corresponds to a mode in which energy can be stored (essentially, the storage of energy increases the voltage needed to store more energy, thus in a sense increasing the impedance as the energy increases). The fundamental dilatational mode occurs for $n = 1$ and is termed the "parallel resonance" frequency. The parallel resonance occurs at

$$\frac{\omega_p}{2\pi} = \frac{\nu}{2d}, \tag{3.2}$$

and is analogous to the fundamental half-wave mode of a stiff vibrating wire with two free ends, held at its midpoint. The frequency of this resonance can be adjusted by changing the thickness d of the structure. For a piezoelectric material such as aluminum nitride (AlN), with a sound speed $\nu \approx 11$ km/s, resonant frequencies above 1 GHz are achievable for thicknesses less than 5 μm.

The impedance magnitude $|Z|$ has a second feature, a zero, at frequency ω_s (the "series resonance" frequency, as explained below). This frequency is given by the transcendental equation

$$\frac{\tan(\omega_s d/2\nu)}{\omega_s d/2\nu} k_{\text{eff}}^2 = 1, \tag{3.3}$$

for which a closed-form solution does not exist. However, as the piezoelectric coupling efficiency k_{eff}^2 is much smaller than unity, the impedance can be approximated near its first pole by

$$Z \approx \frac{1}{i\omega C_0}\left(1 - \frac{8}{\pi^2 - (\omega d/\nu)^2} k_{\text{eff}}^2\right). \tag{3.4}$$

This leads the approximate expression for the series-resonance frequency

$$\frac{\omega_s}{2\pi} \approx \frac{\nu}{2d}\left(1 - \frac{8}{\pi^2} k_{\text{eff}}^2\right)^{1/2}. \tag{3.5}$$

The minimum in $|Z|$ occurs at a slightly lower frequency than the maximum at the parallel-resonance frequency.

It is interesting to note that in the dissipation-free limit, the piezoelectric coupling efficiency can be determined from the two resonant frequencies ω_p and

ω_s by combining Eq. (3.2) and Eq. (3.3):

$$k_{\text{eff}}^2 \approx \frac{\pi\omega_s/2\omega_p}{\tan\left(\pi\omega_s/2\omega_p\right)} \approx \frac{\pi^2}{4}\left(\frac{\omega_p - \omega_s}{\omega_p}\right), \tag{3.6}$$

indicating that the frequency spacing between the two resonances is proportional to the coupling efficiency.

Although Eq. 3.1 is useful for finding the resonance frequencies and evaluating their relation to the coupling efficiency, a lumped-element circuit model that gives a good approximation to the electrical impedance near resonance is quite invaluable. To the trained eye, Eq. 3.4 is the impedance of a static capacitor C_0 in parallel with mechanically-determined components that are inductive and capacitive. Such a model has been developed, and is dubbed the 'modified Butterworth-van Dyke" (MBVD) model [18, 39]. This circuit model for a piezoelectric resonator, including dissipation by way of resistors that represent mechanical and electrical losses in the actual structure, is shown in Fig. 3.1 (c). We will first examine the dissipation-free limit, where the resistances are set to zero. Thus, the dissipation-free circuit consists only of the static capacitor C_0, the electrical branch, in parallel with an electrical equivalent mechanical inductance L_m and capacitance C_m, which make up the mechanical motional branch of the circuit.

As it is not obvious that this lumped-element circuit model captures the main aspects of the impedance of the device as represented by Eq. 3.1, we now turn

our attention to showing that there exists a simple mapping between the two representations for frequencies near the fundamental resonance frequency ω_p. The impedance of the lossless lumped circuit is given by

$$Z_{LE} = \frac{1}{i\omega C_0}\left(1 - \frac{C_m}{C_0 + C_m - C_0 C_m L_m \omega^2}\right), \tag{3.7}$$

which is clearly of the same form as Eq. 3.4. To relate the circuit elements to the mechanical properties, we can use the requirement that both the Eq. 3.4 and Eq. 3.7 should exhibit resonances at the same frequencies. The series and parallel resonances of the circuit model occur at

$$\omega_p = \frac{1}{\sqrt{L_m C_m \frac{C_0}{C_0 + C_m}}}, \text{ and} \tag{3.8}$$

$$\omega_s = \frac{1}{\sqrt{L_m C_m}}. \tag{3.9}$$

Equating these relations to those derived from Eq. 3.4, we find the relations

$$C_m = C_0 \frac{8}{\pi^2} k_{\text{eff}}^2 \left(1 - \frac{8}{\pi^2} k_{\text{eff}}^2\right), \text{ and} \tag{3.10}$$

$$L_m = \frac{d^2}{8 k_{\text{eff}}^2 \nu^2 C_0}. \tag{3.11}$$

Hence, we can easily prescribe the electrical circuit element values from our knowledge of the electromechanical properties (note the capacitance C_0 is determined already from the geometry).

Thus far, we have ignored dissipation in our description. However, any physical FBAR will exhibit both mechanical and electrical losses. Since the motional

branch of the circuit strongly dominates the impedance near a mechanical resonance, the series resistor R_m is included in the motional branch to account for mechanical dissipation. Far from the mechanical resonant frequency, the impedance of the FBAR approaches that of a capacitor with value C_0. Dielectric dissipation in this capacitor is incorporated into the electrical branch with the resistor R_0. The entire MBVD circuit model, including these dissipative elements, is shown in Fig. 3.1 (c). The electrical response of this circuit will exhibit resonances similar to those previously derived. However, dissipation will suppress the amplitude of $|Z|$ near a resonant response. In addition, the exact frequency of a resonant response will be slightly altered. In general the electrical impedance, even on resonance, will arise from the combined interaction of all the circuit elements, and must be treated accordingly.

3.2 Mechanical resonator characterization

Piezoelectric mechanical resonators of the FBAR design described above were fabricated with aluminum metal electrodes and sputtered polycrystalline AlN as the piezoelectric. The multi-layer structure was patterned on the surface of a high-resistivity ($> 10,000$ Ω-cm) 100 mm diameter silicon wafer using interspersed lithographic processing steps of sputtered metal and dielectric deposition, optical lithography, and plasma etching; all patterning was done by etching previously-

deposited layers, with no "lift-off" steps in the process. No electron beam lithography was needed to produce the structures. After processing the full wafer, individual dies were diamond-saw cut from the wafer, each containing one resonator structure. To mechanically isolate the mechanical FBAR structure from the substrate, the chip was then exposed to xenon difluoride gas in a custom-built vacuum system that isotropically removed the silicon beneath the resonator structure. This process generated an undercut that entirely released the mechanically-active part of the structure. The resonator was left suspended over the remaining substrate, supported by the co-fabricated aluminum lead wires and underlying AlN. A scanning electron micrograph (SEM) of a completed device is shown in Fig. 3.2.

Visible in the image is the mechanically-active metal/piezoelectric/metal stack, enclosed by the white dashed rectangle. The structure was supported by the two metal beams leading from the left edge of the stack to the bulk substrate and the external circuitry. In addition to providing mechanical support, the metal beams also served as electrical connections to each electrode of the resonator stack. One of these beams was connected to the circuit electrical ground, while the other was connected to the microwave feed line shown at the top of the image. This microwave drive line was electrically separated from wire bond pads by two on-chip interdigitated capacitors, C_x, which were used to isolate the resonant structure

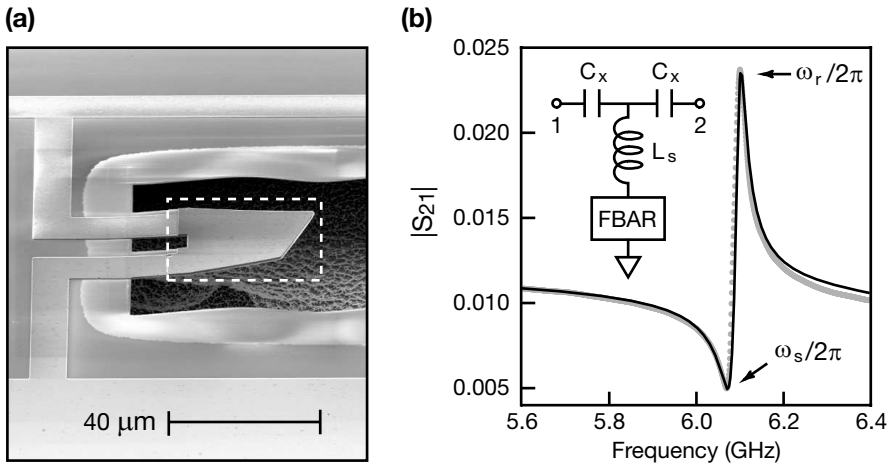

Figure 3.2: Electron micrograph and electrical measurement of a mechanically-suspended resonator. **a**, mechanically active part of the resonator highlighted by white dashed rectangle. The resonator is supported on the left by the metal leads that form the two electrical connections, with their underlying AlN. **b**, electrical transmission measurement (gray points), with a fit to the equivalent circuit model (black line) using the (inset) circuit model. The transmission from port 1 to port 2 (inset) was measured with a calibrated network analyzer. C_x denotes the capacitance of external capacitors associated with the wiring between the measurement cables and the device, and L_S represents the stray inductance of the wiring leads [31].

from the 50 Ω impedance of measurement lines (see inset circuit).

To characterize the electrical response of the FBAR, the chip was wire-bonded with 25 μm diameter wire bonds to an aluminum microwave mount and connected to a microwave vector network analyzer. The normalized complex transmission S_{21} from port 1 to port 2 was then measured as a function of frequency, producing the characteristic response illustrated in the main panel of Fig. 3.2 (b). There are two prominent features in the data: First, the dip in transmitted signal at $\omega_s/2\pi = 6.07$ GHz is attributed to the low-impedance series resonance. At the slightly higher frequency, $\Omega_{\rm M}/2\pi = \omega_p/2\pi = 6.10$ GHz, the transmission takes on its maximal value due to the high-impedance, parallel mechanical resonance, which we have labeled $\Omega_{\rm M}$ as this is the relevant mechanical mode for our "optomechanical" experiments.

To extract the equivalent circuit parameters from the spectroscopic data, the measured transmission response was fit to the electrical model shown inset to Fig. 3.2 (b). The capacitance C_0 was calculated using the lithographically defined area A of the electrodes, the estimated thickness of the AlN layer, $d = 330$ nm, and an approximate dielectric constant $\epsilon_r \approx 10$ for AlN [9], so that $C_0 = \epsilon_0 \epsilon A/d = 0.19$ pF. The stray inductance was estimated to be $L_s \approx 1$ nH, obtained by examining the device response over a broad range of frequencies. The frequencies of the resonant responses, along with the equations linking the reactive elements in the

circuit model, yielded a mechanical capacitance $C_m = 0.655$ fF, a mechanical inductance $L_m = 1.043$ μH, and a piezoelectric coupling coefficient $k_{\text{eff}}^2 \approx 1.2\%$ [39, 28]. The overall amplitude of the transmission indicates that the external capacitors were $C_x \approx 37$ fF. The amplitude of the resonant response gives the resistive values $R_m = 146$ Ω and $R_0 = 8$ Ω. The quality factor of the parallel resonant mode is correspondingly $Q \approx 260$.

We performed a number of experiments that ensured that the measured resonance feature was indeed mechanical in nature, and not a spurious electrical resonance. One such test was conducted by physically removing the mechanically-active part of the device and measuring the remaining circuitry. When measured in this configuration, no resonant response was seen. This result indicates that the response shown in Fig. 3.2 (b) is due (in part, at least) to the presence of the suspended structure highlighted in Fig. 3.2 (a). We also fabricated an identical chip but using amorphous silicon nitride (SiN), a non-piezoelectric insulator material, in place of the piezoelectrically-active AlN. When this device was measured in the same manner, no resonant response was visible, an indication that the piezoelectric material is needed to generate an electrical response.

Two additional series of tests were performed, which more directly illustrate the mechanical nature of the resonance. The first series of tests was conducted to explore changes in the resonant response when the mechanically-active part

of the resonator was not fully suspended. As previously mentioned, the active part of the resonator is released from the underlying Si substrate with XeF_2 gas, which isotropically removes silicon from around and eventually underneath the resonator. If instead of allowing the XeF_2 to fully undercut the resonator, a shorter exposure to the reactive gas is used, then the active part of the resonator will remain partially connected to the substrate by a pillar of silicon. If the chip is then exposed to additional doses of XeF2 gas, the diameter of the pillar will be reduced in size, freeing a greater area of the active part of the structure.

Using this technique, one particular sample was measured electrically a number of times, each time after increasing the degree of mechanical release. The FBAR structure was first measured prior to any exposure to XeF_2, thus while still fully connected to the substrate. No resonant response was observed. Without removing the device from the microwave measurement mount, the resonator was then exposed to XeF2 gas for a time long enough to release approximately 30% of the area beneath the resonator. The sample was then re-measured and the characteristic resonant response began to emerge. The FBAR was then exposed to XeF_2 and measured two more times. Each time the resonant response grew in amplitude as illustrated in Fig. 3.3 (a). The trend toward greater amplitude indicates that the measured response is most likely mechanical in origin, and indicates that the structure is releasing less and less acoustic power into the substrate

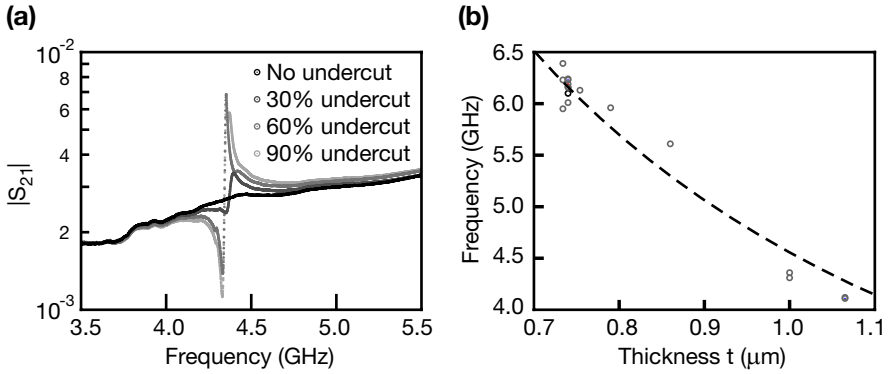

Figure 3.3: Measured mechanical dissipation and frequency dependence of a FBAR structure. **a**, electrical resonant response of a resonator measured with varying degrees of mechanical release. A larger amplitude response indicates less mechanical dissipation. **b**, mechanical resonant frequencies $\Omega_M/2\pi$ obtained by measuring resonators with differing overall thicknesses t. The darker datum at 6.1 GHz corresponds to the resonator shown in Fig. 3.2.

as its connection to the substrate is weakened.

To further test the nature of the electrical resonance, we fabricated a series of resonators with varying overall thicknesses t (including both the electrode thickness as well as the AlN thickness d). Eq. 3.2 indicates that for greater thicknesses, the resonant frequency should decrease, approximately as $1/t$. This prediction is in stark contrast with what one would expect for a purely electrical resonator composed of the parallel connection of an inductor L and a capacitor C, where the capacitance is due to the geometric capacitance of the FBAR structure. In that case, one would have $C \propto 1/t$, so that the resonance frequency would scale as $1/\sqrt{LC} \propto \sqrt{t}$.

The spectroscopically determined mechanical resonance frequencies $\Omega_M/2\pi$ for

a set of unique resonators with different thicknesses t are shown in Fig. 3.3 (b). The reported thickness correspond to the approximate total thickness of the resonator, where the thickness was varied from resonator to resonator by changing the deposition time of the AlN layer. It is clear from the data that the overall trend is toward lower resonant frequency with increased thickness, as expected. The data can be reasonably fit with the expected form $\Omega_{\mathrm{M}}/2\pi \approx \nu/2t$, which produces the dashed line shown in Fig. 3.3 (b). The speed of sound was fit to $\nu \approx 9100$ m/s, and while not unreasonable, we emphasize that this oversimplifies the behavior of these composite structures. As a side note, the variation in the resonant frequency observed for a given thickness value was most likely due to variations in the actual thickness of the structure. As the deposited films tend to become thinner toward the edge of the substrate wafer, resonator dies taken from different locations on the same wafer will have varying thicknesses and thus resonant frequencies. The range of resonance frequencies we observe are within the range expected for this thickness variation.

These check experiments indicate quite strongly that we have realized FBAR structures with fundamental mechanical resonance frequencies in the few GHz band. These frequencies provide promise for the observation of quantum effects in such resonators when cooled to temperatures below 1 K. However, although the high resonance frequency of these structures avoids the typical limitation set by

the presence of a strongly decohering thermal bath, these resonators do suffer from an inherent drawback: As the mechanical resonance frequency is increased, the quality factor of the resonance is seen to decrease correspondingly. A commonly used figure of merit that takes this effect into consideration is the f-Q product, the product of the resonance frequency and the quality factor. Here we find f-Q products of order 10^{12} Hz, within the range seen for most "high quality" mechanical resonators. However, as the FBARs measured here did not exhibit exceptionally high f-Q products, the high mechanical frequency comes at the expense of a lower quality factor.

The low quality factor has a direct implication for quantum measurements, as the lifetime T_1 for a single quantum of energy can be related to the classical quality factor, through $T_1 = Q/\omega_p$. Here we can estimate for our FBAR structures an energy lifetime of $T_1 = 6.7$ ns. A quantum operation on the mechanical resonator must be completed within this time before the quantum state is destroyed by dissipation. Creating and measuring quantum states in such a short time window requires careful planning, and in particular, a very strong coupling between the system used to create and measure the quantum state and the mechanical resonator. The approach we chose to use, to strongly couple a system that can quantum control and quantum measure a mechanical resonator, was to couple the resonator to an electrical equivalent of an atom: A superconducting Josephson

phase qubit [24].

3.3 Josephson junctions as tunable two level systems

A Josephson junction is created when a superconducting path is interrupted by a weak link that restricts the flow of electrons (or, in the superconducting state, Cooper pairs) to quantum tunneling processes. For example, Josephson junctions are often formed by separating two superconducting metal electrodes with a thin insulating barrier, as depicted in Fig. 3.4, commonly referred to as a superconductor-insulator-superconductor (SIS) junction. Although SIS junctions were used for all the experiments to be described below, Josephson junctions can be formed in other ways as well. Most notable are the superconductor-normal metal-superconductor (SNS) junction, where the superconductor is interrupted by a short normal metal section, sufficiently short that superconducting Cooper pairs can sometimes survive the passage through the normal metal (proximity effect); and the microbridge junction, where a very narrow constriction in a superconducting wire limits the flow of Cooper pairs [48].

The physics of the Josephson junction has received much interest since its discovery in 1962 [16]. This is is part due to two remarkable characteristics of

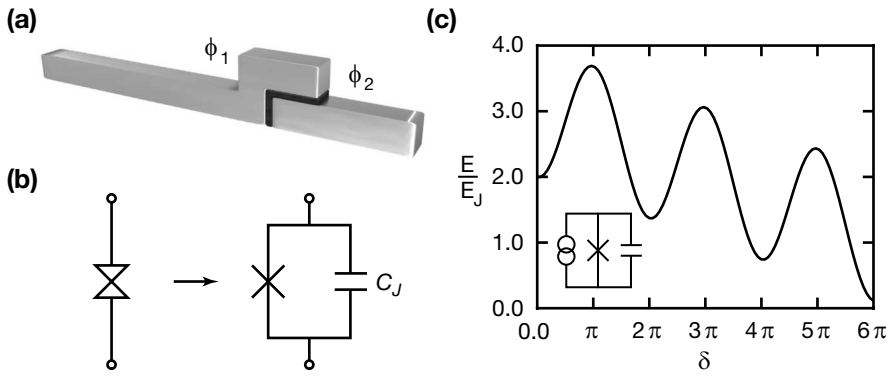

Figure 3.4: A Josephson junction: SIS junction geometry, capacitively shunted circuit model, and "washboard" potential energy diagram. **a**, perspective drawing of an overlap Josephson junction. The two superconducting metal wires are separated by an insulating barrier, shown in black; this is typically a very thin (1 nm) metal oxide layer. The phase of the Ginzburg-Landau superconducting wavefunctions in each superconducting wire is represented by $\phi_{1,2}$. **b**, circuit representation of a Josephson junction, where the hourglass symbol (left side) represents the physical Josephson junction and is equivalent to an ideal Josephson junction shunted by a capacitor (right). **c**, potential energy model for a current-biased Josephson junction. The biasing current determines the overall tilt of the potential, while the oscillations are due to the dc Josephson effect. The local, periodic minima exist for bias currents I less than the critical current I_0.

these unique devices, as described mathematically by the dc and ac Josephson relations. The dc Josephson relation describes the flow of a supercurrent through a junction, even in the absence of an applied voltage. The dc Josephson relation states that the supercurrent I_J through an SIS junction can be written as

$$I_J = I_0 \sin \delta, \tag{3.12}$$

where I_0 is the junction's critical current, and $\delta = \phi_2 - \phi_1$ is the gauge-invariant phase difference between the Ginzburg-Landau wavefunctions on either side of the junction's insulating barrier (in the absence of a magnetic field). If a voltage V is applied across the Josephson junction, the phase difference across the junction is predicted by the ac Josephson relation to evolve in time according to

$$\dot{\delta} = \frac{2e}{\hbar} V. \tag{3.13}$$

Combining these two relations implies that a voltage-biased junction will have a supercurrent that oscillates in time at a frequency $2eV/h$.

In order to exploit these novel properties, Josephson junctions have been incorporated into a wide array of superconducting circuits [1, 8, 20, 4, 27, 49, 25, 3, 21, 32, 53, 2, 6, 44, 50]. For illustrative purposes, we will examine a simple circuit, the current-biased Josephson junction. It is easiest to proceed by first generating an equivalent electrical circuit representation for the Josephson junction. Up to this point in our discussion, we have treated the junction in the quasi-static limit, where we have ignored the self-capacitance of the junction's geometric structure.

As the junction is formed from two metal electrodes separated by a dielectric insulator, we expect that the resulting geometric capacitance will be electrically in parallel to the junction itself. A model circuit for a single junction is illustrated in Fig 3.4 (b), where the junction has been split into an ideal junction, represented by an cross, and its parallel capacitance C_J. The ideal junction is assumed to follow exactly the two Josephson relations.

With this circuit model, we can analyze the effect of adding a time-varying current bias I to the circuit, as depicted in the insert of Fig. 3.4 (c). Kirchhoff's current law dictates that

$$I = C\dot{V} + I_J. \tag{3.14}$$

Using the dc Josephson effect to relate I_J to the phase difference δ, and recognizing that the voltage across the capacitor must be the same as that across the ideal junction, we can combine this equation with the ac Josephson relation to yield

$$\frac{\hbar}{2e}C\ddot{\delta} + I_0 \sin(\delta) - I = 0. \tag{3.15}$$

This is an equation of motion very similar to a classical particle moving in one dimension, with mass proportional to the capacitance C, interacting with a force proportional to $I - I_0 \sin\delta$. We can cast this equation of motion into the Lagrangian formalism and find the associated kinetic and potential energies

$$T = \left(\frac{\hbar}{2e}\right)^2 \frac{C}{2}\dot{\delta}^2 \tag{3.16}$$

$$U(\delta) = -E_J\left(\cos\delta + \frac{I}{I_0}\delta\right), \tag{3.17}$$

where we have introduced the parameter $E_J = \hbar I_0/2e$, the Josephson energy. Here we see that our fictitious particle has mass $M = (\hbar/2e)^2 C$, moving in the potential $U(\delta)$. A plot of the potential energy is shown in Fig. 3.4 (c) for an applied current bias I far from the critical current I_0. This potential is commonly referred to as the tilted washboard potential, with tilt proportional to the applied current. The potential displays 2π-periodic local minima for $I < I_0$, at which point the minima become inflection points. For bias currents $I \geq I_0$, the particle is free to run down the potential and the junction switches from the superconducting state to the "voltage state," where the junction develops a dc voltage.

To form the classical Hamiltonian, we first find the canonical momentum conjugate to the coordinate δ, [11]

$$p = \frac{\partial L}{\partial \dot{\delta}} = \left(\frac{\hbar}{2e}\right)\frac{\hbar C}{2e}\dot{\delta} = \frac{\hbar}{2e}Q, \tag{3.18}$$

where $Q = C\dot{\delta}$ is the charge on the capacitor. The classical Hamiltonian is then

$$H_{\rm cl} = p\dot{\delta} - L = \frac{Q^2}{2C} - E_J\left(\cos\delta + \frac{I}{I_0}\delta\right). \tag{3.19}$$

If we now recognize that the capacitor has a Cooper pair charging energy of $E_C = (2e)^2/2C$, then we can rewrite the Hamiltonian as [51] as

$$H_{\rm cl} = E_C N^2 - E_J\left(\cos(\delta) + \frac{I}{I_0}\delta\right), \tag{3.20}$$

where $N = Q/2e$ is the number of Cooper pairs.

The classical Hamiltonian can now be quantized. Following the customary prescription, we define the quantum operators $\hat{p}$ and $\hat{\delta}$ and impose the commutation

relation

$$[\hat{\delta}, \hat{p}] = i\hbar. \tag{3.21}$$

The coordinate representation of the momentum operator is then

$$\hat{p} \rightarrow -i\hbar \frac{\partial}{\partial \delta}, \tag{3.22}$$

which produces the coordinate representation for the quantum Hamiltonian,

$$\hat{H} \rightarrow -E_C \frac{\partial^2}{\partial \hat{\delta}^2} - E_J \left(\cos \hat{\delta} + \frac{I}{I_0} \hat{\delta} \right), \tag{3.23}$$

The solution to the time-independent Schrödinger equation using this Hamiltonian will produce quantized energy levels (within the potential local minima) because we have ignored dissipation in the previous description. Although these energy eigenstates can be solved for directly, we instead examine a harmonic approximation that captures the qualitative behavior of the lowest-lying energy levels, as illustrated in Fig. 3.5 (a). For small current bias, the shape of the potential minima can be well-approximated by that of a harmonic oscillator. The energy eigenstates of the harmonic oscillator are determined by the curvature of the potential function; in this approximation, this curvature is related to the plasma frequency ω_{plasma}, defined as [10]

$$\omega_{\text{plasma}} \equiv \sqrt{\frac{U'' \,|_{\text{min}}}{M}} = \frac{\sqrt{2E_C E_J}}{\hbar} \left(1 - \frac{I^2}{I_0^2} \right)^{1/4}. \tag{3.24}$$

The plasma frequency is current-bias dependent, with its maximum value at zero bias current. Eq. 3.24 is a good approximation for the energy level spacing

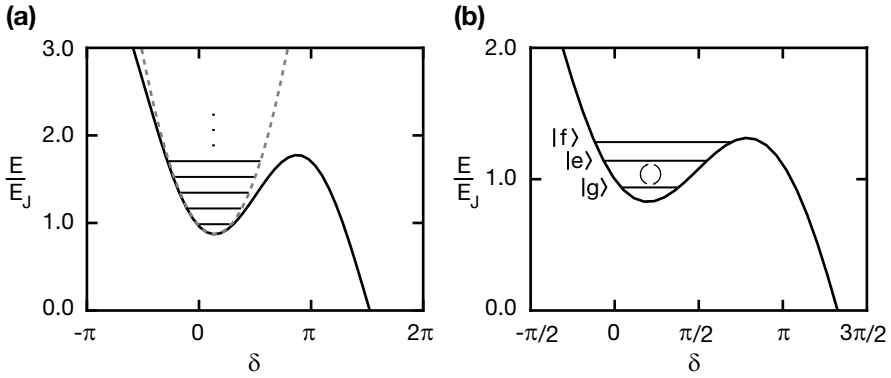

Figure 3.5: Harmonic approximation and eigenstates of the washboard potential. **a**, the dashed line overlay is a harmonic approximation to the local minimum. The evenly spaced energy levels are qualitative representations of the harmonic eigenstates. **b**, lowest energy levels of a local minimum (other eigenstates not shown). The nonuniform spacing arises from the nonlinearity of the potential. The two lowest-lying levels of a local minimum, the ground state $|g\rangle$ and the first excited state $|e\rangle$, form the qubit states.

for a junction biased far from the critical current I_0. However, as the bias current approaches I_0, the actual shape of the potential becomes increasingly anharmonic. This anharmonicity results in a reduced number of energy levels, whose energy spacing, and thus transition frequency, decreases with level number, as shown in Fig. 3.5 (b). Thus, in a local minimum, the ground state $|g\rangle$ to excited state $|e\rangle$ transition can be addressed separately from the higher energy levels, as long as the microwave signal used to stimulate transitions is carefully selected in frequency and careful pulse shaping is used [23]. The two-state manifold $|g\rangle$ and $|e\rangle$ forms the qubit computational basis.

3.4 Coupling a qubit to a mechanical resonator

A straightforward way to strongly couple a Josephson qubit to a piezoelectric mechanical resonator is to place the resonator so that it is electrically in parallel with the Josephson junction. Using the modified Butterworth-van Dyke model for the FBAR resonator, we can design circuits as shown in Fig. 3.6. The two circuits shown there will clearly support two resonant modes: One mode is primarily associated with the qubit itself (here we are implicitly approximating the qubit by its harmonic, that is linear, approximation), and the second mode is primarily attributed to the mechanical resonator. Fig. 3.6 (a) shows a circuit representation for the coupling scheme we have just described, where we have replaced the Josephson element with a tunable (linear) inductor, such that the L_q-C_q resonance reproduces the qubit $|g\rangle \leftrightarrow |e\rangle$ oscillation frequency. Note that the use of linear circuit elements implies that we can only perform single quanta coupling analysis, as the linear circuit will not reproduce the behavior of higher energy excitations.

The classical coupling strength between the two resonant modes in Fig. 3.6 (a) can be found by examining the electrical admittance between the circuit nodes separated by the qubit inductor L_q:

$$Y = \frac{1}{Z_{L_q}} + \frac{1}{Z_{C_q}} + \frac{1}{Z_{C_0}} + \frac{1}{Z_{C_m} + Z_{L_m}}, \tag{3.25}$$

where Z_x is the impedance of element x. The resonant modes are found by solving for the frequencies where the admittance goes to zero. The positive solutions to

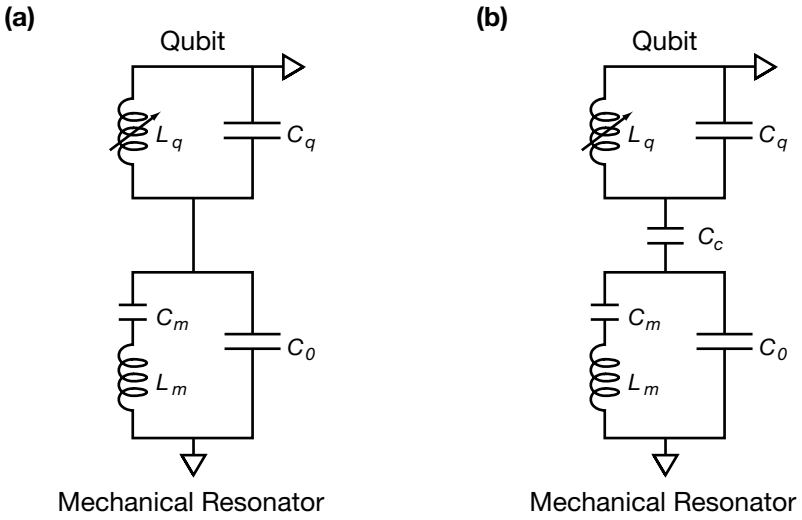

Figure 3.6: Directly and capacitively coupled qubit-FBAR circuit representations. **a**, the tunable inductor L_q and fixed capacitance C_q represent the qubit. The qubit is directly connected to a FBAR, which is modeled by the modified Butterworth-van Dyke circuit in the dissipation free limit. **b**, a coupling capacitor can be used to decrease, and control, the electrical connection between qubit and FBAR.

the resulting biquadratic equation are

$$\omega_{\pm} = \sqrt{\frac{-B \pm \sqrt{B^2 - 4AC}}{2A}}, \tag{3.26}$$

where $A = C_m(C_0 + C_q)L_qL_m$, $B = -C_mL_m - (C_0 + C_m + C_q)L_q$, and $C = 1$.

In the limit of small qubit inductance (thus higher qubit frequency), and for qubit and FBAR with quite different self-resonant frequencies, these solutions take on the limiting forms

$$\omega_+^L \rightarrow \frac{1}{\sqrt{L_q(C_0 + C_q)}}, \text{ and} \tag{3.27}$$

$$\omega_-^L \rightarrow \frac{1}{\sqrt{L_mC_m}}. \tag{3.28}$$

We can interpret the limiting form for ω_+^L as a qubit mode that resonates at the angular frequency $1/\sqrt{L_qC_{q,\text{eff}}}$ with re-normalized capacitance $C_{q,\text{eff}} = C_0 + C_q$. Likewise, the limiting form for ω_-^L can be attributed to the mechanical resonant frequency at $\omega_r = 1/\sqrt{L_mC_m}$. Now, using the fact that the qubit inductance L_q can be tuned, we can change the upper frequency ω_+^L, and in particular tune the qubit frequency towards the mechanical resonance ω_-^L. Adjusting L_q to make the two frequencies equal corresponds to the frequency that generates on-resonance coupling between qubit and resonator; this is analogous to a system of two different harmonic oscillators, coupled by a weak spring, and tuning the mass of one of the oscillators to bring its frequency equal to that of the other oscillator. This condition is colloquially referred to as the frequency for which the two modes are

"on resonance".

As the frequency of the qubit mode is tunable with respect to the fixed mechanical frequency, the amount by which their limiting forms Eq. (3.27) differ is called the qubit frequency de-tuning, or simply the de-tuning, $\Delta = \omega_+^L - \omega_-^L$. When the two modes are on resonance, $\Delta = 0$. However, the frequency difference between the full forms of the two modes, Eq. 3.26, is always nonzero, even at zero de-tuning, due to what in quantum mechanics is often called "level avoidance"; here we are seeing its classical representation. In fact, the frequency difference, $\Omega = (\omega_+ - \omega_-)_{\Delta=0}$, evaluated at $\Delta = 0$, is a measure of the coupling strength between the modes, $\Omega = 2g_0/\hbar$, where g_0 is the classical coupling strength, which corresponds in the quantum limit to the single-quanta coupling strength.

The coupling strength can be solved for analytically. The general solution for the difference between the positive roots of a biquadratic equation is given by

$$\omega_+ - \omega_- = \sqrt{-\frac{B + 2\sqrt{AC}}{A}} \tag{3.29}$$

For $\Delta = 0$ we find

$$\Omega = (\omega_+ - \omega_-)_{\Delta=0} = \sqrt{\frac{1}{L_m C_{q,\text{eff}}}}, \tag{3.30}$$

where we have used the fact that $L_q = C_m L_m / C_{q,\text{eff}}$ on resonance. Thus, if $C_{q,\text{eff}}$ is held fixed, we see that the coupling strength depends only on the mechanical inductance L_m. This implies that larger-area FBARs with the same film thicknesses t will be more strongly coupled to the qubit, and the area of the FBAR

can be adjusted to obtain the desired coupling.

However, relying on the size of the resonator to set the coupling strength may prove inconvenient if the desired resonator size is difficult to realize in practice. To further control the coupling between qubit and mechanical resonator, a coupling capacitor may be added to the circuit, as shown in Fig. 3.6 (b). A similar analysis indicates that the two limiting modes are on resonance when $L_q = C_{m,\text{eff}} L_m / C_{q,\text{eff}}$, where $C_{q,\text{eff}} = C_q + C_0 C_c (C_0 + C_c)^{-1}$ and $C_{m,\text{eff}} = C_m (C_0 + C_c)/(C_0 + C_c + C_m)$. The frequency separation between the mode frequencies on resonance, and thus the coupling strength, is modified by the coupling capacitance to become

$$\Omega_C = \frac{C_c}{C_0 + C_c} \sqrt{\frac{1}{L_m C_{q,\text{eff}}}}. \tag{3.31}$$

We see that the general form is preserved, and we can now adjust the coupling strength via the coupling capacitor C_c as well as through the FBAR parameters.

3.5 Qubits as quantum transducers

Although cooling a mechanical resonator to its quantum ground state is not a trivial procedure, for the discussion that follows we will assume this has already been achieved. The next clear challenge is to excite the ground-state resonator into a non-classical state. However, the method needed to produce such states is not readily apparent. The use of classical excitation pulses to drive a harmonic oscil-

lator will generate coherent states, whose subsequent behavior is indistinguishable from those of a purely classical oscillator: The simple harmonic oscillator, which is the appropriate model for a single harmonic resonance, is always in the correspondence limit between classical and quantum mechanics [26].

To illuminate this point, it is useful to outline the process that creates a coherent state. When a harmonic oscillator, initially in its ground state $|0\rangle$ (where here we represent the oscillator state in terms of its quantum number, or Fock state basis $|n\rangle$), is excited by an on-resonance classical force, the state of the system gradually increases its amplitude in the first excited $|1\rangle$ state. However, as soon as the resonator obtains any probability amplitude to be found in $|1\rangle$, the excitation will begin to promote that population to the second excited state $|2\rangle$, as the $|1\rangle \leftrightarrow |2\rangle$ transition frequency is identical to the $|0\rangle \leftrightarrow |1\rangle$ transition, a consequence of linearity. The resultant state will be a superposition of partially excited phonon number states $|0\rangle$, $|1\rangle$, $|2\rangle$. A measurement of the energy of the oscillator will, for the ideal coherent state, yield phonon number probabilities

$$\mathrm{P}_n(a) = \frac{a^n e^{-a}}{n!}, \tag{3.32}$$

where a is the average phonon number, and n is the index for the Fock state $|n\rangle$. Classical signals can only generate coherent states of this form, and do not reveal the underlying quantum structure of the oscillator's behavior.

Instead of exciting the mechanical resonator directly, we chose to use the ex-

traordinarily strong nonlinearity displayed by the Josephson qubit, so that effectively the qubit serves as a "classical-to-quantum transducer". As the qubit can be manipulated in a way that only involves its lowest two energy levels $|g\rangle$ and $|e\rangle$, and the mode of excitation depends on the phase of the excitation signal, purely classical excitations can be used to completely quantum-control the qubit state. A qubit initially in $|g\rangle$ can be controllably excited, by an on-resonance, calibrated amplitude and duration classical microwave pulse, to the final state $|e\rangle$. At this point, further excitation will force the qubit to emit energy into the excitation field and return to its ground state $|g\rangle$. The state dynamics for a microwave-frequency classical current bias $I_{\rm rf}$, resonant with the $|g\rangle \leftrightarrow |e\rangle$ transition, are described by the Rabi formula [40]

$$\mathrm{P}_e(t) = \sin^2\left(\frac{I_{\rm rf}\chi_{eg}E_J}{\hbar I_0}t\right), \tag{3.33}$$

where $\mathrm{P}_e(t)$ is the qubit excited state probability, and χ_{eg} is the dipole matrix element between states $|g\rangle$ and $|e\rangle$ [10]. Classical radiation alone is sufficient to place the qubit in any state on the Bloch sphere, provided the phase, amplitude and duration of the pulse are properly chosen [46].

Since Josephson qubits can be placed into well-defined quantum states using classical excitations, they provide an ideal means for quantum control of a harmonic oscillator, such as a mechanical resonator. Producing a non-classical state in the mechanical resonator now becomes a two-step process. First, one creates

an arbitrary qubit state using a classical excitation, with the qubit well de-tuned from the resonator to minimize interactions. Second, one transfers the quantum state to the mechanical resonator, by bringing the qubit into frequency-resonance with the resonator in a carefully controlled fashion, and then waiting as the excitation transfers from qubit to resonator. This is completely analogous to the classical transfer of energy that occurs between two coupled harmonic oscillators when one is excited: The classical "beating" described in elementary classical mechanics is the classical description of what here is the equivalent quantum process. As mentioned previously, the transfer time for the excitation (in both the quantum and classical systems) must be shorter or, at most, of the same order as the mechanical oscillator's energy relaxation time. For the FBAR resonators described above, this time is only several nanoseconds. Since the transfer time is inversely proportional to the coupling strength Ω_C, strong qubit-FBAR coupling is required.

The quantum dynamics of the capacitively-coupled qubit-FBAR system are most easily understood by casting the full Hamiltonian into the form of the Jaynes-Cummings model Hamiltonian (see [5]):

$$\frac{\hat{H}}{\hbar} = -\frac{\omega_q}{2}\hat{\sigma}_z + \Omega_{\mathrm{M}}\hat{a}^\dagger\hat{a} - i\frac{\Omega_C}{2}\left(\hat{a}\hat{\sigma}_- - \hat{a}^\dagger\hat{\sigma}_+\right). \tag{3.34}$$

In the Jaynes-Cummings Hamiltonian, written here in the rotating wave approximation, the qubit is represented by the first term, which is that of a two-level

system with tunable transition frequency $\omega_q/2\pi$, where $\hat{\sigma}_z$ is the qubit z operator. The second term corresponds to the mechanical resonator, which takes on the standard form of a harmonic oscillator with energy level transition frequency $\Omega_{\rm M}/2\pi$, and $\hat{a}^\dagger$ and $\hat{a}$ are the resonator phonon raising and lowering operators. The last term of the Hamiltonian expresses the qubit-mechanical resonator coupling, where $\hat{\sigma}_-$ and $\hat{\sigma}_+$ are the qubit raising and lower operators, respectively [10]. The rotating wave approximation is valid when the qubit-resonator coupling is much smaller than the mechanical transition frequency, $\Omega \ll \Omega_{\rm M}$ [45].

If a quantum state $\alpha|g\rangle + \beta|e\rangle$ is created in the qubit, it can be subsequently transferred to the mechanical resonator by tuning the qubit $|g\rangle \leftrightarrow |e\rangle$ transition frequency into resonance with the mechanical resonator frequency $\Omega_{\rm M}$. If we label the probability amplitudes C_{qr} for the basis state $|qr\rangle$ of the coupled system, i.e. a state is given by $|\psi\rangle = C_{g0}|g0\rangle + C_{g1}|g1\rangle + C_{e0}|e0\rangle + C_{e1}|e1\rangle$ (here including only the two lowest resonator Fock states $|0\rangle$ and $|1\rangle$), then the dynamics of the system are described by the set of equations [10]

$$c_{g0}(t) = \alpha, \tag{3.35}$$

$$c_{g1}(t) = \beta\frac{\Omega_C}{\Omega(\Delta)}\sin\left(\frac{\Omega(\Delta)t}{2}\right)e^{-i\Delta t/2}, \tag{3.36}$$

$$c_{e0}(t) = \beta\left[\cos\left(\frac{\Omega(\Delta)t}{2}\right) + i\frac{\Delta}{\Omega(\Delta)}\sin\left(\frac{\Omega(\Delta)t}{2}\right)\right]e^{i\Delta t/2}, \text{ and} \tag{3.37}$$

$$c_{e1}(t) = 0. \tag{3.38}$$

Here $\Delta = \omega_q - \Omega_{\rm M}$ is the de-tuning and $\Omega(\Delta) = \sqrt{\Omega_C^2 + \Delta^2}$ is the Rabi vacuum

frequency. In Fig. 3.7 (a) we plot the time evolution for the initial qubit state $|e\rangle$ (i.e. $\alpha = 0, \beta = 1$), with the qubit transition frequency exactly on resonance with the mechanical resonator, $\Delta = 0$. The resonator is initially in the ground state, but after a quarter of a swap period, $\Omega_C t = \pi/2$, the qubit and mechanical resonator are maximally entangled, with an equal probability to find either in the excited state. The state transfer from qubit to mechanical resonator is complete after a time $t = \pi/\Omega_C$, which places the resonator in the quantum state $|1\rangle$ and leaves the qubit in the ground state. The energy quantum is returned to the qubit (up to a phase) if the interaction is allowed to proceed to $t = 2\pi/\Omega_C$. For a more general state with both α and β non-zero, the same process occurs, with the resonator in the swapped state $\alpha|0\rangle + \beta|1\rangle$ after a time $t = \pi/\Omega_C$, and the state being completely returned to the qubit after a time $t = 2\pi/\Omega_C$.

If the qubit and mechanical resonator are not exactly on resonance, i.e. for non-zero de-tuning, then the state transfer will still take place, but with a higher frequency $\sqrt{\Omega_C^2 + \Delta^2}$, and with a reduced maximal transfer probability $\Omega_C^2/\left(\Omega_C^2 + \Delta^2\right)$. We have illustrated this dependence on de-tuning by plotting the probability to find the qubit in the excited state $P_e = |C_{e0}|^2$, shown in Fig. 3.7 (b). The light portions of the plot correspond to the quantum state being primarily found in the qubit, while the dark portions indicate a preferentially excited mechanical resonator $P_1 = 1 - P_e$, from conservation of probability. Of course, in any real

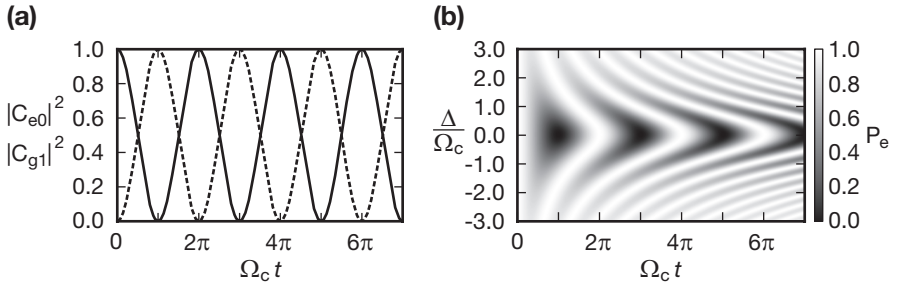

Figure 3.7: Qubit-mechanical resonator probabilities on resonance and for variable de-tunings. **a** shows the on-resonance time evolution of the excited state probability for the qubit, $|C_{e0}|^2$ (solid line), and the $|1\rangle$ state probability for the resonator $|C_{g1}|^2$ (dashed line), for the initial state $|e0\rangle$. **b** shows the time evolution of the qubit $|e\rangle$ state probability P_e as for the same time evolution, but for different de-tunings Δ. The trace for $|C_{e0}|^2$ in **a** is the same as the evolution for P_e in **b** for $\Delta = 0$.

system, energy loss and phase decoherence will cause the system to relax, so the oscillations become less pronounced as time proceeds.

3.6 Quantum ground state and single phonon control

Now that we have constructed the theoretical tools needed to understand the quantum interaction between a qubit and a mechanical resonator, we can turn our attention to the results we obtained for our experimental implementation of this system. An image and circuit representation for the experimental device is shown in Fig. 3.8, where, for clarity, we have not included dissipative elements for

the qubit. In this device, a flux-biased Josephson junction qubit (phase qubit) was used instead of the idealized current-biased Josephson qubit we discussed earlier. In the phase qubit, the effective bias current is produced using an on-chip flux bias coil, mutually coupled to the inductor L_B which is connected across the Josephson junction. This change means that the inclined "washboard potential" of the current-biased junction is replaced by a larger parabolic shape with superposed washboard oscillations, but the local behavior (in one of the metastable wells) remains effectively identical. In addition, because better qubit performance is obtained with small-area Josephson junctions, an additional shunting capacitor C_S is added to adjust the qubit resonant frequency to the desired microwave range of 4 GHz$< \omega_q/2\pi <$ 8 GHz.

There are slight changes in the dynamics of the flux-biased Josephson qubit in comparison with the current-biased version. Although the additional capacitance can be thought of as just an increased mass $M = (\hbar/2e)^2(C_J + C_S)$, the additional linear inductor, as mentioned above, changes the overall shape of the washboard potential by incorporating a term that is quadratic in the phase coordinate. This eliminates the "running" non-zero voltage states, and forms the double-well potential depicted in Fig. 3.8 (c). Properly biased, the left well includes the qubit state manifold, while the right well contains many lower-energy states. The two wells are separated by approximately 2π in the phase coordinate, which corresponds to

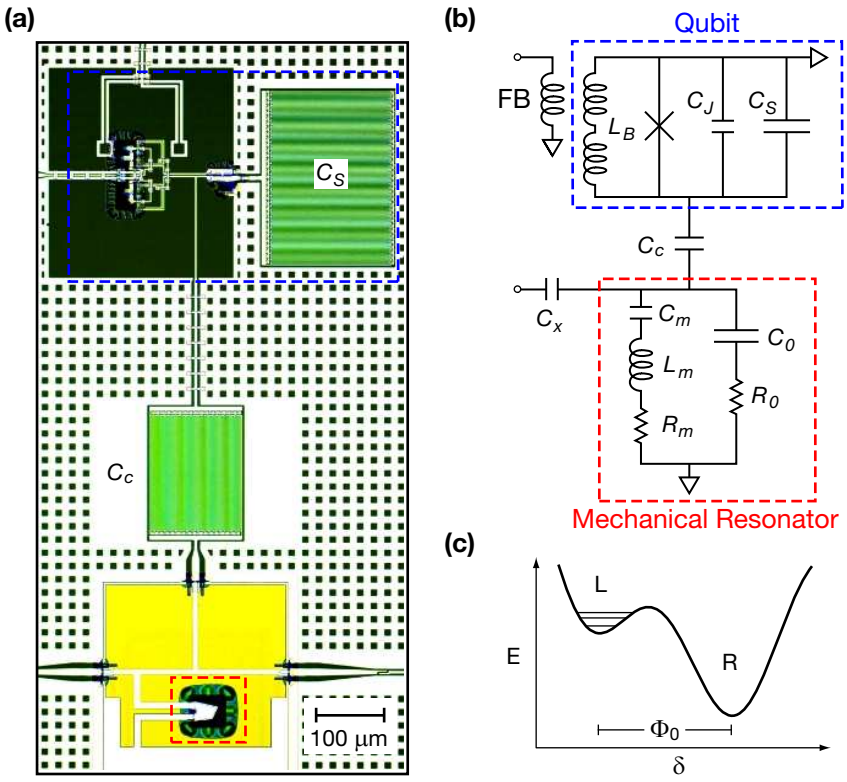

Figure 3.8: Optical micrograph and circuit representation of coupled qubit-mechanical resonator. **a**, the qubit at the top of the micrograph is contained within the blue dashed line. The Josephson junction is barely visible in the middle of the highlighted area and is shunted by an inductor to the left and an interdigitated capacitor to the right. A wire connects the qubit to an interdigitated coupling capacitor C_c, shown in the middle of the image. At the bottom of the image a mechanically-suspended FBAR is surrounded by the red dashed box. All circuit components are surrounded by an electrical ground plane. **b**, Lumped-element circuit representation showing the capacitively-shunted Josephson junction in parallel with a gradiometric inductor L_B and a capacitance C_S resulting from the interdigitated inductor. The qubit is capacitively-coupled to the FBAR, which here is represented by the modified Butterworth-van Dyke model. **c**, double well potential energy of the phase qubit with left well, L, and right well, R. The three lowest lying energy levels of the left well are depicted schematically. The phase difference between left and right well corresponds to an approximate difference of one flux quanta threading the qubit loop.

approximately one flux quantum Φ_0 through the enclosing inductance.

The qubit is initialized by adjusting the flux bias until the phase "particle" is located in the left well, where in time it relaxes to the (metastable) ground state $|g\rangle$ of that well. This ground state, and the next higher energy level $|e\rangle$ in the left well, form the qubit manifold, with their energy level spacing dependent on the bias flux (instead of on the bias current). High-frequency microwave pulses can be applied through the flux bias line to prepare the qubit in any desired superposition of these states. In general, a sequence of these pulses, along with slower qubit frequency-tuning pulses, determines the quantum evolution of the qubit state, either by directly altering the state or by allowing the qubit to interact with the resonator. Once a pulse sequence is complete, a measurement of the qubit is performed by tilting the potential well with the external flux bias just enough so that the excited state $|e\rangle$ will preferentially tunnel from the left well into the right well, while the ground state $|g\rangle$ will remain in the left well. An on-chip superconducting quantum interference device (SQUID) reads out the measurement by detecting the flux threading the qubit loop, projectively differentiating between finding the phase particle in the left or right well. This procedure yields a 90-95% visibility between the excited and ground state. The probability P_e that the qubit was in its $|e\rangle$ state just before measurement can be evaluated by repeating the entire process many (~ 1000) times, and averaging the results.

The coupled qubit-mechanical resonator sample shown in Fig. 3.8 (a) was mounted in an aluminum box, attached to the mixing chamber of a dilution refrigerator, and cooled to the refrigerator base temperature of $T \approx 25$ mK. At this temperature, both the qubit and mechanical resonator should contain less than one energy quantum, as the inequality $\hbar\omega \gg k_B T$ is easily satisfied for typical qubit and resonator frequencies of a few GHz. Previous experiments on phase qubits have shown that the qubit is very reliably in its ground state at this temperature, and our aim in the next section is to demonstrate that the mechanical resonator is in its quantum ground state as well.

The first measurement is to determine the resonant frequencies of the combined system. This was performed using qubit spectroscopy, as illustrated in Fig. 3.9. For all measurements, the qubit was always first initialized to a $|g\rangle \leftrightarrow |e\rangle$ transition frequency $\omega_q/2\pi = 5.44$ GHz, by setting the qubit flux bias to what we term the "operating bias", which we also used as the zero reference for the flux bias. Qubit spectroscopy was performed by pulsing the qubit dc flux away from the operating bias, and illuminating the qubit with microwaves at some frequency for 1.0 μs. After tuning the (excited) qubit back to the operating bias, the qubit was measured, from which the excited state probability P_e could be determined (as described above). For a given microwave drive frequency, a substantial increase in qubit excited state probability was observed only when the qubit transition fre-

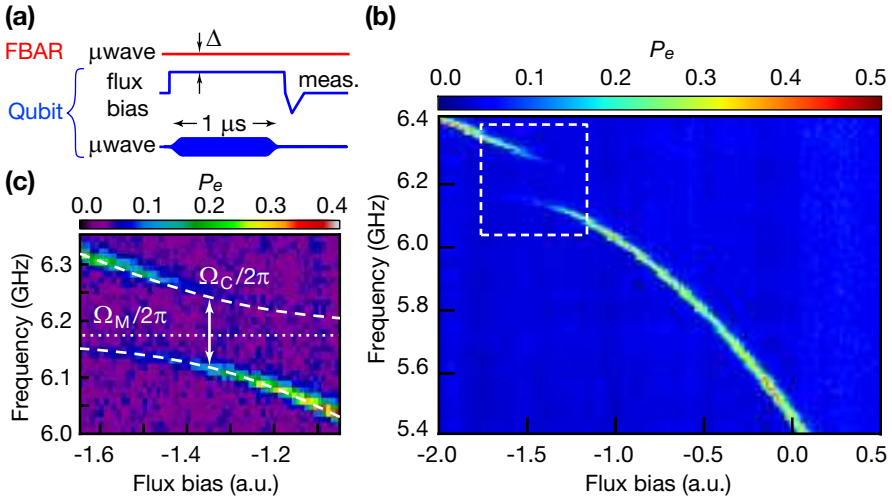

Figure 3.9: Qubit spectroscopy: pulse sequence, qubit excited state probability, and detail of the avoided level crossing. **a**, the qubit, initially in its ground state $|g\rangle$, is moved away from its operating bias and illuminated with microwaves for 1.0 μs. The qubit is then returned to the operating bias and measured. This experiment is repeated while varying both microwave frequency and flux bias tuning. **b**, the probability for the qubit to be measured in the excited state, P_e, is maximal when the $|g\rangle \leftrightarrow |e\rangle$ energy level transition is resonant with the microwave drive. The distinct splitting enclosed in the white dashed box is due to the qubit-FBAR interaction. **c**, detail of **b** highlighting the avoided-level crossing with a fit to the model (upper and lower dashed lines). The horizontal dotted line indicates the frequency of the mechanical resonator $\Omega_M/2\pi$. The coupling strength $\Omega_C/2\pi = 124$ MHz between qubit and resonator was determined from the minimum frequency difference between the two curves.

quency was resonant with the driving field. For non-resonant driving frequencies, the qubit remained in the ground state. Thus, by repeating the experiment while varying both the qubit flux bias and the microwave drive frequency, the resonant modes of the coupled system can be mapped out.

The avoided-level crossing, enclosed by the white dashed rectangle in Fig. 3.9 (b), is characteristic of two interacting resonant systems, and here arises from the

interaction between the qubit and the mechanical resonator. The splitting occurs from the interaction and hence the hybridization of the quantum states of the qubit and resonator, leading to the splitting seen in the qubit transition frequency as a function of bias. A detailed view of this behavior is shown in Fig. 3.9 (c), where the fixed mechanical resonant frequency is indicated by the dotted line at $\Omega_{\mathrm{M}}/2\pi = 6.175$ GHz. The dashed white lines were produced by fitting the data to the classical circuit model described above. The minimum frequency difference between the modes is $\Omega_C/2\pi = 124$ MHz and indicates an energy transfer time (Rabi swap time) between the qubit and mechanical resonator of approximately 4 ns.

We exploited the strong qubit-resonator coupling to verify that the mechanical resonator was indeed in its quantum ground state. The general idea is to use the qubit as a "quantum thermometer" able to detect any non-zero state occupation in the system. If, for example, the mechanical resonator was not in the ground state, then some of that energy would transfer to the qubit when the qubit and resonator are brought into frequency resonance. Measuring that the qubit has a non-zero excited probability would imply that the mechanical resonator was not in the ground state, while a lack of qubit excitation would indicate that the FBAR was indeed in the quantum ground state.

We used two pulse sequences to measure the effective temperature of the res-

onator, as shown in Fig. 3.10 (a). As depicted in the upper pulse sequence, the qubit, initially in its ground state $|g\rangle$, was brought to a frequency de-tuning Δ from the mechanical resonance frequency and left there for 1.0 μs. The qubit was then returned to its operating bias and measured. The probability P_e of measuring the qubit in its excited state as a function of de-tuning Δ is shown in Fig. 3.10 (b) (blue points). The lower pulse sequence shown in Fig. 3.10 (a), was used to place a bound on the dynamic range of the qubit. In this pulse sequence, after interacting with the mechanical resonator, the qubit was returned to its operating bias, but just prior to measurement the ground and excited state probabilities were swapped by applying a microwave π-pulse. The results are shown in Fig. 3.10 (b) by the black data points.

During the interaction, the qubit and mechanical resonator will come into thermal equilibrium, and the qubit excited state population will then reflect any elevated population in the resonator excited states, modulated by the strength of the interaction between the resonator and qubit, and by the qubit and resonator coupling to the thermal bath, as parameterized by their respective energy lifetimes. The numerical simulations include this physics. However, no change in qubit population was seen, even near zero de-tuning where the interaction is the strongest. The lack of a peak (dip) in the qubit excited state probability for the blue (black) data indicates that the mechanical resonator had no measurable

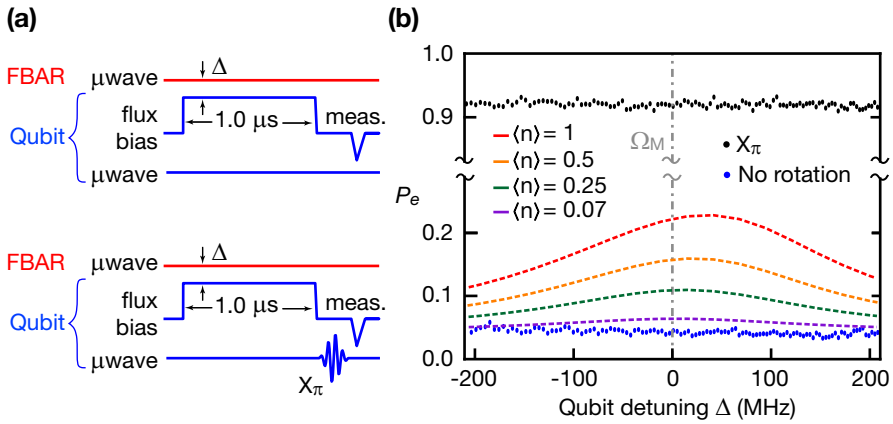

Figure 3.10: Quantum ground state: pulse sequences and experimental data **a**, the qubit, initially in $|g\rangle$, was tuned to within Δ of the mechanical resonator and allowed to interact with the mechanical resonator for 1.0 μs. The qubit was then returned to its operating bias and measured. The experiment was repeated for a range of de-tunings. In the lower pulse sequence, an additional microwave π-pulse was used to swap the ground and excited state populations prior to measurement. **b**, qubit excited state probability without (blue points) and with (black points) the additional population-swapping π-pulse. The dashed lines are numerically simulated qubit probabilities, in which the mechanical resonator was maintained in a thermal state of $\langle n \rangle$ phonons during the qubit interaction process. The lack of a peak in the blue data points around zero de-tuning, and the lack of a dip in the black data points, which from the simulations would be evident even for a very small number of residual phonons $\langle n \rangle$, indicates that the mechanical resonator is with quite high probability (better than 93%) in its quantum ground state $|0\rangle$.

thermal energy to transfer to the qubit. The degree to which the resonator was in the quantum ground state was determined from dynamic quantum simulations to be $P_0 > 93\%$, with a corresponding average phonon number $\langle n \rangle < 0.07$.

With the assurance that the mechanical resonator was indeed in its quantum ground state, our focus shifted toward demonstrating quantum control of the mechanical resonator. We were able to use the qubit as a quantum transducer, generating and measuring a single phonon in the resonator, by applying the pulse sequence shown in Fig. 3.11 (a). The qubit, initially in $|g\rangle$, was promoted to its excited state with a microwave π-pulse (defined as the pulse that exchanges the populations of the $|g\rangle$ and $|e\rangle$ states, i.e. here exciting the qubit to its $|e\rangle$ state). The qubit was then biased to bring its transition frequency toward that of the mechanical resonator, and held at a de-tuning Δ for a variable time τ. Finally, we returned the qubit to its operating bias and measured its excited state probability P_e.

The expected oscillatory behavior, corresponding to the quantum state swapping between qubit and mechanical resonator, can be seen clearly in Fig. 3.11 (b). The oscillations occur at the correct Rabi swap frequency, and display the expected Lorentzian dependence on detuning. There is very rapid decay of the oscillations, due to the very limited energy lifetime of the resonator and the qubit. The asymmetry in the magnitude of the probabilities around $\Delta = 0$ arise from the

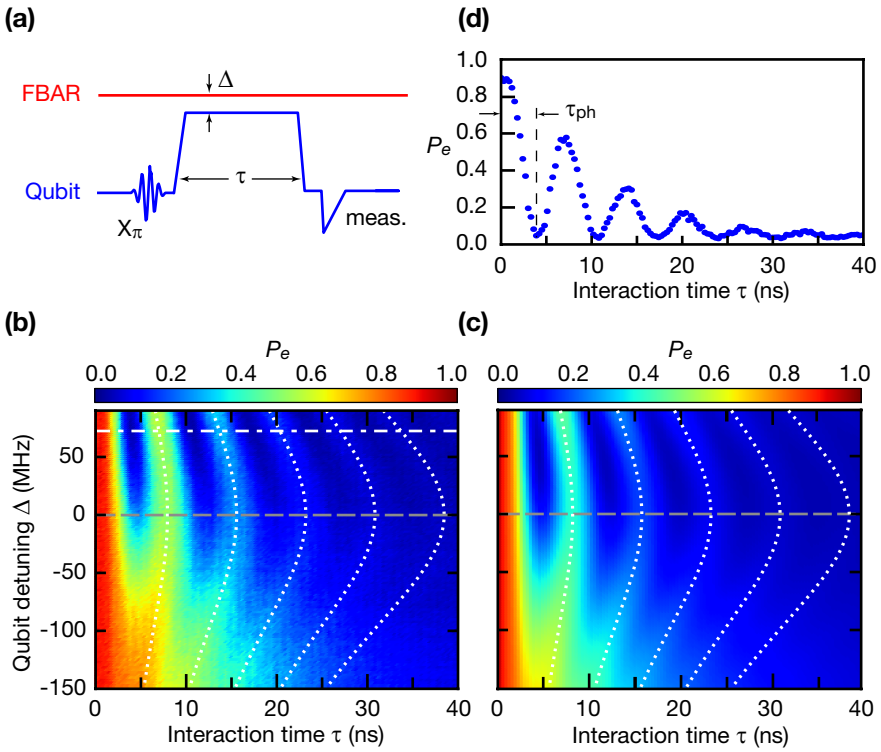

Figure 3.11: Excited mechanical resonator states: pulse sequence, quantum simulation, and experimental data. **a**, pulse sequence in which the qubit is first promoted to $|e\rangle$ by a π-pulse, then allowed to interact with the mechanical resonator at a de-tuning Δ for a variable time τ, before being returned and measured at its operating bias. **b**, measurement of qubit excited state probability P_e as a function of de-tuning and interaction time, showing a single quantum excitation oscillating between the qubit and the mechanical resonator. The dotted white lines show the expected Lorentzian dependence. The gray dashed line indicates the mechanical resonance frequency. **c**, numerical simulation of the data in **b**, for a qubit initially in its $|e\rangle$ state interacting with a mechanical resonator, with the measured qubit and mechanical resonator parameters. **d**, qubit excited state probability for de-tuning $\Delta = 72$ MHz, indicated by the white dashed line slice of the experimental data shown in **b**. After a time $\tau = \tau_{ph}/2$, the qubit and mechanical resonator were maximally entangled. At interaction time τ_{ph}, the qubit was measured to be in its ground state, implying a single phonon excitation was created in the mechanical resonator. At time $2\tau_{ph}$ the excitation had been returned to the qubit, reduced in amplitude by dissipation (finite energy lifetime).

exact shape of the tuning pulse used to bring the qubit toward and away from the FBAR: The pulse is trapezoidal, due to the finite rise-time of the electronics that control the flux bias. Since the ~ 1 ns rise and fall times of this trapezoidal shape are not fast compared to qubit-resonator swap time, setting the qubit frequency somewhat above the resonator frequency favors higher state transfer probabilities. This is borne out by the simulations presented in Fig. 3.11 (c). A line cut through the experimental data is shown in Fig. 3.11 (d), for a de-tuning $\Delta = 72$ MHz, corresponding to the white dashed line in panel (b). Guided by the solutions to the Jaynes-Cummings Hamiltonian presented above, the maxima of the oscillations were fit to a swap frequency $\Omega_C/2\pi = 132$ MHz, quite close to the value obtained from qubit spectroscopy.

We next used the ability to create a single phonon excitation in the resonator to measure its energy relaxation and phase coherence times. Fig. 3.12 (a) shows the pulse sequence used to extract the resonator energy relaxation time T_{1M}. The qubit, initially in the ground state, was placed in the excited state by a π-pulse, then biased and held at $\Delta = 72$ MHz for τ_{ph}, so that the qubit excitation was fully transferred to the resonator, creating a one-phonon Fock state $|1\rangle$. The qubit, in its ground state, was then returned to its operating bias for a variable time τ. During this time the qubit and mechanical resonator were effectively decoupled, confining the phonon excitation to the mechanical resonator and allowing it to

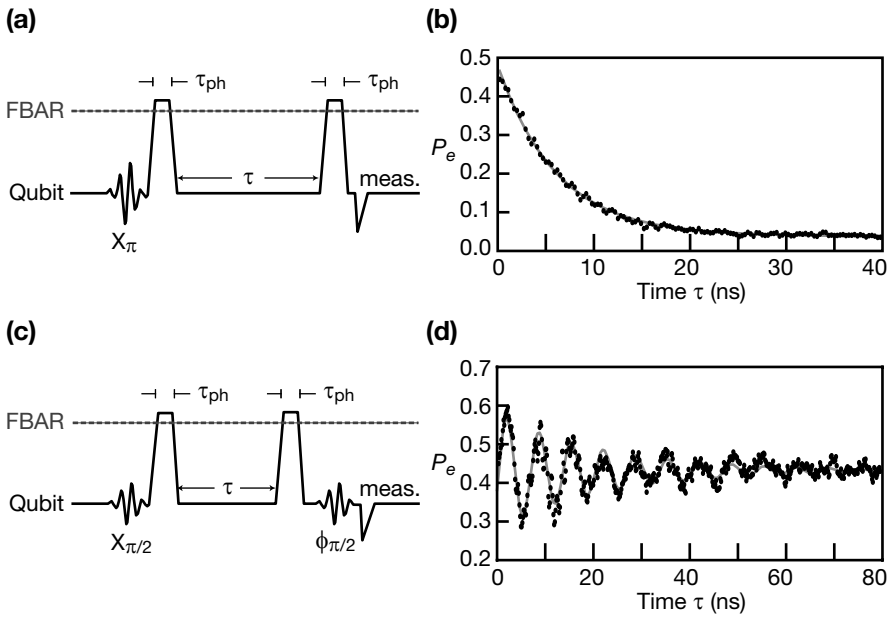

Figure 3.12: Mechanical resonator energy relaxation and phase coherence times. **a**, $T_{1\mathrm{M}}$ pulse sequence. The qubit was placed into $|e\rangle$ by a π-pulse, then tuned into resonance with the resonator for a duration sufficient to fully transfer the qubit excitation to the resonator, generating a single phonon. The qubit was then de-tuned from the resonator allowing the phonon to decay in the resonator for a time τ, after which the qubit was brought back into resonance with the resonator to transfer any remaining excitation to the qubit. **b**, Measured qubit excited state probability $P_e(\tau)$. The fit line is a direct measure of the phonon decay time, yielding $T_{1\mathrm{M}} = 6.1$ ns. **c**, Resonator phase coherence pulse sequence. This is similar to **a**, but using a $\pi/2$-pulse to prepare the qubit in the superposed state $(|g\rangle + |e\rangle)/\sqrt{2}$. The phase of the second $\pi/2$-pulse was swept in order to produce the oscillations seen in **d**, which is a measure of the resonator phase coherence. The fit line indicates $T_{2\mathrm{M}} \approx 2T_{1\mathrm{M}}$.

decay. The qubit was then brought back to $\Delta = 72$ MHz for τ_{ph}, transferring any excitation remaining in the resonator back to the qubit. Finally, the qubit was returned to its operating bias and measured. By varying the delay time τ, the measured qubit probability is a direct measure of the single-phonon energy decay in the resonator. The experimental data are shown in Fig. 3.12 (b), with a fit exponential corresponding to a mechanical energy decay time of $T_{1M} = 6.1$ ns.

The phase coherence time of the FBAR was measured in a similar fashion. The qubit was first prepared in the superposed state $(|g\rangle + |e\rangle)/\sqrt{2}$, using a $\pi/2$-pulse with controlled phase. As discussed earlier, an initial qubit state $\alpha|g\rangle + \beta|e\rangle$ can be transfered to the mechanical resonator phonon state $\alpha|0\rangle + \beta|1\rangle$ by allowing the coupled system to interact for a time $\tau = \pi/\Omega_C$; a length of time equivalent to the experimentally determined single phonon swap time τ_{ph}. Using this technique we transfered the initial superposed qubit state to the mechanical resonator, creating the superposed phonon state $(|0\rangle + |1\rangle)/\sqrt{2}$. After the state transfer was complete, the qubit, now in its ground state, was detuned from the resonator to decouple the system. The qubit was then held at its operating bias to allow the superposed phonon state to decay in the resonator. After a time τ, the qubit was brought back into resonance with the mechanical resonator and allowed to interact for τ_{ph} in order to transfer any remaining phonon superposition back to a superposition of qubit states. The qubit was then returned to the operating bias and measured.

This experiment was repeated for varying hold times τ.

However, in order to obtain an accurate measure of the decay of the resulting superposed state, the measurement was conducted using a Ramsey fringe technique [35]. Just before the qubit excited state probability was read-out, a $\pi/2$-pulse was applied to the qubit. The phase of this pulse $\phi_{\pi/2}$ was then swept at an angular frequency ω_ϕ, producing the oscillation frequency seen in the data $\omega_\phi/2\pi$. The phase coherence time was determined from a fit to the resulting oscillation, $T_{2M} \simeq 20$ ns.

The fact that the dephasing time was measured to be more than twice the energy relaxation time (the theoretical limit) was most likely a result of the complexity of the pulse sequence, where small pulse shaping errors can lead to longer-than-expected phase coherence times. Note that during this measurement of the resonator phase coherence, the mechanical resonator was placed in a superposition of its ground and first excited states, a very non-classical quantum superposition.

We performed one final experiment to observe the effect of higher energy Fock states $|n\rangle$, with $n \geq 2$, in the mechanical resonator. These higher levels were populated by directly exciting the resonator with an on-resonance Gaussian microwave pulse coupled through the on-chip external capacitor C_x. During this microwave pulse, the qubit was kept off-resonance and thus not directly excited by the microwave signal. As previously discussed, the state of the resonator after

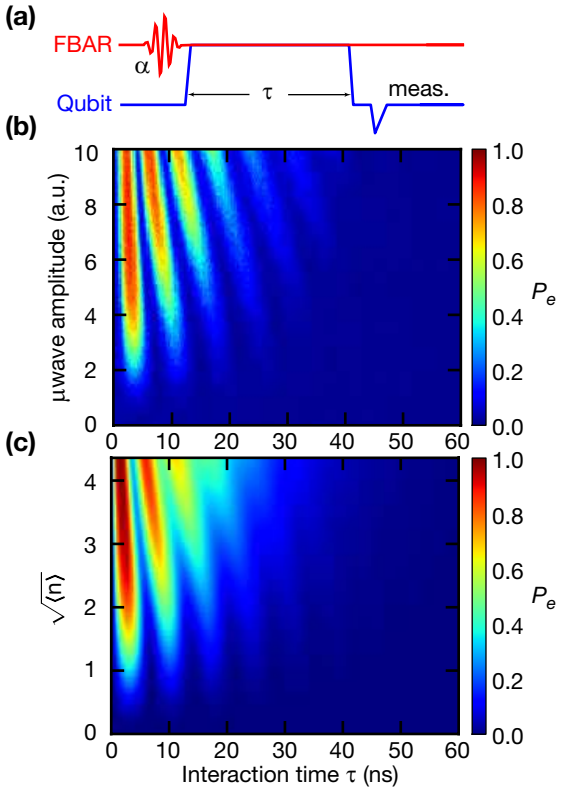

Figure 3.13: Coherent state pulse sequence, data, and simulation **a**, a classical Gaussian microwave pulse was applied directly to the FBAR. After the microwave pulse was turned off, the qubit was tuned into resonance and allowed to interact with the excited FBAR for a time τ. The qubit, initially in its ground state $|g\rangle$, was measured and the excited state probability P_e recorded. The experiment was then repeated for varying initial microwave pulse amplitudes and interaction times. **b**, experimental data showing the expected increase in swap frequency when the qubit is allowed to interact with a more highly excited FBAR. **c**, quantum simulations show similar expected shortening of swap period for the interaction between qubit and mechanical resonator. For the simulations, the FBAR was initially placed in a coherent state with average phonon number $\langle n \rangle$.

this pulse will be a coherent state [15]. The qubit, initially in its ground state $|g\rangle$, was then brought into resonance with the resonator, and allowed to interact for a variable time τ at detuning $\Delta = 0$. The qubit was then returned to its operating bias and its excited state probability measured. The amplitude of the initial microwave pulse was varied while repeating this measurement. The pulse sequence and resulting data are shown in Fig. 3.13 (a) and (b). From the data presented there, the swap frequency can be seen to increase with higher microwave pulse amplitude. Larger microwave pulse amplitudes create initial coherent states with more highly populated Fock states $|n\rangle$. Since the qubit-resonator interaction strength scales as $\sqrt{n}g_0$, these more highly excited Fock states effectively cause the qubit and resonator to be more strongly coupled [15]. Correspondingly, the time needed to transfer energy between qubit and resonator is reduced. The increase in swap frequency with increasing excitation, and thus phonon number n, is reproduced in the numerical simulations presented in Fig. 3.13 (c).

More complex experiments, such as arbitrary phonon state generation, similar to those performed with microwave electromagnetic resonators [14], were not feasible with this system, due to the quite short energy relaxation time of the mechanical resonator. Future experiments, such as those involving Wigner tomography, to further verify that the mechanical quantum states were indeed non-classical, is an obvious future direction. The primary improvement needed to perform mea-

surements in this area would be to increase the energy lifetime (i.e. the quality factor Q) of the resonator, preferably by a factor of ten or more.

In conclusion, we have created a novel system by coupling a qubit to a mechanical resonator, with which we were able to explore non-classical effects in a mechanical resonator. Spectroscopic measurements displayed the characteristic resonant mode splitting of a coupled system; an essentially classical result. We then used the qubit as a "quantum thermometer" to measure the thermal occupation of the mechanical resonator. Using this technique, the mechanical resonator was determined to be in the quantum ground state. To further reveal the quantum nature of the mechanical resonator, we used the qubit as a "quantum transducer" to prepare single phonon states, creating entangled qubit-phonon states in the process. We then measured the single phonon energy lifetime of the mechanical resonator $T_{1\mathrm{M}} = 6.1$ ns. A similar technique was employed to extract the resonator's phase coherence time $T_{2\mathrm{M}} \approx 2T_{1\mathrm{M}}$, which necessitated the creation of superposed phonon states. Finally, to explore the effects of higher phonon levels, we excited the resonator directly to create coherent phonon states. These measurements provide strong evidence that we have achieved elementary quantum control over a macroscopic mechanical system.

Chapter 4

The loose ends

The aim of this chapter is to provide additional support for some of the statements made in the previous chapter, or, in parts, to add to the discussion. Although the flow of this chapter may seem stochastic, at least the topics are ordered in the same way as they were presented in the previous chapter.

An outline of this chapter is as follows: In the first section we calculate the expected electrical response of a mechanical resonator when measured spectroscopically. We begin by constructing a lumped element circuit representation of a mechanical resonator attached to a vector network analyzer in a two-port configuration. Using elementary circuit analysis, we obtain an expression for the normalized transmitted signal recorded by the network analyzer S_{21}. It was this resulting expression which was used to fit the classical spectroscopic response,

presented in Fig. 3.2 of the last chapter. The values for the circuit parameters, quoted there, were also obtained using this fit.

The next section provides a plot of the classically obtained qubit-mechanical resonator coupling strength. To produce this plot, we assumed the equivalent circuit component values obtained from the fit of the measured spectroscopic response, shown in Fig. 3.2. This analysis serves no greater purpose than to place numeric values on the possible range of coupling strengths and to provide justification for our choice of coupling capacitor.

We then examine the full form of the qubit-resonator interaction Hamiltonian and identify the terms that were previously dropped when taking the rotating wave approximation. Although the actual experiment was conducted in a regime where the rotating wave approximation was applicable [45], the previously neglected terms may become significant if future experiments are conducted on FBARs of much larger sizes or with much higher piezoelectric coupling efficiencies.

Following that discussion, we switch gears to examine the expected off-resonant performance of the qubit, subject to the possible energy loss mechanisms. We sketch the results of a calculation that indicated an appreciable amount of dissipation may arise from the combination of dielectric losses of the AlN contained in the FBAR and the SiO_2 layer upon which the qubit rests. We then present the experimentally measured energy decay time of the qubit T_{1q}, and find it to be

significantly shorter than what was expected from the dielectric loss calculation, although still within the same order of magnitude.

Lastly, we outline the Lindblad formalism used to incorporate decoherence into the quantum simulations presented in the previous chapter. Also in this section, we present the details of the procedure used to place an upper bound on the quoted average phonon number $\langle n \rangle$ and ground state probability P_0 of the FBAR measured with the ground state pulse sequence presented in the previous chapter.

4.1 Classical FBAR spectroscopic analysis

The normalized transmission, S_{21}, resulting from a spectroscopically measured FBAR, can be modeled with the circuit presented in Fig. 4.1 (a). Fitting the measured data to this model enabled the extraction of MBVD component parameters. In this model, a transmission measurement is conducted by exciting the device under test with a voltage source V_{in} and monitoring the output voltage at V_{out}, as indicated in Fig. 4.1 (a). Since the vector network analyzer used to measure the FBARs was designed to be matched to 50 Ω, we have modeled this built-in impedance with two in-line resistors, each with value $R_x = 50\ \Omega$. The other circuit components were described in the previous chapter, where we have included the full form of the MBVD model, the stray inductance L_S, and the impedance transforming external capacitors C_x used to ensure the FBAR is not

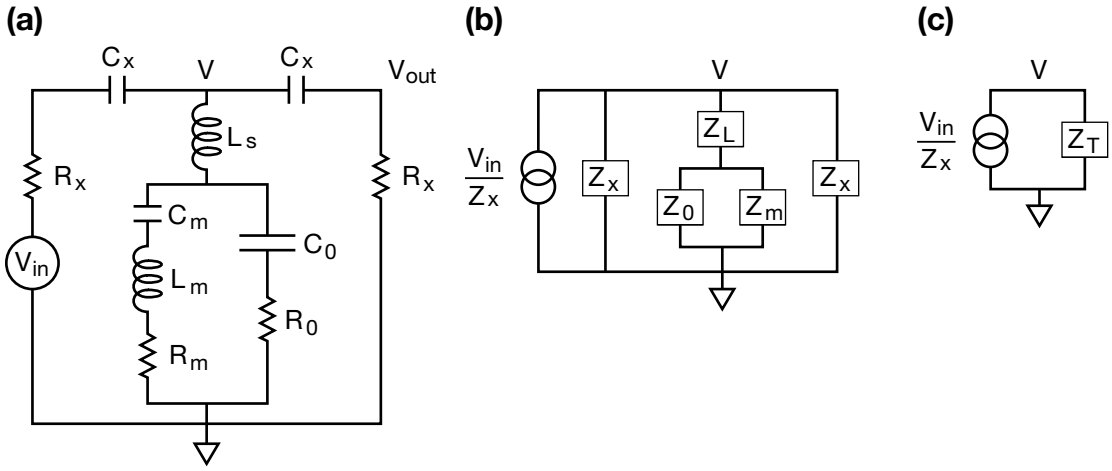

Figure 4.1: **a**, full spectroscopic measurement circuit including the built-in vector network analyzer impedance $R_x = 50\ \Omega$. The network analyzer measures a normalized voltage ratio $S_{21} = 2V_{out}/V_{in}$. **b**, Norton equivalent circuit. **c**, current biased circuit depicting the fully combined impedance of the transformed elements.

appreciably damped by R_x.

In order to express the measured signal $S_{21} = 2V_{out}/V_{in}$ in terms of circuit parameters, we transform the full circuit into the Norton equivalent circuit as depicted in Fig. 4.1 (b). The voltage source has been replaced by a current bias V_{in}/Z_x, where $Z_x = Z_{C_x} + R_x$, the series connection of the impedance of the coupling capacitor and vector network analyzer resistor. For convenience, the individual circuit elements of the mechanical resonator have been combined into three impedances: the impedance of the stray inductance Z_{L_S}, the mechanical branch impedance $Z_m = Z_{L_m} + Z_{C_m} + R_m$, and the electrical branch impedance $Z_0 = Z_{C_0} + R_0$. In Fig. 4.1 (c), we have combined these impedances into a total

impedance shunting the current bias of

$$Z_T = \left[\frac{2}{Z_x} + \frac{1}{Z_L + \left(\frac{1}{Z_0} + \frac{1}{Z_m} \right)^{-1}} \right]^{-1} \tag{4.1}$$

Using Ohm's law, we identify the voltage across the total impedance as $V = Z_T V_{in}/Z_x$. Now, to find the voltage measured by the vector network analyzer, we recognize that V_{out} and V are related through the voltage division $V_{out} = V R_x/Z_x$. Thus, plugging in for V, the output voltage becomes

$$V_{out} = \frac{R_x Z_T}{Z_x^2} V_{in} \tag{4.2}$$

Finally, since the vector network analyzer records the normalized voltage ratio $S_{21} = 2V_{out}/V_{in}$,

$$S_{21} = 2\frac{R_x Z_T}{Z_x^2}. \tag{4.3}$$

4.2 Coupling capacitance determination from classical analysis

The design of the coupled qubit-mechanical resonator sample was mostly driven by the somewhat limited performance of the mechanical resonators described in the last chapter. They exhibited quality factors of roughly 260, which corresponds to an expected energy decay lifetime of 7 ns at 6 GHz. To ensure the quantum state would remain measurable after being transferred from qubit to resonator and then back to the qubit, it was determined that a coupling strength of at least 100 MHz was needed.

If the only consideration were to create the strongest possible coupling between qubit and mechanical resonator, then a direct electrical connection should be made between the two. Since the mechanical resonator has a coupling efficiency of $k_{eff}^2 = 1.2$ %, this places a natural upper bound on the maximum qubit-resonator coupling strength. Optimal coupling can be achieved by forgoing the qubit shunting capacitor entirely and relying on the electrical capacitance of the mechanical resonator to shunt the qubit. The resulting coupling strength obtained is shown as the largest coupling strength in Fig. 4.2, approximately 400 MHz, where we have plotted the coupling strength for a qubit with fixed $C_{q,eff} \approx 1$ pF directly connected to a ~ 6 GHz mechanical resonator.

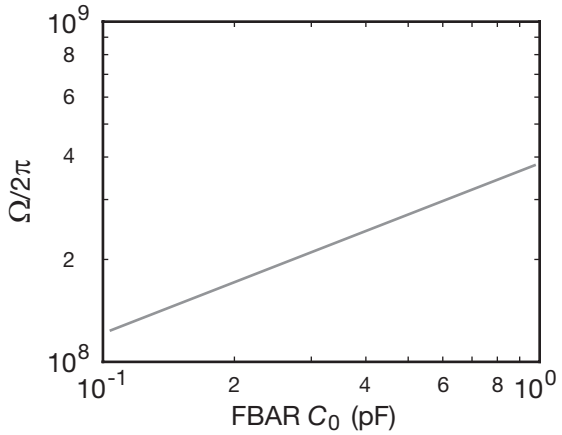

Figure 4.2: Directly connected qubit-mechanical resonator coupling strength over the practical range of resonator electrical capacitances. The maximum coupling occurs when the electrical capacitance of the mechanical resonator is used to completely shunt the qubit, $C_0 = 1.0$ pF. The corresponding radii of ~ 6 GHz disk FBARs with these electrical capacitances would range from 10-40 μm.

However, the disadvantage of direct coupling comes from the dependence on the size of the mechanical resonator, and thus for fixed FBAR film thickness, a dependence on the electrical capacitance. It may not be practical to make resonators that differ greatly from a size proven to work well. A typical electrical capacitance for many of the classical FBARs tested was $C_0 \approx 0.2$ pF. Therefore, when designing FBARs coupled to qubits, we chose to preserve this electrical capacitance. While directly coupling a $C_0 = 0.2$ pF FBAR to a qubit would have produced a tolerable coupling strength of around 175 MHz, we opted to introduce an interdigitated coupling capacitor $C_x = 0.5$ pF to limit the interaction strength to around 125 MHz. We would like to point out that since we have previously

shown that a capacitively coupled qubit-FBAR can be mapped back to a directly coupled qubit-FBAR circuit with renormalized capacitances, the choice to use a coupling capacitor was only made out of convenience. For future experiments, if one is willing to create FBARs of the appropriate size, a direct link between qubit and FBAR may be preferable due to the corresponding reduction in the complexity of the fabrication.

4.3 Coupled qubit-resonator Hamiltonian and RWA

The qubit and mechanical resonator are phase-charge coupled, also commonly referred to as X-Y coupling. Although the rotating wave approximation (RWA) should accurate describe the qubit-mechanical resonator coupling for the previously examined coupled qubit-resonator sample [45], in future experiments one may wish to increase the coupling strength to the point where the RWA is no longer applicable. To this end, and for completeness, we now examine the full form of the coupling Hamiltonian [5, 10]

$$\delta H = -ig \sum_{mm'} \chi_{mm'}(a - a^\dagger) c_m^\dagger c_{m'}, \tag{4.4}$$

where $\chi_{mm'}$ are the qubit dipole matrix elements, $a^\dagger$ and a are the resonator raising and lowering operators, and $c_m^\dagger$ and c_m are the creation and annihilation operators for the qubit states $m = 0, 1$ [45]. This full form of the coupling Hamil-

tonian can be broken into

$$\delta H = \delta H_{JC} + \delta H_V, \tag{4.5}$$

where δH_V are the terms that were previously neglected

$$\delta H_V = -ig\left[\chi_{00}c_0^\dagger c_0(a-a^\dagger) + \chi_{01}c_0^\dagger c_1 a - \chi_{01}c_1^\dagger c_0 a^\dagger + \chi_{11}c_1^\dagger c_1(a-a^\dagger)\right]. \tag{4.6}$$

We can rewrite this additional contribution to the coupling in terms of the previously introduced qubit, z, lowering, and raising operators $\sigma_z, \sigma_\pm$ as

$$\delta H_V = -ig\left\{\left[-\frac{\Delta\chi}{2}\sigma_z + \frac{1}{2}\left(\chi_{00}+\chi_{11}\right)\sigma_0\right](a-a^\dagger) + \frac{\chi_{01}}{2}\left(\sigma_+ a - \sigma_- a^\dagger\right)\right\}, \tag{4.7}$$

where $\Delta\chi = \chi_{11} - \chi_{00}$, and σ_0 is the identity. These terms all oscillate with at least a frequency of Ω_{M} in the qubit-FBAR instantaneous interaction picture [10]. A discussion of the regime in which these terms provide a significant contribution to the coupling can be found in Ref. [45].

4.4 Off resonant qubit characterization

Before finalizing the design of the coupled qubit-mechanical resonator sample, we calculated the dissipative effect of the SiO_2 substrate layer and the dielectric loss resulting from the portion of the FBAR electrical capacitance C_0 seen by the qubit. Although, we found that these loss mechanisms should limit the qubit energy decay time to $T_{1q} \approx 60$ ns for a 6 GHz resonator, this length of time would have been sufficient to perform single qubit gate operations, and is significantly longer than the estimated FBAR energy decay time of 6.6 ns.

This result was calculated by estimating the expected qubit lifetime that would result from dielectric losses alone. An upper bound on the loss was calculated by assuming a substrate entirely composed of thermal SiO_2. This reduced the overall expected qubit lifetime to approximately 84 ns, taking into consideration the qubit interdigitated shunting and coupling capacitors [30]. In addition, far off resonance, the total qubit effective capacitance, $C_{q,eff}$, contains a non-negligible portion of the FBAR electrical capacitance. For the values of the mechanical resonator and coupling capacitor used in the experiment, the additional loss coming from the AlN layer of the FBAR further reduced the qubit energy lifetime to around 60 ns [30].

Once the qubit-mechanical resonator sample had been fabricated, mounted, and cooled to base temperature, we were able to directly measure the off-resonant energy lifetime of the qubit. However, prior to measuring T_{1q}, a suitable off-resonant qubit operating frequency had to be defined. This off-resonant frequency was determined by examining the combined resonant modes mapped out by qubit spectroscopy. We chose a frequency of 5.44 GHz, approximately 735 MHz detuned from $\Omega_{\mathrm{M}}/2\pi$, and effectively decoupled from the FBAR. The extent to which the qubit and FBAR remain coupled at this operating frequency can be determined, in the context of the RWA, to be $\Omega_C^2/(\Omega_C^2 + \delta^2) = 0.03$. It was at this operating frequency where all single qubit operation were performed.

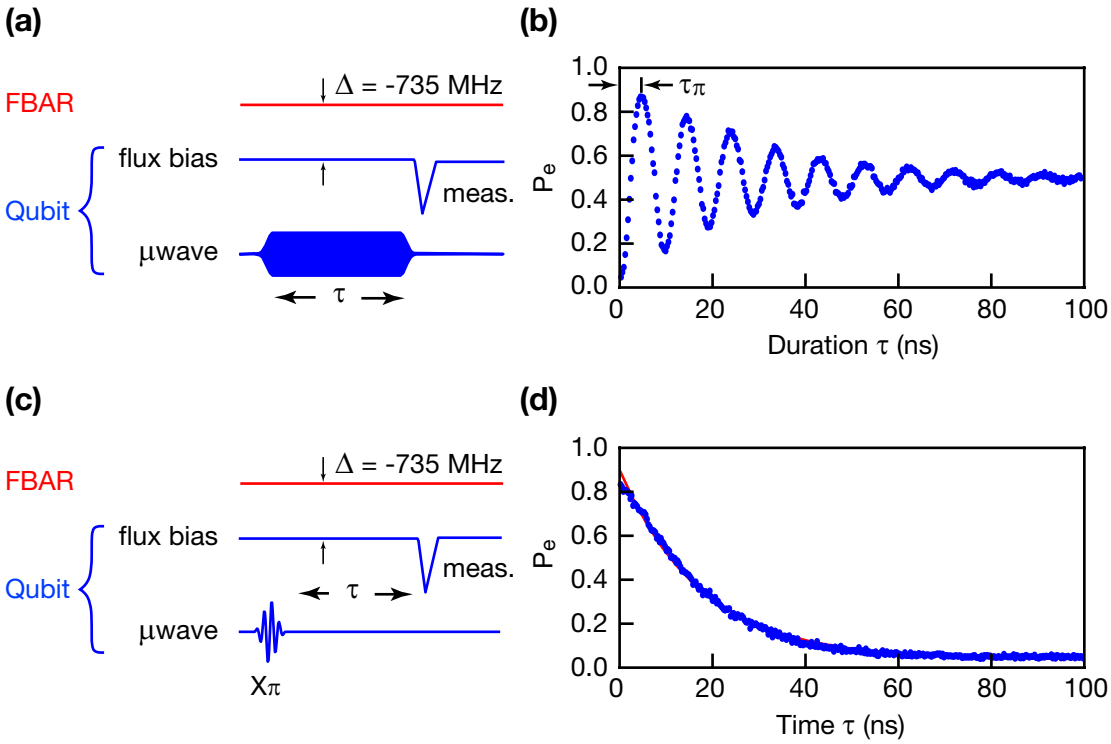

Figure 4.3: **a** with the qubit far detuned from the resonator $\Delta = -735$ MHz, a fixed amplitude microwave pulse as applied to the qubit for a variable time τ. **b** measured Rabi oscillations induced by the microwave drive. For the fixed microwave amplitude, τ_π was the pulse length need to most fully exchange $|g\rangle$ with $|e\rangle$. **c** the qubit was placed in $|e\rangle$ by a π-pulse then allowed to decay for a time τ. Any remaining P_e was then measured. **d** the measured qubit P_e (blue points) were fit to an exponential decay (red line) with a time constant of $T_{1q} \approx 17$ ns.

Before measuring T_{1q} we first determined the proper duration of a microwave drive pulse needed to excite the qubit $|g\rangle \rightarrow |e\rangle$ transition. The necessary pulse duration was found by exciting the qubit with fixed amplitude microwaves for variable lengths of time τ. The resulting qubit excited state probability was then recorded. As discussed previously, exciting the qubit with microwaves will produce $|g\rangle \leftrightarrow |e\rangle$ Rabi oscillations, where the optimal pulse duration is the length of time needed to produce the point of maximal probability transfer. For the chosen microwave drive amplitude, this time corresponded to $\tau_\pi = 5.0$ ns as illustrated in Fig. 4.3 (b). A microwave pulse of this type is known as a π-pulse, since it induces a π rotation in the Bloch sphere representation, most fully swapping the ground and excited state amplitudes.

We now used this ability to monitor the energy relaxation of the qubit. The pulse sequence, illustrated in Fig. 4.3 (c), begins with the qubit in $|g\rangle$. A π-pulse then places the qubit in $|e\rangle$, from where it relaxes toward the ground state for a duration of time τ before the excited state probability is read out. By repeating this process many times for varying durations, P_e as a function of time was mapped out. As shown in Fig. 4.3 (d), the data followed the expected form of an exponential decay with a fit decay constant $T_{1q} \approx 17$ ns. This measured time of $T_{1q} \approx 17$ ns is significantly shorter than the expected energy decay time of around 60 ns, calculated from dielectric losses alone. Although the exact cause

of this discrepancy is unknown, the shorter than expected decay time may be a result of additional mechanical dissipation from off-resonant coupling to the piezoelectrically active AlN layer of the mechanical resonator.

4.5 Lindblad formalism for quantum simulations

The material presented in this section follows, directly in parts, the discussion originally appearing in the supplementary information of "Quantum ground state and single-phonon control of a mechanical resonator" by O'Connell et al. [31].

To produce the numerical quantum simulations previously presented, we used the approximate (RWA) coupling term of the Jaynes-Cummings Hamiltonian. We have also modeled the FBAR as a harmonic oscillator, but, as needed we have extended the number of energy levels composing the qubit term, using the known level-dependent energy dispersion of the phase qubit.

For the quantum ground state simulations presented in Fig. 3.10 of the previous chapter, we included five qubit levels, and six equally-spaced FBAR energy levels. For the swap simulations (Fig. 3.11) we used two qubit levels, and five resonator levels. For the more energetic coherent state simulations (Fig. 3.13), we used eight qubit levels, and 38 equally-spaced energy levels for the resonator, which provided sufficient energy range to accommodate relatively large resonator excitations.

Decoherence was incorporated using the Lindblad master equation [22],

$$\frac{d\rho}{dt} = -\frac{i}{\hbar}[H,\rho] + \frac{1}{2}\sum_k [L_k, \rho L_k^\dagger] + [L_k\rho, L_k^\dagger], \tag{4.8}$$

where standard Lindblad operators were used to include qubit energy decay, $L_{1q} = \sqrt{1/T_{1q}}\,a$, qubit pure dephasing $L_{\phi q} = \sqrt{2/T_{\phi q}}\,a^\dagger a$, resonator energy relaxation $L_{1\mathrm{M}} = \sqrt{1/T_{1\mathrm{M}}}\,a$ and resonator pure dephasing $L_{\phi\mathrm{M}} = \sqrt{2/T_{\phi\mathrm{M}}}\,a^\dagger a$. For all simulations, we used the parameters $T_{1q} = 17$ ns and $T_{1\mathrm{M}} = 6.1$ ns, as measured for both the qubit and resonator. The phase coherence times $T_{\phi r,q}$ were set to an arbitrary value of 100 ns, sufficiently large that the qubit and resonator T_2 coherence times, which satisfy $1/T_2 = 1/2T_1 + 1/T_\phi$, would exhibit $T_2 \approx 2T_1$ as measured. For thermal simulations, we included the thermal excitation operator $L_\uparrow = \sqrt{\Gamma_\uparrow}\,a^\dagger$, where we set the thermal excitation and energy decay Lindblad coefficients to correspond to the Boltzmann factor, $\Gamma_\uparrow T_{1\mathrm{M}} = e^{-hf_r/k_BT}$, with T the resonator temperature and $T_{1\mathrm{M}}$ the resonator energy relaxation time [34].

For the thermal simulations presented in Fig. 3.10, the resonator was initially placed in a thermal state with temperature corresponding to a certain average number of phonons $\langle n\rangle$, the qubit placed in its ground state $|g\rangle$, and the Lindblad equation numerically integrated, for a given qubit-resonator detuning Δ, with a time step of 0.05 ns. We observed that the coupled system reached a steady state after roughly 150 ns, so the simulation was stopped at that time. The equilibrium qubit P_e was calculated for each simulation, as a function of the qubit-resonator

detuning Δ and resonator thermal phonon occupation $\langle n \rangle$; the thermal occupation was nearly the same at the start of the simulation and once the qubit and resonator had achieved equilibrium.

The upper bound we quote for the maximum average phonon number, $\langle n \rangle_{\max} < 0.07$, was obtained using a very conservative formulation: This phonon number yields a change in the qubit excited state probability P_e, between the calculated on-resonance maximum and off-resonance minimum values, corrected by the qubit visibility γ (the difference between the value of P_e measured for the qubit excited state, as prepared using a tuned qubit π-pulse, and that measured for the qubit ground state), equal to three times the standard deviation σ in the measured qubit P_e over the full range of detunings: $\langle n_{\max} \rangle \ni \gamma(P_{e,\max} - P_{e,\min}) \approx 3\sigma$.

For the swap simulations presented in Fig. 3.11, the qubit was placed in its excited state $|e\rangle$ while at the operating bias, and was then tuned to an interaction detuning Δ by applying a trapezoidal tuning pulse with a 1 ns rise time, a flat top at Δ detuning for a variable time, and a 1 ns fall time back to the resting frequency; the simulation used a 0.1 ns time step. The qubit state was evaluated immediately after returning it to the operating bias. The time axis in Fig. 3 of the main text includes both the rise and fall times (i.e. $\tau = 0$ starts at the beginning of the tuning pulse).

The trapezoidal pulse was chosen as a reasonable approximation to the flux

bias tuning pulse seen by the qubit, which includes an electronics-limited, ~ 1 ns rise and fall time. The exact shape of the frequency tuning pulse strongly effects the precise amplitude of the state transfer between qubit and mechanical resonator. For example, simulations show that when the rise and fall time is set to zero, no asymmetry in the response is observed. Using the trapezoidal tuning pulse as described, however, the pronounced asymmetry emerges, as in Fig. 3.11. However, this pulse shape is only an approximation of the actual tuning pulse, so that some discrepancies remain between experiment and simulation.

In the coherent state simulation in Fig. 3.13, the resonator was initially placed in a coherent state using a given microwave drive amplitude, quoted in terms of $\sqrt{\langle n \rangle}$, where $\langle n \rangle$ is the average phonon number of the resulting Poisson distribution. We numerically integrated the free evolution of the Lindblad equation with the qubit at the interaction frequency for a total time of 60 ns with 0.1 ns time steps. For a given value of $\sqrt{\langle n \rangle}$, the squared amplitude of the excited state of the qubit, equal to P_e, was recorded for each time step. The time dependence of P_e for a range of values of $\langle n \rangle$ was calculated.

Chapter 5

Conclusion

Taking a cue from superconducting qubits, we designed our experiment to rely only on commercial refrigeration to cool the mechanical resonator to the quantum ground state. Using the Bose distribution to predict the expected phonon number at the base temperature of our dilution refrigerator, we were guided toward high frequency mechanical resonators. In order to obtain suitably high resonant frequencies, we fabricated film bulk acoustic resonators with fundamental dilatational mode frequencies in the GHz regime.

We tackled the issue of quantum state creation and measurement by coupling a mechanical oscillator to a superconducting phase qubit. The coupled sample was cooled in a dilution refrigerator and the qubit-mechanical resonator coupling strength was verified using qubit spectroscopy, where the combined res-

onant modes of the system displayed the expected level avoidance of a coupled system. We then used the qubit at a "quantum thermometer" to measure the thermal phonon occupation of the mechanical resonant mode. By comparing the measured data to quantum simulation, it was determined with high probability that the mechanical resonator was indeed in the quantum ground state. From there, the qubit was used as a "quantum transducer" to first convert a classical microwave excitation to a well defined single qubit state and then transfer that state to the mechanical resonator. This technique was used to swap a single quanta back and forth between qubit and mechanical resonator, creating, at times, single phonon states and entangled qubit-resonator states. This ability to create single phonon states was then utilized to measure the energy decay time of the mechanical resonator, which was found to be $T_{1\mathrm{M}} = 6.1$ ns. We then conducted a Ramsey fringe experiment on the mechanical resonator to extract its phase coherence time $T_{2\mathrm{M}} \approx 2T_{1\mathrm{M}}$. We would like point out that the phase coherence measurement required the creation of the highly non-classical phonon state $(|0\rangle + |1\rangle)/\sqrt{2}$. Finally, we created a coherent state in the mechanical resonator in order to observe its higher phonon levels, thus highlighting its bosonic nature.

Future experiments on similar resonators would benefit greatly from increased mechanical energy lifetimes. If the quality factor, and correspondingly the energy lifetime, of the mechanical resonators could be considerably increased (by a factor

of 10), then the door would be opened to those experiments currently only achievable with superconducting electrical resonators. Wigner tomography, to further indicate the creation of mechanical quantum states, would be a significant step forward. By coupling an additional mechanical resonator to the qubit, macroscopically entangled superposed mechanical quantum states could be created between the two resonators. It would also be interesting to use the mechanical resonator as a quantum bus between two qubits or as a bridge between a qubit and another mechanical resonator.

Bibliography

[1] A. O. Caldeira and A. Legget. Influence of dissipation on quantum tunneling in macroscopic systems. *Phys. Rev. Lett.*, 46:211, 1981.

[2] I. Chiorescu, P. Bertet, K. Semba, Y. Nakamura, C. J. P. M. Harmans, and J. E. Mooij. Coherent dynamics of a flux qubit coupled to a harmonic oscillator. *Nature*, 431:159–162, 2004.

[3] I. Chiorescu, Y. Nakamura, C. J. P. M. Harmans, and J. E. Mooij. Coherent quantum dynamics of a superconducting flux qubit. *Science*, 299:1869–1871, 2003.

[4] J. Clarke, A. N. Cleland, M. H. Devoret, D. Esteve, and J. M. Martinis. Quantum mechanics of a macroscopic variable: the phase difference of a Josephson junction. *Science*, 239:992–997, 1988.

[5] A. N. Cleland and M. R. Geller. Superconducting qubit storage and entanglement with nanomechanical resonators. *Phys. Rev. Lett.*, 93:070501, 2004.

[6] K. B. Cooper, M. Steffen, R. McDermott, R. W. Simmonds, S. Oh, D. A. Hite, D. P. Pappas, and J. M. Martinis. Observation of quantum oscillations between a josephson phase qubit and a microscopic resonator using fast readout. *Phys. Rev. Lett.*, 93:180401, 2004.

[7] H. G. Dehmelt. Entropy reduction by motional sideband excitation. *Nature*, 262:777, 1976.

[8] M. H. Devoret, J. M. Martinis, and J. Clarke. Measurements of macroscopic quantum tunneling out of the zero-voltage state of a current-biased josephson junction. *Phys. Rev. Lett.*, 55:1908, 1985.

[9] M.-A. Dubois and P. Muralt. Properties of aluminum nitride thin films for piezoelectric transducers and microwave filter applications. *Appl. Phys. Lett.*, 74:20, 1999.

[10] M. R. Geller and A. N. Cleland. Superconducting qubits coupled to nanoelectromechanical resonators: An architecture for solid-state quantum-information processing. *Phys. Rev. A*, 71:032311, 2005.

[11] H. Goldstein, C. Poole, and J. Safko. *Classical Mechanics*. Addison Wesley, 2002.

[12] S. Gröblacher, K. Hammerer, M. R. Vanner, and M. Aspelmeyer. Observation of strong coupling between a micromechanical resonator and an optical cavity field. *Nature*, 460:724–727, 2009.

[13] S. Gröblacher, J. B. Hertzberg, M. R. Vanner, G. D. Cole, S. Gigan, K. C. Schwab, and M. Aspelmeyer. Demonstration of an ultracold micro-optomechanical oscillator in a cryogenic cavity. *Nature Phys.*, 5:485–488, 2009.

[14] M. Hofheinz, H. Wang, M. Ansmann, R. C. Bialczak, E. Lucero, M. Neeley, A. D. O'Connell, D. Sank, J. Wenner, J. M. Martinis, and A. N. Cleland. Synthesizing arbitrary quantum states in a superconducting resonator. *Nature*, 459(7246):546–549, May 2009.

[15] M. Hofheinz, E. M. Weig, M. Ansmann, R. C. Bialczak, E. Lucero, M. Neeley, A. D. O'Connell, H. Wang, J. M. Martinis, and A. N. Cleland. Generation of Fock states in a superconducting quantum circuit. *Nature*, 454:310–314, 2008.

[16] B. D. Josephson. Possible new effects in superconducting tunnelling. *Phys. Lett.*, 1:251, 1962.

[17] D. Kleckner and D. Bouwmeester. Sub-kelvin optical cooling of a micromechanical resonator. *Nature*, 444:75–78, 2006.

[18] J. D. I. Larson, P. D. Bradley, S. Warternberg, and R. C. Ruby. in Proc. 2000 IEEE Ultrasonics Symp. (eds Schneider, S. C., Levy, M. & McAvoy, B. R.). pages 863–868, IEEE, 2000.

[19] A. J. Leggett. Testing the limits of quantum mechanics: motivation, state of play, prospects. *J. Phys.: Condens. Matter*, 14:R415–R451, 2002.

[20] A. J. Leggett, S. Chakravarty, A. T. Dorsey, M. P. A. Fisher, A. Garg, and W. Zwerger. Dynamics of the dissipative two-state system. *Rev. Mod. Phys.*, 59:1–85, 1987.

[21] K. W. Lehnert, K. Bladh, L. F. Spietz, D. Gunnarsson, D. I. Schuster, P. Delsing, and R. J. Schoelkopf. Measurement of the excited-state lifetime of a microelectronic circuit. *Phys. Rev. Lett.*, 90:027002, 2003.

[22] G. Lindblad. On the generators of quantum dynamical semigroups. *Commun. Math. Phys.*, 48:119–130, 1976.

[23] E. Lucero, M. Hofheinz, M. Ansmann, R. C. Bialczak, N. Katz, M. Neeley, A. D. O'Connell, H. Wang, A. N. Cleland, and J. M. Martinis. High-Fidelity Gates in a Single Josephson Qubit. *Physical Review Letters*, 100(24):247001, 2008.

[24] J. M. Martinis. Superconducting phase qubits. *Quantum Inf. Process.*, 8:81–103, 2009.

[25] J. M. Martinis, S. Nam, J. Aumentado, and C. Urbina. Rabi oscillations in a large josephson-junction qubit. *Phys. Rev. Lett.*, 89:117901, 2002.

[26] E. Merzbacher. *Quantum Mechanics*. John Wiley & Sons, Inc., 1998.

[27] J. E. Mooij, T. P. Orlando, L. Levitov, L. Tian, C. H. van der Wal, and S. Lloyd. Josephson persistent-current qubit. *Science*, 285:1036–1039, 1999.

[28] K. Nam, Y. Park, B. Ha, D. Shim, I. Song, J. Pak, and G. Park. Piezoelectric properties of aluminum nitride for thin film bulk acoustic wave resonator. *J. Korean Phys. Soc.*, 47:S309–S312, 2005.

[29] W. Neuhauser, M. Hohenstatt, P. Toschek, and H. Dehmelt. Optical-sideband cooling of visible atom cloud confined in parabolic well. *Phys. Rev. Lett.*, 41:233–236, 1978.

[30] A. D. O'Connell, M. Ansmann, R. C. Bialczak, M. Hofheinz, N. Katz, E. Lucero, C. McKenney, M. Neeley, H. Wang, E. M. Weig, and J. M. Cleland, A. N.and Martinis. Microwave dielectric loss at single photon energies and millikelvin temperatures. *Appl. Phys. Lett.*, 92:112903, 2008.

[31] A. D. O'Connell, M. Hofheinz, M. Ansmann, R. C. Bialczak, M. Lenander, E. Lucero, M. Neeley, D. Sank, H. Wang, M. Weides, J. Wenner, J. M. Martinis, and A. N. Cleland. Quantum ground state and single-phonon control of a mechanical resonator. *Nature*, 464:697–703, April 2010.

[32] Y. A. Pashkin, T. Yamamoto, O. Astafiev, Y. Nakamura, D. V. Averin, and J. S. Tsai. Quantum oscillations in two coupled charge qubits. *Nature*, 421:823–826, 2003.

[33] D. M. Pozar. *Microwave Engineering*. John Wiley & Sons, Inc., New York, 2005.

[34] A. K. Rajagopal. The principle of detailed balance and the lindblad dissipative quantum dynamics. *Phys. Lett. A*, 246:237–241, 1998.

[35] N. F. Ramsey. A molecular beam resonance method with separated oscillating fields. *Phys. Rev.*, 78:695–699, 1950.

[36] C. A. Regal, J. D. Teufel, and K. W. Lehnert. Measuring nanomechanical motion with a microwave cavity interferometer. *Nature Phys.*, 4:555–560, 2008.

[37] T. Rocheleau, T. Ndukum, C. Macklin, J. B. Hertzberg, A. A. Clerk, and K. C. Schwab. Preparation and detection of a mechanical resonator near the ground state of motion. *Nature*, 463:72–75, 2010.

[38] J. F. Rosenbaum. *Bulk Acoustic Wave Theory and Devices*. Artech House, 1988.

[39] R. C. Ruby, P. Bradley, Y. Oshmyansky, A. Chien, and J. D. I. Larson. in Proc. 2001 IEEE Ultrasonics Symp. (eds Yuhas, D. E. & Schneider, S. C.). pages 813–821, IEEE, 2001.

[40] J. J. Sakurai. *Modern Quantum Mechanics*. Addison Wesley, 1994.

[41] A. Schliesser, O. Arcizet, R. Riviere, G. Anetsberger, and T. J. Kippenberg. Resolved-sideband cooling and position measurement of a micromechanical oscillator close to the Heisenberg uncertainty limit. *Nature Phys.*, 5:509–514, 2009.

[42] A. Schliesser, R. Riviere, G. Anetsberger, O. Arcizet, and T. J. Kippenberg. Resolved-sideband cooling of a micromechanical oscillator. *Nature Phys*, 4:415–419, 2008.

[43] E. Schrödinger. The present situation in quantum mechanics. *Naturwissenschaften*, 23:807–812; 823–828; 844–849, 1935.

[44] R. W. Simmonds, K. M. Lang, D. A. Hite, S. Nam, D. P. Pappas, and J. M. Martinis. Decoherence in josephson phase qubits from junction resonators. *Phys. Rev. Lett.*, 93:077003, 2004.

[45] A. Sornborger, A. N. Cleland, and M. R. Geller. Superconducting phase qubit coupled to a nanomechanical resonator: Beyond the rotating-wave approximation. *Phys. Rev. A*, 70:052315, 2004.

[46] M. Steffen, J. M. Martinis, and I. L. Chuang. Accurate control of josephson phase qubits. *Phys. Rev. B.*, 68:224518, 2003.

[47] J. D. Teufel, J. W. Harlow, C. A. Regal, and K. W. Lehnert. Dynamical backaction of microwave fields on a nanomechanical oscillator. *Phys. Rev. Lett.*, 101:197203, 2008.

[48] M. Tinkham. *Introduction to Superconductivity.* McGraw-Hill, 1996.

[49] C. H. van der Wal, A. C. J. ter Haar, F. K. Wilhelm, R. N. Schouten, C. J. P. M. Harmans, T. P. Orlando, S. Lloyd, and J. E. Mooij. Quantum superposition of macroscopic persistent-current states. *Science*, 290:773–777, 2000.

[50] A. Wallraff, D. I. Schuster, A. Blais, L. Frunzio, R.-S. Huang, J. Majer, S. Kumar, S. M. Girvin, and R. J. Schoelkopf. Strong coupling of a single photon to a superconducting qubit using circuit quantum electrodynamics. *Nature*, 431:162–167, 2004.

[51] G. Wendin and V. S. Shumeiko. Superconducting quantum circuits, qubits and computing. *arXiv:cond-mat/0508729v1*, 2005.

[52] D. Wineland and H. Dehmelt. Proposed $10^{14}\Delta\nu < \nu$ laser fluorescence spectroscopy on T1+ mono-ion oscillator III. *Bull. Am. Phys. Soc.*, 20:637, 1975.

[53] T. Yamamoto, Y. A. Pashkin, O. Astafiev, Y. Nakamura, and J. S. Tsai. Demonstration of conditional gate operation using superconducting charge qubits. *Nature*, 425:941, 2003.

[54] W. H. Zurek. Decoherence, einselection, and the quantum origins of the classical. *Reviews of Modern Physics*, 75:715–765, 2003.

Appendix A

Device fabrication

In the field of quantum computation, it is usually known what device specifications are needed for a successful demonstration of some new effect. Although it may be easy to describe how a device should perform, or even to envision a scheme for making such a device, it is far from trivial to actually create it. Fortunately, the nanofabrication facility at the University of California, Santa Barbara is equipped with many tools that enable the creation of micron and sub-micron featured electronic devices. Using those tools to execute a well thought out fabrication process, along with a bit of luck, can occasionally result in a device that meets performance requirements.

A.1 Mechanical resonators

It was necessary to develop a reliable process for creating mechanical resonators in order to facilitate their later incorporation into the qubit fabrication. A good deal of effort resulted in a process that is reliable and easily reproduced as long as one is familiar with the reasoning behind each of the steps.

A.1.1 L-Edit design

The fabrication process begins by carefully designing each photo-lithographic layer. In the our group this is facilitated through the use of L-Edit, a computer assisted design program by Tanner EDA. Once the design is complete these patterns are transfered to photo-lithograph reticles (masks) for use in an I-line UV stepper. Since we are conducting fundamental research instead of making small changes to a known working circuit, the design of a successful mask can be quite challenging. One of the major considerations is the interaction between subsequent layers and those previously processed. One must not only ensure that the patterns make physical sense but also pay close attention to the effects of subsequent etches on all layers, especially if those etches accidentally of intentionally etch significantly past their target layer.

Another important aspect of a successful design is the incorporation of adequate tolerance. Using the machines found in the UCSB nanofabrication facility,

a good rule of thumb is to design traces with a minimum width of 1.5 microns and to allow five microns of interlayer alignment offset error. If it is absolutely necessary trace widths just smaller than one micron can be used with a good bit of effort tuning up the exposure and developing times. Also, it is possible to achieve sub-micron alignment between layers but this requires test exposures and careful attention to any irregularities in prior layers that caused their lateral dimensions to vary from their design values.

The last major issue that plagues the designer of a new process is the fact that one will almost certainly encounter problems with their design that become apparent only after the fabrication process has begun. Many of these issues are difficult if not impossible to predict beforehand. One technique to help ease this concern is to create multiple designs with slight variations. The hope is that by taking educated guesses at potential problems at least one combination of design parameters will lead to a design robust enough to withstand these unforeseen issues. Another benefit of creating many designs is that if more than one design produces working devices, then the performance differences of those devices can be compared for optimization purposes. With this in mind, we have created an exposure technique that selectively exposes only parts of the entire design at a given time. By puzzle-piecing these parts together, we produce the desired pattern.

The way this is accomplished in practice is to first separate out the novel parts of the circuit from the generic. The novel part of the circuit, in this case, is the mechanical resonator structure, its lead wire, and its connection to ground. The rest of circuit elements: bond pads, ground plane, waveguides, and coupling capacitors, make up the generic part of the circuit and exists only to facilitate connection to the measurement lines. For each lithographic layer we created 36 novel element designs and one generic design, for a total of 37 patterns. We then create two separate reticle layers, one for the 36 active element designs and one for the generic design. Typically, these two reticle layers are then written to separate masks. When it comes time to transfer this pattern to the photoresist, it takes two exposures to create a complete pattern on the wafer. One of the exposures uses the novel element mask and selectively exposes only one of the 36 patterns (to be discussed below). The second exposure uses the generic mask and exposes the rest of the pattern.

This technique was created to maximize the number of possible patterns without requiring the creation of many more mask plates. Using this double exposure method requires at most twice the number of masks for 36 times as many patterns. We applied this idea of modular design once more by also separating out the coupling capacitors, creating four coupling capacitance variations. However, instead of designing a new mask composed only of coupling capacitors, we were

able to fit the relatively small patterns in the middle of the generic circuit mask. Thus, with only twice the number of masks, 144 distinct patterns were available during the fabrication process

There was one final technique used to cut down on the number of masks needed. Since masks are relatively expensive and our die size is sufficiently small, we do not need to transfer just one lithographic layer design to an entire mask. Instead, by placing one lithographic layer in each corner, we were able to fit four different lithographic layers onto a single mask. When exposed, only one quadrant of the mask remains uncovered by shutters so that only the desired pattern is allowed to illuminate the wafer.

With these technical details now covered, we illustrate the complete mask set used to fabricate test mechanical resonators. A complete mechanical resonator consists of four lithographic steps: base wiring, AlN vias, top wiring, and mechanical resonator (MR) define.

Base wiring

The design of the mechanical resonator base wiring layer is composed of one generic wiring pattern, the novel resonator geometry, and the coupling capacitors. The generic wiring pattern is shown in Fig. A.1 and consists of launchers leading into a square space left for a coupling capacitor, and finally connecting to the

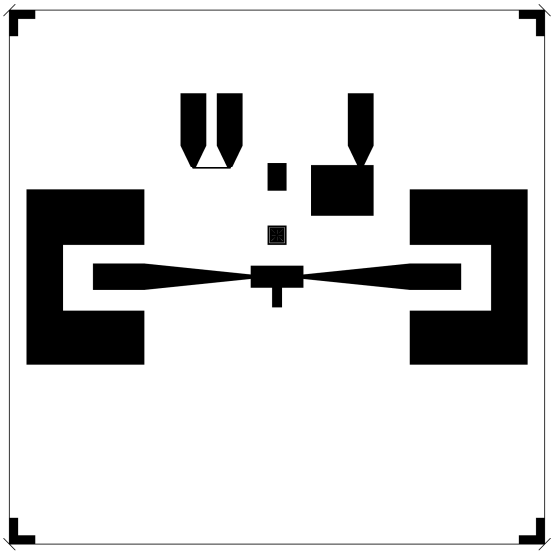

Figure A.1: Generic mechanical resonator base wiring. The black areas represent unexposed photoresist. Bond pads connecting to tapering waveguide leads to the center of the chip where the novel part of the circuit has yet to be defined. The alignment mark is the located above the center of the chip and can be identified as the square shaped pattern containing a star. The other structures above the alignment mark are used for testing purposes.

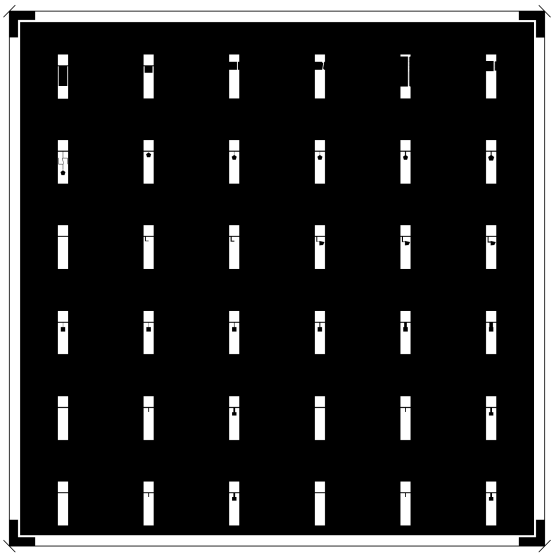

Figure A.2: Novel mechanical resonator base wiring. All 36 possible choices for the mechanical resonator.

center of the die where the dangling rectangular region exists as a space in which to place the novel mechanical resonator pattern. The three other structures of interest lie across the top of the die. From left to right they are a short test, to ensure the launchers are actually sending signal to the resonator, a Dektak strip to measure the height of each deposited layer, and the bottom electrode of a capacitor, that once finished, will be large enough to be easily measured with an LCR meter.

Along with the generic wiring pattern, the coupling capacitors and novel mechanical pattern are needed to complete the layer. The coupling capacitors were designed with the standard interdigitated geometry, customarily used in the qubit group. They are located in the center of the generic mask. The novel mechanical

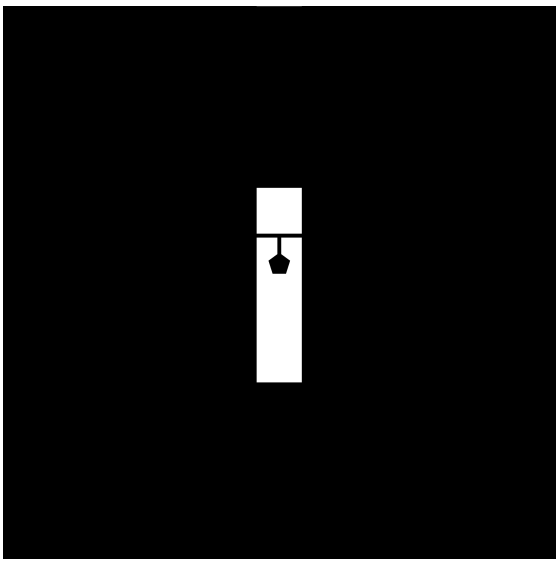

Figure A.3: Expanded view of novel mechanical resonator base wiring. One of the possible choices for the mechanical resonator. The leg connects the lead wiring to the pentagonal section, which will serve as the bottom electrode of the mechanically active part of the resonator.

mask is shown in Fig. A.2. Only one of these patterns is needed to complete the layer. At the time of expose all but one are blocked with the automated mechanical shutters of the GCA Autostep200. The number and spacing of the patterns was limited by the smallest shutter aperture size the stepper would allow. A detailed view of a particular mechanical resonator is shown in Fig. A.3 and features the lead transmission line running across the top, and the bottom electrode of the mechanical resonator, which can be identified as the pentagonal shape. We have dubbed the lead connecting to the resonator, the "leg", because there will be two of them connected to the FBAR structure once the fabrication is complete.

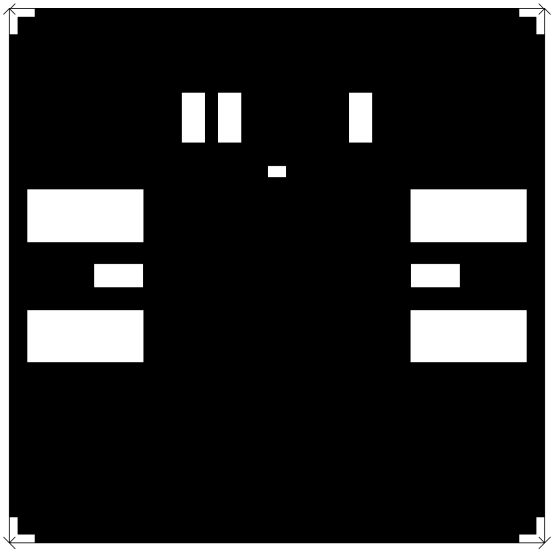

Figure A.4: Generic mechanical resonator vias. White area shows where holes will be etched through the AlN layer.

Vias

When this pattern is exposed, the base wiring has already been blanket coated with a layer of AlN. It is necessary to create holes through the AlN, while stopping on the aluminum base layer, to allow electrical connection to the underlying aluminum. Since all of the mechanical resonators are connected to the generic wiring in the same way, there is no need for resonator specific vias and there is only one generic pattern for this step (see Fig. A.4).

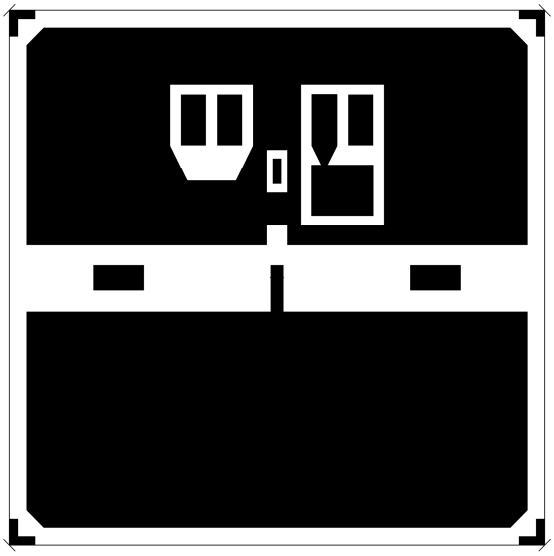

Figure A.5: Generic mechanical resonator top wiring. Black features represent the resulting aluminum pattern. The largest feature shown is the ground plane. The rectangles shown on each side are extra aluminum to thicken the bond pads to aid in the wire bonding process.

Top wiring

This layer has both a generic and a novel component. In Fig. A.5 the generic part of the circuit is shown. The large dark areas from the ground plane and are connected to each other through the base wiring layer. The ground plane extends upward in the middle of the chip in a rectangular region left in order to subsequently expose the novel pattern. Once again we have a pattern with 36 possible choices for the top electrode of the mechanical resonator, and we need to shutter off all but one. However, this time, the pattern must correspond to the previously chosen base wiring. We show such a pattern in Fig. A.6, where

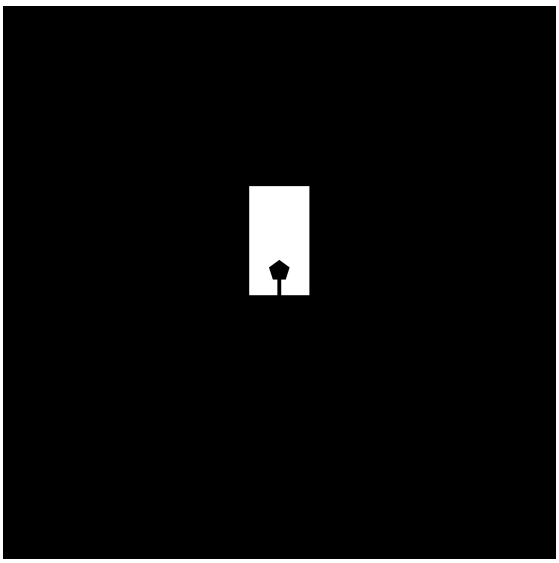

Figure A.6: Expanded view of novel mechanical resonator top wiring. View of just one of the possible choices showing the top electrode aluminum layer of the mechanical resonator. The leg leading away from the pentagon is connected to ground.

the pentagonal shape is the top electrode of the mechanical resonator and the leg leads to the ground plane. The top wiring pattern is radially five microns smaller than the base wiring layer so that the pentagonal pattern fits within the area defined by the bottom electrode. Although there should not be any holes in the AlN, this was done to minimize the chance of having shorts between the electrode layers at the step edge.

Mechanical resonator define

The last lithographic pattern is used to define the shape of the mechanical resonator by transferring its pattern though all the layers and slightly into the silicon

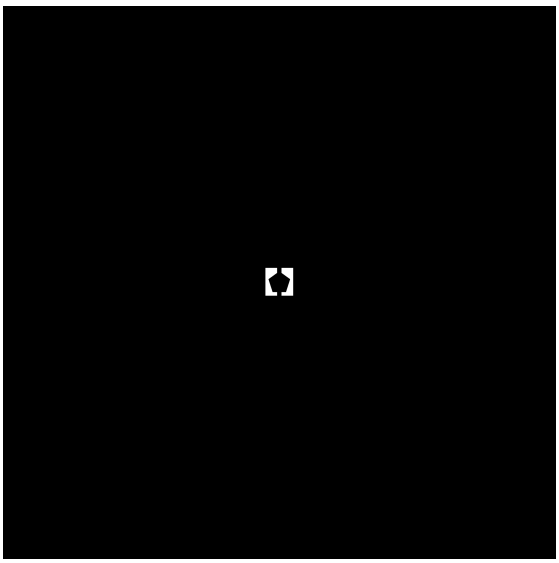

Figure A.7: Expanded view of novel mechanical resonator defining pattern. This defines the final shape of the mechanical resonator structure since the protected area (black) is slightly smaller than previous layer. Plasma etching will form vertical sidewalls that cut though all layers including the oxide on the substrate.

substrate. Since only the shape of the mechanical resonator results from this step, there is no need for a generic pattern. The shape of the mechanically active part is once again five microns smaller than the previous layers so that it produces vertical sidewalls in this pattern, free from edge effects of previous layers, except for the one place where the top wiring steps up onto the base wiring.

A.1.2 Stepper program

These patterns are transfered to a photoresist coating on wafer by using the GCA AutoStep 200 I-Line Wafer Stepper located in the UCSB nanofabrication facility.

In order to understand how these patterns are transfered to the photoresit, we describe some of the specifics of stepper operation.

Shutter limits

The automatic capabilities of the stepper are what enables the previously described flexibility in pattern choice. The stepper is equipped with shutters that are capable of blocking off most of the mask area. There are four shutters called X-Left, X-Right, Y-Front, Y-Rear. Each shutter can range from fully open with a value of zero, to fully closed with a value of 100. However, since the shutters are physical objects, they can collide if improper values for their position are entered, e.g. X-Left = 52, X-Right = 52. In addition to the obvious limits on shutter positioning with respect to each other, it has been experimentally determined that there must be at least 5.5 percentage clearance left between opposing shutter, e.g. X-Left = 31, X-Right = 63.5. Thus, the shutters have a minimum exposure size that corresponds to an on-chip size of approximately 1 mm by 1 mm (when programming the stepper all units are expressed as their 5x reduced exposed values so that is what we will use for the remainder of this section). Taking this into consideration when designing the novel mask plates, unique patterns were spaced 1 mm apart in both the x and y directions, beginning at -2.5 mm in both x and y.

Pass shifts

The final consideration, to determine shutter positioning, is the fact that we only use the top left corner of the mask plate for any given layer, as discussed above. The pass shift offset we typically use to define the center of this pattern is (−4.0 mm,−4.0 mm). The directional sign is a little strange here as the negative x direction moves the wafer in the negative x direction with respect to the mask, while the negative y direction moves the wafer in the positive y direction with respect to the wafer. One could interpret this as lying underneath the mask with one's head closest to the door of the stepper and looking upwardly at the mask, however I do not find this mental exercise particularly helpful so we will just take the negative y direction as up.

To correctly position a particular novel pattern this pass shift must be taken into consideration so that the effective positions of the patterns range from -6.5 mm to -1.5 mm in both the x and y directions.

Shutter positions

The necessary values of the shutters to expose an individual novel pattern were determined experimentally. The edge of the pattern occurs at a value of 16 for both the X-Left and Y-Rear shutter. By only allowing for the minimum exposed area the other two shutter positions can be determined to be 78.5 for X-Right and

row	pass shift x (mm)	shutters (XL, XR)
1	-6.5	(16, 78.5)
2	-5.5	(21, 73.5)
3	-4.5	(26, 68.5)
4	-3.5	(31, 63.5)
5	-2.5	(36, 58.5)
6	-1.5	(41, 53.5)

Table A.1: Pass shift and shutter positions for novel pattern row.

column	pass shift x (mm)	shutters (YF, YR)
1	-6.5	(78.5, 16)
2	-5.5	(73.5, 21)
3	-4.5	(68.5, 26)
4	-3.5	(63.5, 31)
5	-2.5	(58.5, 36)
6	-1.5	(53.5, 41)

Table A.2: Pass shift and shutter positions for novel pattern column.

Y-Front. Since the mask plate has roughly 100 mm of usable lateral dimensions, to move the shutters 1.0 mm chip distance corresponds roughly to a 5 mm shutter adjustment, which is 5 percent. Thus, the other shutter positions for the possible novel pattern choices are calculable as ranging from 16 to 41 in both X-Left and Y-Rear, and 78.5 to 53.5 in X-Right and Y-Front, in increments of 5.

Lookup table

It is taxing to calculate the proper shutter positions and pass shift for every novel pattern, so here we present a lookup table for convenience. Using standard row column notation to denote a specific novel pattern position in the L-Edit file, we

can easily find the desired shutter positions and pass shift using table A.1 and table A.2.

Test resonator program

It is a good idea to create a new job file for each layer. Each job can have up to 10 passes, all of which can be automatically exposed with a single pass command '*'. Each pass contains specific exposure times, shutter positions, and pass shifts. In order to create test mechanical resonators, one such series of four jobs has been created and has the prefix MULTI. The individual jobs are:

MULTIBW - exposes generic mechanical resonator base wiring, novel mechanical resonator base wiring and coupling capacitors. The top half of the wafter has 5 patterns, the middle row of the wafer is its own pattern, and the lower half of the wafer has 5 patterns. Coupling capacitors are 10 fF in the top half, shorts in the middle row, and 5 fF in the bottom half.

MULTIVIAS - exposes generic vias.

MULTITW - exposes generic mechanical resonator top wiring and novel mechanical resonator top wiring.

MULTID - exposes novel mechanical resonator define.

A.1.3 Lithography and etches

For completeness, all lithography and etch steps needed to fabricate a mechanical resonator are described here although only two of them were developed specifically for this process. All of the exposes are intentionally overexposed. The mask set was designed with this intentional overexposing in mind. Overexposing ensures that no residue films of photoresist will remain after developing and thus substantially increases yield.

Photoresist processing

Two different thickness of photoresist were used during the fab. The mechanical resonator base wiring uses SPR-955 0.9 microns, while the remaining layers use SPR-955 1.8 microns. Irrespective of the thickness, the resist spinning procedure is always the same. First HMDS micro-primer is spun onto the wafer at 2500 rpm for 30 seconds with a ramp rate of 500 rpm/s. The wafer is then transfered to another spinner and photoresist is spun onto the wafer also at 2500 rpm for 30 seconds. The wafer is then heated on a hotplate for 90 seconds at 90 degrees Celsius. The wafer is then exposed in the stepper. After exposure, another bake is performed at 115 degrees Celsius for 90 seconds in order to set the photoresist. The wafer is then submersed and agitated in AZ 300 MIF for 60 seconds, immediately followed by a 10 second DI dip. The wafer is then rinsed under gently running water and

Step number	1	2	3	4	5
Cl_2 (SCCM)	40.0	40.0	40.0	0.0	0.0
CF_4 (SCCM)	0.0	0.0	0.0	3.2	3.2
Ar (SCCM)	0.0	0.0	0.0	40.0	40.0
Pressure (Pa)	3.0	0.7	0.7	3.0	0.2
Vac time (s)	0.0	0.0	45.0	0.0	45.0
Rf wait (s)	15.0	0.0	0.0	15.0	0.0
SRC FWD (W)	300	300	300	400	400
Bias FWD (W)	0.0	0.0	70	0.0	150
Step time (s)	5.0	5.0	VAR	10.0	VAR

Table A.3: AlN via etch recipe for Panasonic 2, number 152.

blown dry with a nitrogen gun set to a pressure of 15 psi.

Mechanical resonator base wiring

The photoresist is exposed for 0.75 seconds multiplied by a correction factor of 0.35, for an actual exposure time of 0.263 seconds. The wafer is then plasma etched using our standard BCl_3/Cl_2 aluminum etch recipe, which can be found on the Martinis group TWiki page. The etch time depends on the Al thickness but for 130 nm, 30 seconds was used successfully.

AlN vias

The pattern is exposed in the stepper for 1.45*0.35 seconds. It is then etched in Panasonic 2 using recipe 152. This recipe was specifically developed for etching though AlN and stopping on the underlying Al layer. The details of the etch can be found in table A.3. The idea is to remove most, but not all of the AlN layer

with chlorine. Then, the second part of the recipe is just an Ar mill to remove the remaining AlN. CF_4 is added to the mill to promote the formation aluminum fluoride once the mill has eaten into the aluminum layer. The aluminum fluoride acts to protect the aluminum from milling away too quickly. It is difficult to determine the precise etch rate of this process, but it seems that the Cl_2 etch time is proportional to the thickness of the AlN film, and the exact Ar/CF_4 mill time is not essential as long as it is not completely forgone. In practice, the mill time is kept at 7 minutes and the chlorine etch time is adjusted (37 seconds is sufficient chlorine etching time for 300 nm).

Mechanical resonator top wiring

The expose time is increased to 1.6*0.35 seconds because of the underlying layers. The wafer is plasma etched using the standard Al recipe. For the usual thickness of 154 nm, 40 seconds works well.

Mechanical resonator define

After a 1.6*0.35 second exposure the wafer is plasma etched in Panasonic 2 using recipe 152. Although recipe 152 was used earlier to create vias, it this process step it serves a different purpose. Instead of trying to stop on the underlying layers, the intent of this etch is to cut though all the layers, including the SiO_2 wafer oxide. For the usual layer thicknesses, 4 minutes pure Cl_2 etch is barely

adequate to cut though all the layers. The second part of the etch contains CF_4, which etches the SiO_2. The Ar is really not necessary and it may be preferable to remove it. A note of caution here, photoresist is not indestructible so care must be taken not to increase the time of this etch beyond what is absolutely necessary.

A.1.4 Xenon difluoride etcher

When we first set out to make mechanical resonators the UCSB nanofab did not have a xenon difluoride etcher. Instead of waiting for them to acquire one, we decided to build our own. At the time of writing, the xenon difluoride etch is located in Broida Hall room 1310. The computer software was written in Delphi and runs with labRAD server abstraction. The source code can be found on the attached computer, on the CD on top of the computer, as well as on Skynet.

We will briefly describe the typical operation of the etcher. The first step is to vent the etching chamber and load the sample to be etched. Next, pump out the chamber. At this point the chamber should be repeatedly (about 20 times) flushed with nitrogen gas and pumped down to base pressure. This rids the chamber of most of the water vapor, which would otherwise react with the XeF_2 forming HF acid. Once all the pump-purge cycles have finished, the etch is ready to commence.

The etch is carried out by iteratively flooding the etching chamber with xenon difluoride gas, allowing enough time for it to react with exposed silicon, and

pumping the resulting gases out of the etching chamber. Specifically, the machine operates by allowing XeF_2 crystals to sublimate to about four Torr in its vacuum bottle. The valve between this bottle and the expansion chamber is then opened for an amount of time long enough for the expansion chamber to reach the desired pressure. The flow rate of the XeF_2 gas is controlled by a metering valve between the bottle and the expansion chamber. The valve between the bottle and the expansion chamber is then closed and the valve between the He line and the expansion chamber is opened long enough for the expansion chamber pressure to reach the desired total pressure. The He flow rate is controlled by a different metering valve. After the He pneumatic valve has been closed, the valve between the expansion chamber and the etching chamber is opened for the desired etching time. A good rule of thumb is to allow the etch to occur for at least one minute so that most of the XeF_2 gas has been consumed. After the etch time has expired, the gate valve between the expansion and etching chambers is closed and the valve between the etching chamber and pump is opened to pump out the etching chamber. Once the etching chamber has reached an acceptable pressure, the valve between the pump and the etching chamber is closed. This constitutes one etch cycle. This process is repeated as many times as necessary to fully release the device (typically less than 10 times at 3.5 Torr XeF_2 for a few dies). The amount of release can be monitored with the binocular microscope and it may

be more convenient to intentionally enter a value much too large for the number of intended etch cycles and then simply press the "next step" button when the device is sufficiently released.

The sample is now ready to be removed from the etch chamber. However, the chamber should first undergo another pump-purge process to rid it of any remaining xenon difluoride gas. This should be done in a similar fashion to the pre-etch pump-purge, and executed for at least 16 cycles.

A.2 Coupled qubit and mechanical resonator

The Martinis group had previously developed a relatively robust process for creating superconducting phase qubits. Our aim, then, was to combine those tried-and-true steps with those needed to create a mechanical resonator.

A.2.1 L-Edit design

By itself, the mechanical resonator process contains four lithographic steps, and to make qubits by themselves utilizes seven lithographic exposures. Naïvely, it appears as though the FBAR top wiring step could be combined with the base wiring step of the qubit, producing a total of only 10 lithographic patterns. However, it was not possible to use just 10 lithographic patterns because of the difficulties faced when combining the essentially two-dimensional qubit layers with the inher-

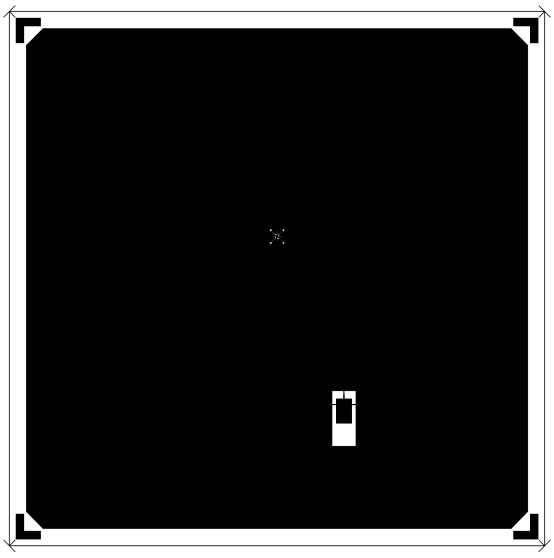

Figure A.8: Generic Mechanical resonator bottom electrode. Black represents the resulting aluminum pattern. The wires lead into mechanical resonator area. The horizontal wires will connect to CPW drive lines, and the vertical wire will lead to a coupling capacitor that is connected to the qubit.

ent three dimensionality of the FBAR. To overcome this issue, it was necessary to add an additional three layers to the process.

Mechanical resonator base wiring

To begin, the mechanical resonator base wiring is broken into two separate designs, the generic leads (Fig. A.8) and a mask containing many possible choices for the FBAR geometry. One particular resonator pattern is shown in Fig. A.9. The horizontal lines will be connected through coupling capacitors to CPWs, which lead to microwave launchers. The idea behind these lines is that they allow for classical transmission measurements to be made to ensure that the co-fabricated

test mechanical resonators perform as expected. In addition, to drive the FBAR directly, even when connected to a qubit, one of these lines may be used. The vertical lead will connect to the qubit coupling capacitor.

Note that the generic pattern is small enough to be combined with another mask plate in order to save space. This could be done with future mask sets. At this point, as a technical aside, it is also worth mentioning that in a given quadrant of the novel mechanical resonator base wiring pattern, there was enough room to include and entirely different pattern. We included patterns for qubit top wiring shunting capacitor and qubit top wiring coupling capacitor. The purposes of these patterns will be mentioned later and they were only included in this quadrant to minimize the total number of masks needed.

Mechanical resonator vias

In order to connect to the mechanical resonator CPW leads, holes need to be made that penetrate through the AlN and stop on the underlying aluminum. These holes are the same for all resonators and are illustrated in Fig. A.10.

Mechanical resonator plasma frame

This is the first of the patterns needed to facilitate the connection between the mechanical resonator and subsequent qubit base wiring. The problem we address with this pattern is that it would very detrimental for qubit performance to create

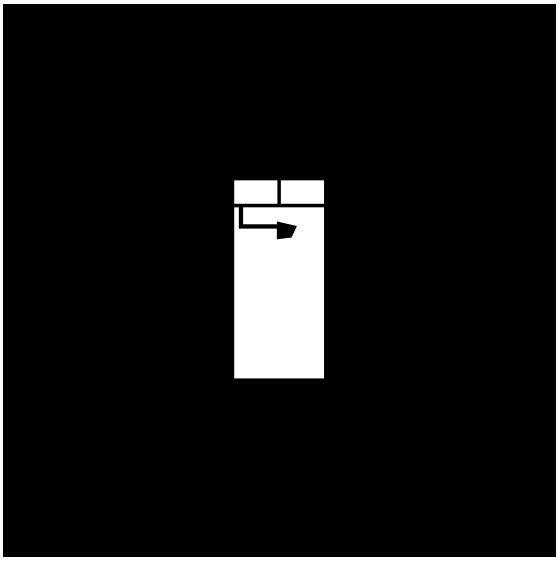

Figure A.9: Expanded view of novel mechanical resonator bottom electrode. One of the possible 36 choices.

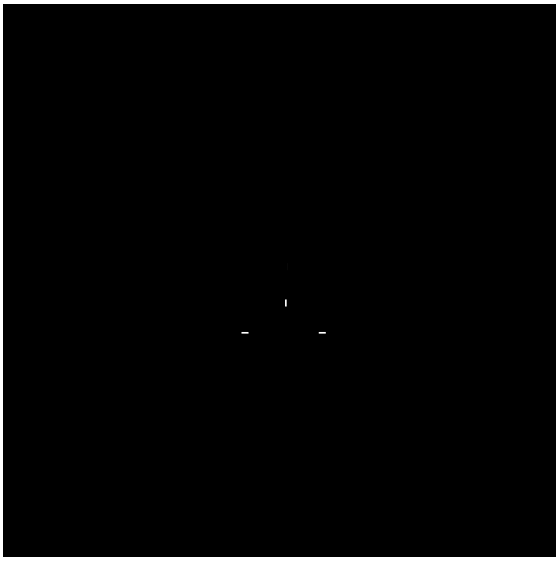

Figure A.10: Generic mechanical resonator vias. White area indicates where the holes will be cut though the AlN layer to facilitate future contact with the mechanical resonator lead wires.

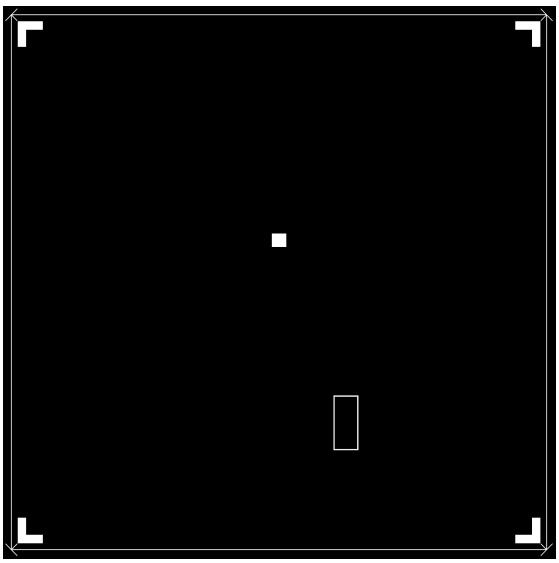

Figure A.11: Generic mechanical resonator plasma frame. The white rectangular picture frame shaped region in the lower right indicates where a plasma etch will cut though all the layers, stopping on the substrate. Using plasma gives vertical sidewalls and good lateral edge dimensions.

it atop an AlN layer. The resulting energy lifetime would most likely be abysmal and it would be difficult to create the small features needed for the junctions. To this end, we would like to remove as much of the AlN as possible. This would be best done using a selective wet etch that isotropically erodes AlN. However such an etch it is not possible at this point.

The reason a wet etch would be detrimental stems from the fact that wet etchants etch laterally as well as vertically. This would most likely destroy the mechanical resonator leads. In addition, any material that still remained would be dramatically undercut. Finally, AlN etches much slower than Al so it would

be impossible to allow the etchant to come in contact with the vias, which are exposed Al, without etching away all the Al. Without etching directly up to the exposed Al of the vias, subsequent wiring layers would have to be deposited over a minimum step height equal to the sum of the thicknesses of the mechanical resonator base wiring and the AlN layer; a step height sufficient to make a reliable connection unlikely.

For the reasons mentioned above, a wet etch was impossible. Inductively coupled plasma, on the other hand, etches anisotropically, creating vertical sidewalls and well defined lateral dimensions. With a plasma etch we can allow the etch to cut into the Al vias without risking their demise and also without substantial undercutting of the pattern. The draw back of plasma etching is that it transfers the vertical topology as it etches. Thus, if the layer to be etched is rough, the stop layer will have a roughness proportional to the etch selectivity.

Since it would be difficult to fabricate a qubit on a rough substrate, we sought a solution that incorporated the good substrate clearing properties of the wet etch with the lateral definition of the plasma etch. The idea was to etch vertical sidewalls in the desired pattern while etching as little of substrate area as possible. Then, in a subsequent step, use a wet etch to clear the rest of the substrate. The pattern shown in Fig. A.11 represents the first of these two steps. It is designed to cut partly into the via and extend just past the edge of the mechanical resonator

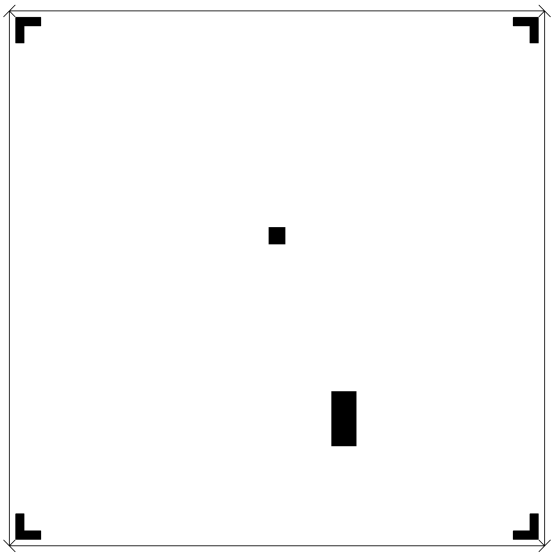

Figure A.12: Generic mechanical resonator wet etch. The rectangular area is sized so that the edge of the pattern extends into, but not past, the area defined in the plasma etch. Any material not protected within this black area will be removed by a wet etch, which selectively stops on the SiO_2 substrate oxide layer.

structure on all sides.

Mechanical resonator wet etch

The second part of the substrate clearing process is carried out using a wet etch. The pattern shown in Fig. A.12 extends into the middle of the etched strip defined with the previous plasma etch. By having the edge of the photoresist pattern extend past the mechanical resonator pattern so that its perimeter rests on the wafer oxide layer, the wet etchant is blocked from laterally etching into the mechanical resonator area. Thus, all of the AlN outside of the region can be removed without affecting the previously defined resonator pattern.

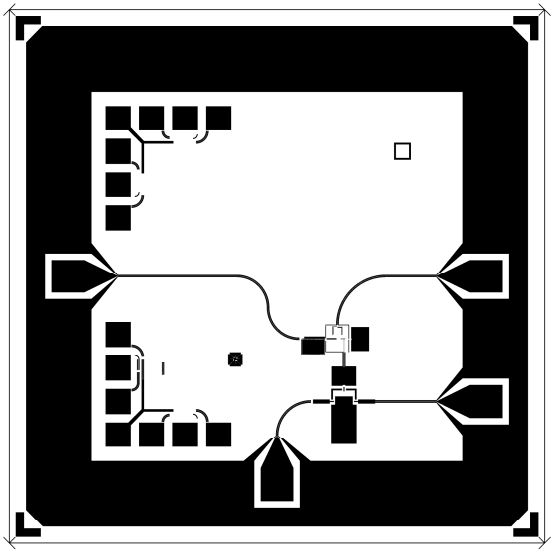

Figure A.13: Generic qubit-mechanical resonator base wiring pattern. Black shapes represent resulting aluminum. Two CPW feed lines leading from the bond pads to the mechanical resonator area are shown in lower right corner. Also illustrated are a CPW originating from the left side of the chip and connecting to the SQUID circuitry, and a CPW feed line originating from the right side of the chip and leading to the qubit flux bias.

Qubit base wiring and mechanical resonator top wiring

These patterns are exposed onto a blanket layer of aluminum that serves as the qubit base wiring, the qubit shunting capacitor base wiring, the coupling capacitor base wiring, the mechanical resonator CPW feed lines, the mechanical resonator external capacitors, and the top electrode of the mechanical resonator. Figure A.13 is a generic pattern showing qubit base wiring. Also shown are the FBAR CPW feed lines and and the qubit CPW feed lines and launchers. The unexposed areas correspond to where the mechanical resonator top electrode, the

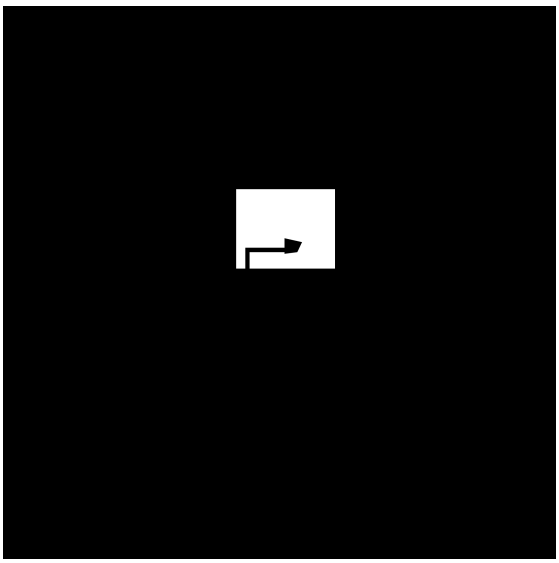

Figure A.14: Expanded view of novel mechanical resonator top electrode. The large area leading off the bottom of the lead leg connects to the chip ground plane.

qubit shunting capacitor, coupling capacitor, and FBAR external capacitors will be subsequently patterned. Figure A.14 shows a novel mechanical resonator top wiring pattern where the wiring extends from the top electrode of the active part of the mechanical structure and terminates at ground.

Mechanical resonator CPW clear

This pattern constitutes the final part of the process needed to connect the mechanical resonator to the qubit base wiring. During the previous step, CPW lines were patterned, which lead from the mechanical resonator to the feed lines and coupling capacitors. However, the underlying area where these CPW lines connect to the mechanical resonator leads will be very rough. This roughness is due to the

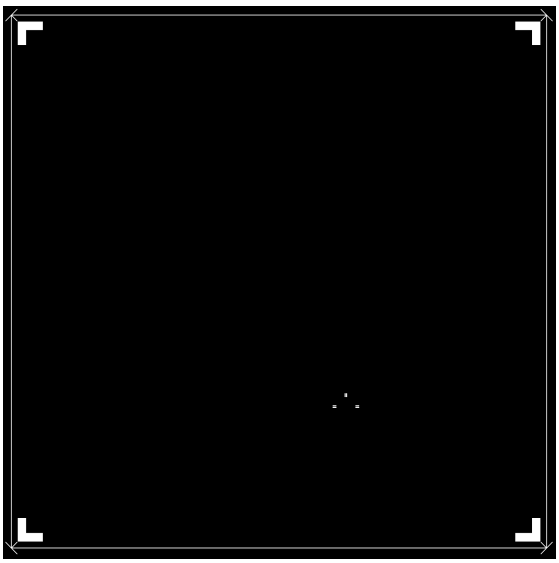

Figure A.15: Generic qubit-mechanical resonator CPW clear. The small white areas represent holes etched on either side of the center strip of CPWs connecting the mechanical resonator to the feed lines and qubit coupling capacitor.

small area which needed to be plasma etched and then covered with photoresist during the wet etch in order to protect against lateral etching.

A subtle processing issue occurs in such situations. The problem arises from of the aluminum oxide layer ubiquitously found on all aluminum surfaces exposed to air. This aluminum oxide layer is much more difficult to etch than aluminum. If the aluminum layer is rough, it will be composed of hills and valleys where their normal direction is not perpendicular to the normal of the wafer. An anisotropic plasma etch, which basically etches downwardly, will see an effectively thicker layer of aluminum oxide wherever the underlying aluminum is sloped. Thus, one etch time will be insufficient to etch both smooth aluminum and rough aluminum

without severely over-etching the flat sections. In the previous step, the aluminum was etched with a time sufficient to remove aluminum from the smooth areas but potentially insufficient to remove all of the aluminum from these small rough areas. If any aluminum has remained unetched in the previous step it could short the center part of the mechanical resonator CPW lines to the ground plane. Thus, the pattern shown in Fig. A.15 was created to allow for these small sections to undergo a wet etch, ensuring that they are free of aluminum. Note that this step is unnecessary if there is no aluminum remaining to short the CPW lines. The amount of remaining aluminum in these areas, if any, was never quantified due to time constraints. This step was done solely as a precaution.

Since this step concludes the connection of the mechanical resonator to the qubit wiring it may be helpful to present a review of the patterns used thus far, and how they come together to form the connection itself. These patterns are presented in Fig. A.16. Figure A.16 **a** shows the mechanical resonator bottom electrode. Figure A.16 **b** represents the vias holes as small black rectangles, **c** shows the resulting area etched by the plasma frame step as a light green region superimposed on existing patterns. Figure A.16 **d** illustrates the area protected by photoresist during the wet etch as a superimposed gray area. Figure A.16 **e** shows, in solid gold, the pattern of the remaining aluminum after the qubit base wiring step. Note that the coupling capacitors are not illustrated. Finally, **f**

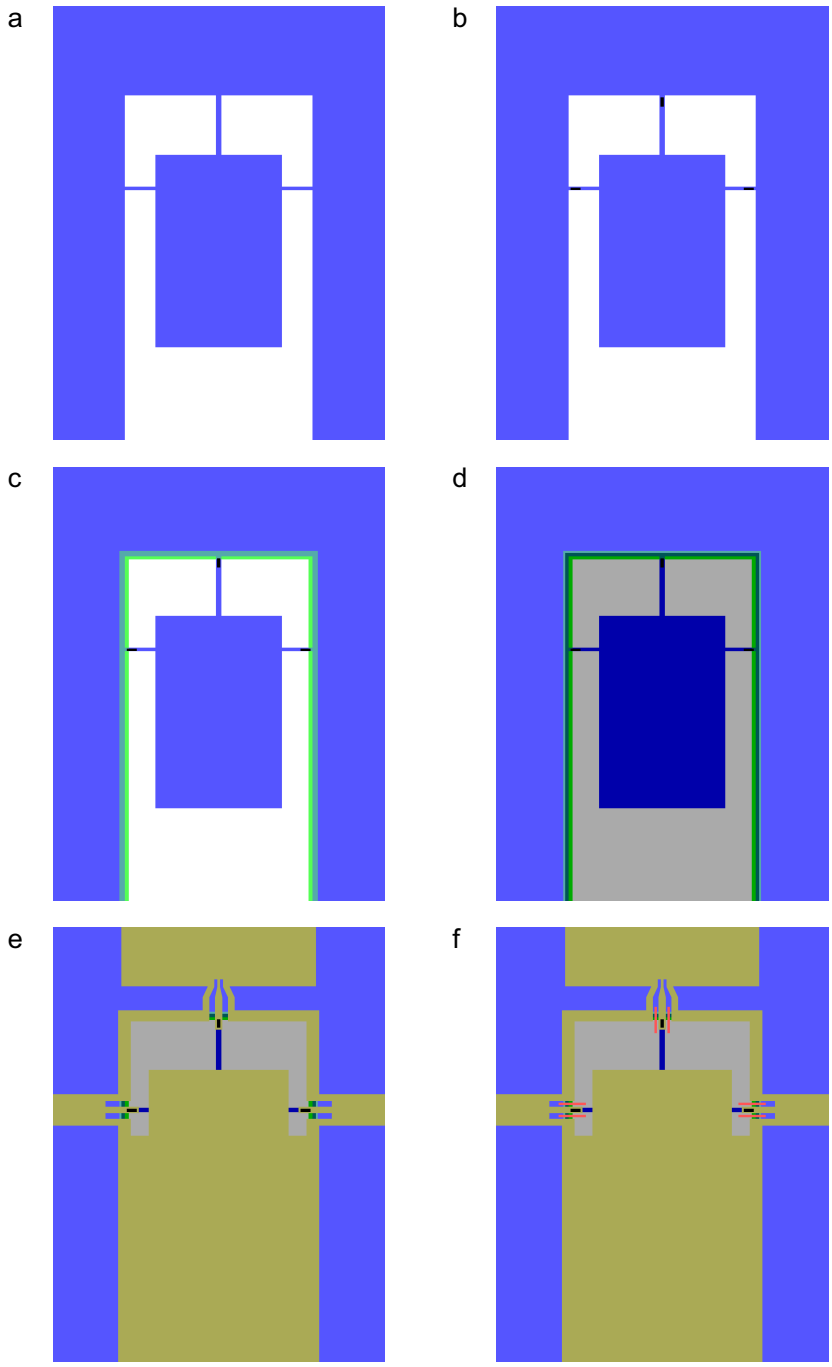

Figure A.16: All layers involved in the connection between mechanical resonator and CPWs.

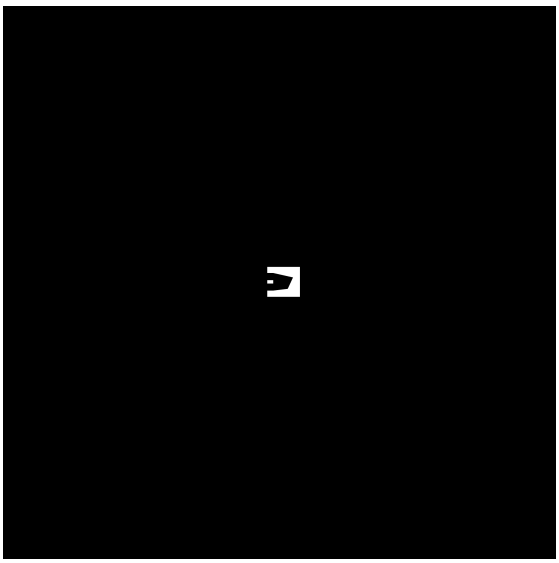

Figure A.17: Expanded view of mechanical resonator define. Black pattern indicates protected area and is slightly smaller than existing shape of the mechanical resonator. After etching, this pattern will define the shape of the mechanical resonator.

indicates, in red, the small rectangular region of the CPW to be wet etched and cleared of unwanted aluminum.

Mechanical resonator define

The novel pattern shown in Fig. A.17 defines the shape of the resulting mechanical resonator structure in the usual fashion. As an aside, it should be noted that the result of etching this pattern will create an object with height being the sum of the mechanical resonator base wiring, AlN, and mechanical resonator top wiring thicknesses. Usually this height is approximately 750 nanometers, which is quite a large step height. Step heights this large can cause fabrication problems

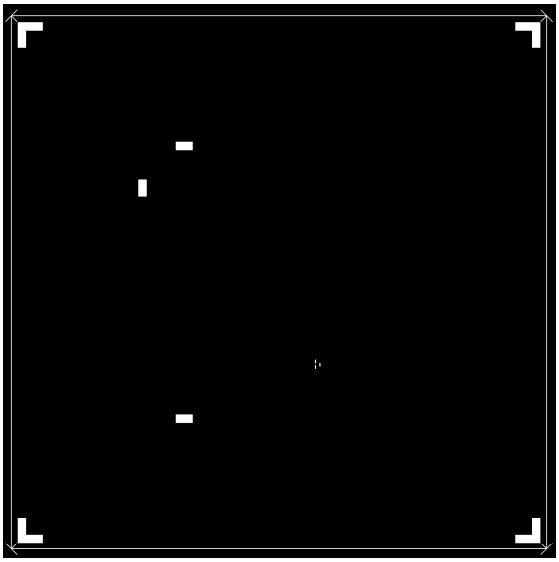

Figure A.18: Generic junction area clear. White ares are holes where the amorphous silicon will be cleared to allow the junction trilayer to be formed on the substrate.

such as insufficient photoresist coverage or streaking, nearly vertical features of subsequently sputter deposited metal layers, or inadequate dielectric coverage.

Junction area clear

The performance of the resulting mechanical resonator relies on the ability to release the structure from the substrate. With this in mind the substrate was specifically chosen to be silicon, a material that etches selectively over aluminum and aluminum oxide when exposed to XeF_2 gas. This, however is not the conventional choice for a qubit substrate. Usually, qubits are fabricated on single crystal sapphire substrates because of their low dielectric loss and high etch selectivity.

At this point in the fabrication process, the Martinis group customarily combines two ideas into one lithography step. The first idea is to etch vias through the hydrogenated amorphous silicon and stop on the underlying aluminum layer. The second idea is to remove all of the amorphous silicon from a small area of the substrate in order to subsequently create the qubit junction in an amorphous silicon free area. However, the conventional plasma etch for this step contains CF_4 which also readily etches SiO_2, the oxide layer of our silicon substrate. We do not wish to penetrate this oxide layer unnecessarily. This oxide layer will later help protect the silicon substrate from being etched away when the entire chip is exposed to xenon difluoride gas.

To selectively etch amorphous silicon while leaving the SiO_2 layer, thus avoiding future problems, a pure chlorine plasma may be used. However, it is impossible to use this etch for both of the purposes described above, because chlorine etches aluminum. These considerations forced us to break the two ideas into two different lithographic steps. The first of these patterns is illustrated in Fig. A.18 and generically clears the area of amorphous silicon in order to subsequently form junctions.

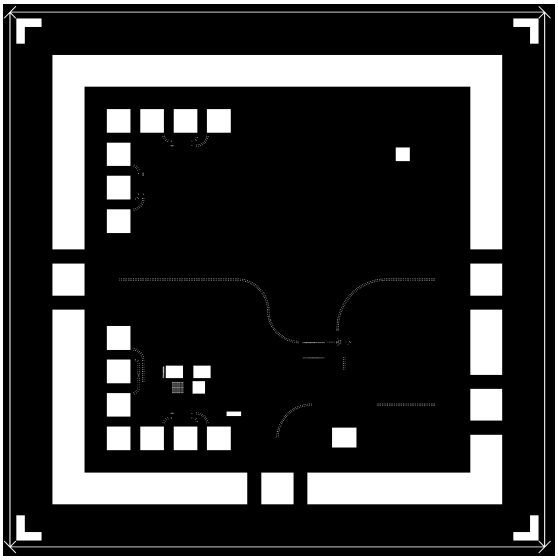

Figure A.19: Generic qubit and wiring vias. White areas are holes where the amorphous silicon hydride will be removed to allow connection of subsequent aluminum layers to the base wiring.

Wiring vias

The second of the amorphous silicon generic etching steps is shown in Fig. A.19 and acts to create holes in the amorphous silicon that lead to the underlying base wiring.

Junction gap

The pattern used to open up small holes in the blanket aluminum layer is barely visible in Fig. A.20. The purpose of these holes is to define a step edge where the overlap junctions can be formed.

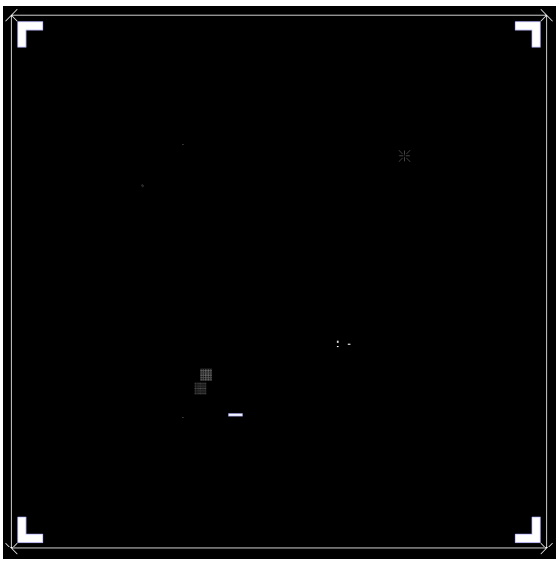

Figure A.20: Generic junction holes. Small white rectangles represent holes through the aluminum layer needed to create a nonconducting area over which a junction will be subsequently formed.

Overlap junction

The overlap junction triangular shape is barely visible as the small dark spots in Fig. A.21. This is the standard overlap junction pattern used in the Martinis group, so a detailed discussion will not be presented here.

Qubit top wiring

The generic pattern shown in Fig. A.22 is composed of qubit top wiring, squid capacitor top wiring, jumpers for the CPW lines, and extra aluminum rectangles that prove to be useful when bonding. Not shown are the novel patterns used to from the qubit shunting capacitor and coupling capacitor top wiring. One

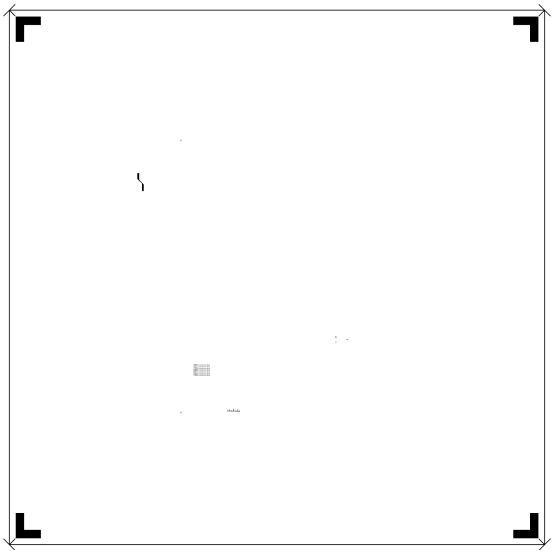

Figure A.21: Generic overlap junctions. Small black patterns indicate remaining aluminum atop the aluminum oxide, bridging the junction gap.

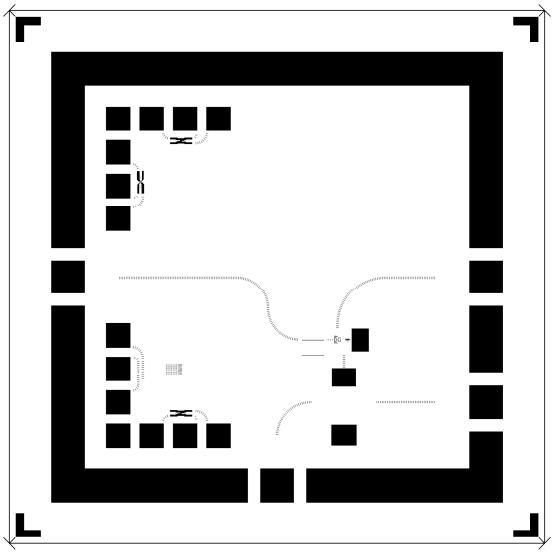

Figure A.22: Generic qubit top wiring. Black area represents the resulting aluminum pattern, which serves as the top wiring of the qubit, jumpers that keep the ground plane connected across the CPWs, and bond pads.

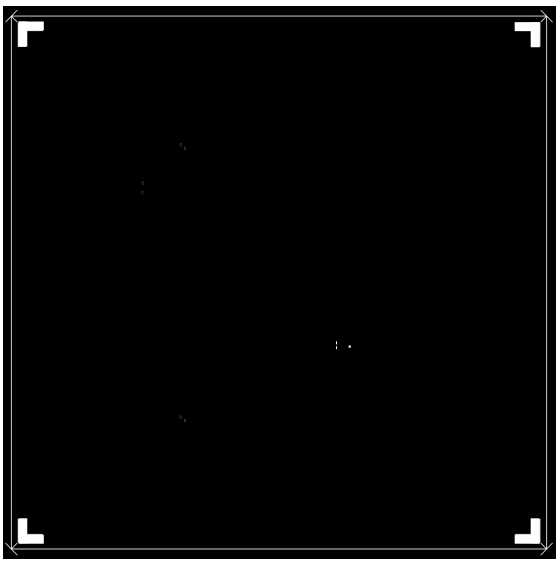

Figure A.23: Generic qubit shorting strap removal. When the small white rectangles are exposed, they create holes in the photoresist. When the wafer is immersed in aluminum etchant, the electrical connections between the junctions and the ground plane are severed.

possibly useful feature of this pattern is illustrated as the black rectangle at the bottom of the mechanical resonator area of the chip. This aluminum pad can be used to directly wire bond the ground of the mechanical resonator to the chip ground, although a wire bond of this type was not used in the previously described experiment.

Shorting strap removal

The junctions must remain shorted to ground during plasma etches or the tend to short. The generic pattern, shown in Fig. A.23, is used to expose those areas to a wet etch in order to remove the shorting straps. Also involved in the wet

etch, but not illustrated here, is a novel pattern similar in shape to the one used when defining the shape of the mechanical resonators. The only difference is that is covers a slightly smaller area of the mechanical resonator. This pattern is designed to be a slightly smaller size in order to allow the sidewalls of the FBAR to be wet etched. Any aluminum that may be coating these walls, shorting the stack, will be removed in the wet etch. Note that this novel pattern is not necessary if there is no aluminum coating the sidewalls of the mechanical resonator. Due to time constraints the amount of aluminum shorting the sidewalls, if any, was never quantified. This pattern was always used, but only as a precaution.

A.2.2 Stepper program

The stepper programs required for this process were substantially more complex than those needed to create mechanical resonators alone. In all, five different mask plates were used. They are labeled A through E. The patterns on each of the plates are:

Mask A - FBAR base wiring generic, FBAR vias generic, FBAR plasma generic (not used), FBAR wet etch generic, also 10fF FBAR drive line external capacitors

Mask B - qubit base wiring generic, qubit vias generic, junction vias generic, junction gap generic, also 2.1, 1.1, 0.5 0.3 fF FBAR drive line external capacitors

Mask C - junctions generic, qubit top wiring generic, SiN removal generic (not

used), shorting strap removal generic

Mask D - FBAR base wiring and coupling capacitor/qubit capacitor top wiring novel, FBAR plasma frame generic, coupling capacitor/qubit capacitor base wiring novel, FBAR define and coupling capacitor/qubit capacitor vias novel. Note that most of this mask, except for the plasma frame pattern, goes unused because it was succeeded by Mask E.

Mask E - FBAR base wiring and coupling capacitor/qubit capacitor top wiring novel; FBAR top wiring, coupling capacitor/qubit capacitor base wiring, and FBAR CPW clear; FBAR define and coupling capacitor/qubit capacitor vias; shorting strap and FBAR sidewall Al removal.

There are a total of 14 job files that utilize these masks to create the coupled sample:

2MRBW - masks A and E: Mask A contains the generic mechanical resonator patterns. This job exposes the base wiring. Mask E houses all of the novel patterns. Columns 1-2 and 13-14 are membrane type resonators, columns 3 and 12 are extended leg geometry, columns 4-5 and 10-11 have rounded features, and columns 6-9 have wingtip leg overlap. The geometric capacitance of all the mechanical resonators is roughly 0.2 pF.

2MRVIAS - mask A: generic FBAR via pattern on every die.

2MRPF - mask D: generic plasma frame pattern.

2MRWET - mask A: FBAR wet etch pattern.

2MRTW and 2QBW are exposed onto the same photoresist. 2MRTW - mask E: novel FBAR top wiring. 2QBW - masks A and B: generic qubit base wiring; novel coupling capacitor/qubit capacitor base wiring and FBAR external capacitors. Columns 1-7 1.0 pF coupling capacitor, columns 8-14 0.5 pF coupling capacitor. Columns 1-3 0.74 pF qubit shunting capacitor. Columns 4-14 0.98 pF qubit shunting capacitor.

2MRFU - mask E: generic FBAR CPW clear

2MRD - mask D: novel FBAR define. Note: mask E may be used here instead of D.

2QJVIAS - mask B: generic junction vias.

2QVIAS - masks B and D: generic qubit vias and novel coupling capacitor/qubit capacitor vias.

2QHOLE - mask B: generic junction gap

2QJ - mask C: overlap junction pattern. Rows 1-3 300 nm larger, rows 4-5 150 nm larger, rows 6-9 no pass shift, rows 10-11 150 nm smaller, rows 12-14 300 nm smaller.

2QTW - masks C and E: generic qubit top wiring and novel coupling capacitor/qubit capacitor top wiring.

2QSS - masks C and E: generic qubit shorting strap removal and novel FBAR

sidewall Al removal.

A.2.3 Lithography and etches

In this section we describe all of the necessary exposures and etches in order to create the coupled sample. Many of these etches and exposure techniques were developed by the Martinis group, but they are all listed below for completeness.

Photoresist processing

Two thicknesses of photoresist were used, SPR-955 0.9 micron and SPR-955 1.8 micron. Independent of which resist was used, the wafer was always primed with HMDS for 30 seconds at 2500 rpm with a ramp rate of 500 rpm/s. The wafer was then moved to a different spinner and the photoresist applied and spun in the same way. Following the spinning, the wafer was baked for 90 seconds at 90 degrees Celsius. Following each exposure, a resist hardening bake was performed at 115 degrees Celsius for 90 seconds. The developing procedure of first immersing and agitating the wafer in AZ 300 MIF for 60 seconds, then dunking the wafer in DI water for 10 seconds, followed by a flowing water rise and nitrogen gun blow dry at 15 psi was a standard procedure for most of the layers. However, there were two exceptions. The developing time was reduced to 45 seconds, the flowing water rise was forgone, and the nitrogen gun pressure was dropped to about 5 psi for the

qubit base wiring and mechanical resonator top wiring step. This was to ensure that the one micron lines of the interdigitated capacitors would come out more reliably. The second exception was that the qubit top wiring was only developed for 55 seconds, the ideal developing time (60 seconds is actually an overdevelop)

Mechanical resonator base wiring

Using 0.9 micron photoresist, both the generic and novel FBAR base wiring patters were exposed for 0.75*0.35 seconds, which is a significant overexposure. The pattern was then plasma etched in Panasonic 2 using the Martinis group standard aluminum plasma etch for 30 seconds.

Mechanical resonator vias

The mechanical resonator pattern was exposed onto 1.8 micron photoresist for 1.45*0.35 seconds. The wafer was then etched using the AlN via etch previously described (recipe number 152 on Panasonic 2) for 36 seconds with chlorine and 7 minutes with the CF_4/Ar mill.

Mechanical resonator plasma frame

The plasma frame pattern was overexposed for a time of 1.6*0.35 seconds, transferring the design to 1.8 micron resist. A pure chlorine etch was developed to remove the unwanted Al and AlN material while stopping on the silcon dioxide

Step number	1	2	3
Cl_2 (SCCM)	40.0	40.0	40.0
Pressure (Pa)	1.0	0.7	0.7
Vac time (s)	0.0	0.0	45.0
Rf wait (s)	15.0	0.0	0.0
SRC FWD (W)	300	300	300
Bias FWD (W)	0.0	0.0	70
Step time (s)	5.0	5.0	VAR

Table A.4: Plasma frame etch recipe for Panasonic 2, number 160.

substrate layer. This etch has the same parameters as the first three steps of the AlN via etch. The plasma frame recipe is number 160 on Panasonic 2 and has the parameters denoted in table A.4. The etch was performed for 3 minutes.

Mechanical resonator wet etch

The wafer was exposed for 1.6*0.35 seconds using 1.8 micron photoresist. The wafer was then submersed in Transene Al etchant "Type A", which had been allowed to equilibrate to a programmed hotplate temperature of 75 degrees Celsius (the actual temperate of the bath is lower). The wafer was suspended with the pattern facing upward to allow for visual monitoring of the etch. The wafer was agitated periodically for 22 minutes. A note about this etch, it may seem as though most of the AlN is removed after a few minutes. However, there remains a white milky film across the entire wafer. Allowing the wafer to remain in the bath for the remainder of the etch time allows that layer to be broken off and

dissolved. It is important to carry out the full length of this etch to ensure the resulting roughness is minimized.

Qubit base wiring and mechanical resonator top wiring

There are two different exposure times for this step. For the qubit base wiring, qubit shunting capacitor, and qubit/FBAR coupling capacitor, a 0.62*0.35 second exposure was used to imprint the pattern into 0.9 micron photoresist. This time would be a slight over exposure for a standard develop time, but with the special 45 second develop time used for this step, it is the ideal exposure time. The mechanical resonator top wiring was exposed for 1.8*0.35 seconds, a gross overexposure. The pattern was then etched using the standard Martinis group Al recipe for 40 seconds.

Mechanical resonator CPW clear

With a photoresist thickness of 0.9 microns, the 1.0*0.35 second exposure is definitely long enough to fully transfer the CPW clear pattern. A hotplate temperature was set to 80 degrees Celsius and the bath allowed to equilibrate for at least half of an hour. The wafer was then submersed and agitated in Transene aluminum etchant Type A for one minute.

Step number	1	2	3
Cl_2 (SCCM)	8.0	8.0	8.0
Pressure (Pa)	1.0	1.2	1.2
Vac time (s)	0.0	0.0	15.0
Rf wait (s)	15.0	0.0	0.0
SRC FWD (W)	500	400	400
Bias FWD (W)	0.0	0.0	40
Step time (s)	5.0	10.0	VAR

Table A.5: Junction clear etch recipe for Panasonic 2, number 158.

Mechanical resonator define

The thicker, 1.8 micron, photoresist was used to ensure the plasma etch would not accidentally penetrate the resist. The pattern was overexposed for 1.6*0.35 seconds before being plasma etched using recipe number 152 with a 4 minute chlorine time and 9 minute CF_4/Ar mill.

Junction area clear

The pattern was transfered to 1.8 micron photoresist using a 2.0*0.35 second exposure time, a time much longer than likely necessary. The wafer was then etched in Panasonic 2 using a pure chlorine plasma etch recipe specifically developed for this step for a time of 2 minutes and 56 seconds. The number of the recipe is 158 on Panasonic 2 and is documented in table A.5. This recipe was designed to use chlorine because it has little effect on silicon dioxide but etches amorphous silicon relatively rapidly.

Wiring vias

The thicker resist was used for this step with an exposure time of 2.0*0.35 seconds. The wafer was then etched using the standard Martinis group amorphous silicon etch recipe for 2 minutes and 40 seconds. This recipe has been previously documented and can be found on the Martinis group TWiki.

Junction gap

The pattern was transfered to 0.9 micron photoresist using a 1.0*0.35 second exposure. The thinner resist was used to attempt to produce better pattern definition, although a 1.0*0.35 second exposure is a substantial overexposure and smears out the edges of the resulting pattern. The wafer was etched in Panasonic 2 using the standard Martinis group aluminum etch for 49 seconds.

Overlap junction

The overlap junction pattern was exposed for 0.8*0.35 seconds onto 0.9 micron photoresist. The pattern was then milled in Panasonic 1 using the standard Martinis group junction chlorine/argon mill. The parameters for this mill can be found on the Martinis group TWiki. The wafer was milled a total of five times: four times for 53 seconds and once for an additional 18 seconds.

Qubit top wiring

The 0.9 micron photoresist was exposed for 0.85*0.35 seconds. The wafer was then etched in Panasonic 2 for 49 seconds using the standard Martinis group aluminum recipe.

Shorting strap removal

Finally, 1.8 micron photo resist was used for the shorting strap removal pattern, which was exposed for 1.6*0.35 seconds. The wafer was then immersed and agitated in Trasene aluminum etchant Type A for 30 seconds. The bath had been allowed to equilibrate to a programmed hotplate temperate of 80 degrees Celsius.

A.3 Tips and tricks

This section contains some useful concepts and techniques that were used to create the coupled qubit and mechanical resonator sample. Unfortunately, successful fabrication cannot be learned from reading about proper techniques. There are many very subtle aspects of a clean fabrication that are difficult to describe.

A.3.1 Spinning photoresist

We shall begin with photoresist spinning. It is standard procedure to change spinners between HMDS application and the spinning of photoresist. Although

this technique has been used for the fabrication described above, it may not be necessary to switch spinners. When performing tests to this end, it was seen that if thirty seconds were allowed to elapse between spinning HMDS and photoresist, then no problems emerged as long as an excessive amount of HMDS was not used.

A.3.2 Stepper alignment

Using the stepper can be frustrating because it is quite tricky to operate properly. The alignment aspect of the process can be made much easier if great care is taken when aligning the wafer to the chuck, and subsequently, the chuck to the stage. One way to ensure a good wafer to chuck alignment is to rest the flat of the wafer against the bottom two pins while ensuring that it does not touch the left pin. By gently rocking the wafer back and forth it can be seen that the wafer is resting squarely on the bottom pins. Once the wafer is flush with those pins, slide the wafer to the left until it touches the left pin. Repeat the rocking and sliding procedure until the wafer is resting flush with respect to all three pins. The rule of thumb here is that if is possible to still rock the wafer to the left, then it is not flush with all three pins. Once the wafer is in place, carefully engage the chuck vacuum. Then slide the chuck onto the stage and engage the stage vacuum. At this point it is still possible to move the chuck with respect to the stage because the vacuum seal is sufficiently weak. To ensure reproducible

chuck to stage alignment, rotate the chuck handle counterclockwise then back into position. The chuck should now be aligned with the two alignment posts of the stage. If this procedure is carefully done every time, the alignment mark should never be off by more than 100 microns when first viewing the alignment screen.

A.3.3 Using the Unaxis properly

Depositing amorphous silicon in the Unaxis ICP PECVD system is always unreliable. To help minimize errors, one should fabricate on a wafer size expected by the Unaxis, namely a 100 mm wafer. As a side note, processing on a 100 mm wafer produces almost twice the number of devices as processing on a three inch wafer.

A.3.4 Plasma etching in the Panasonic

Etching in the Panasonic is quite tricky. The difficulty arises because the Panasonic is designed to process six inch wafers. Since the other machines in the cleanroom, the Unaxis for example, are incapable of handling six inch wafers, then necessarily the Panasonic is the odd-man-out. Thus, a smaller size wafer must be mounted on a six inch carrier wafer in order to be processed in the Panasonic. Mounting to the six inch carrier wafer is difficult because it involves sticking the wafer to be processed to the carrier wafer using pump oil. This pump oil secures

the wafers together and also creates a thermal connection between the two. Too little pump oil and good thermal contact is not made. Too much pump oil and it will come out the sides when first placed in vacuum. The pump oil will then be sprayed all over the wafer by the plasma. Also, if the wafer is only barely stuck to the carrier wafer, when the two are loaded into the Panasonic, movement by the robotic arms may jostle the wafers apart.

The procedure for properly applying pump oil to the carrier wafer is as follows: First, get a wooden handled cotton swab. Obtain an eyedropper full of pump oil. Squeeze the pump oil out of the eye dropper and onto the end of the wooden handle of the cotton swab. A medium sized drop is sufficient. Take the wooden handle with the pump oil and quickly dab it in the center of the carrier wafer to transfer part of the oil. Dab the remaining pump oil left on the wooden handle in six equally spaced locations radially, about one inch from center. Place the wafer to be etched on top the carrier wafer. Take the tweezers and find an open spot in the center of the wafer. Press firmly with the tweezers and try to gently move the wafer in a circle with respect to the carrier wafer. This should be possible at first and then become hard to move as the pump oil is distributed.

Then, take tweezers and the back end of a razor blade and press the wafer down simultaneously on opposing sides of the circumference of the wafer to be processed. Next, use the razor blade to block the carrier wafer from sliding with

respect to the clean wipe by placing it as a stopping point on the clean wipe just outside the carrier wafer. Take the tweezers and gently slide the wafer to be processed toward the razor blade by catching the tweezers on the edge of the wafer to be processed. Try not to scratch the carrier wafer too badly. By sliding the wafers with respect to each other, the oil becomes distributed in that direction. Slide the wafer to be processed back to the center of the carrier wafer by moving the razor and tweezer to their respective antipodal positions and sliding the wafer with the tweezers. Rotate the position of the tweezers and razor blade by 90 degrees and repeat the process described from the beginning of this paragraph. After about four repetitions the oil will be uniformly distributed and the wafers will become very difficult to move with respect to each other. The wafers are now adequately attached.

The final tip for plasma etching is to encourage the practice of watching the sample in the load lock when it is first loaded into that chamber. At this time, the robotic arm rotates the carrier wafer by 180 degrees. If the wafer to be processed rotates with respect to the carrier wafer then it is a sure sign that the mounting procedure was improperly done. The process should be immediately stopped and the sample removed and remounted. This is always a good check to do although there is rarely a problem once the art of attaching the wafers together has been mastered.

A.3.5 Etching aluminum

To create micron or smaller aluminum features, it is necessary to soak the wafer in water immediately after the plasma etch. It has been found that a ten minute soak time increases feature sharpness by passivating any residual chlorine, thus preventing the chlorine from etching laterally into the aluminum, creating what looks like bites taken out of the traces. For trace sizes larger than a micron a five minute water soak should be sufficient. Note that water does slowly etch aluminum so if one is attempting to produce trace widths of just a few nanometers, this technique may etch through those lines.

A.3.6 Microscope dark field

It is highly recommended to examine the wafer after every step in both regular illumination and the dark field setting on the microscope. Height information becomes obvious only in the dark field setting. To become acclimated with using the dark field setting, try comparing dark field images with atomic force microscopy data taken for the same device. By only looking at a film in an optical microscope it is possible to get a good estimate of the film roughness.

A.3.7 Viewing undeveloped photoresist

Developing photoresist on aluminum or AlN layers should only be done once it is verified that the pattern has been exposed correctly. If there has been an error and the pattern must be shot again then some non negligible amount of the aluminum or AlN has been etched away by the developer. This can cause future unforeseen problems and should be avoided. Fortunately, there is an easy solution. Ensure that the pattern has been correctly exposed before developing by examining it under the optical microscope with the GIF filter and polarizer in place. If the aperture, luminosity, and polarization angle are adjusted properly, then the exposed areas of the photoresist should be clearly visible without developing.

A.3.8 Removing photoresist

This technique was developed in response to the AlN via plasma etch recipe, which involves a 7 minute CF_4/Ar mill. This mill heats the wafer quite substantially and greatly hardens the photoresist. Simply sonicating the wafer in acetone at any power proved unable to fully remove the hardened photoresist. However, by adding a directed acetone spray to the middle and end of the standard procedure, full removal of the photoresist was observed. The details are as follows: First, sonicate the wafer in the tabletop device for four minutes at the usual power. Then, remove the wafer from the bath while spraying it with acetone. While

ensuring that the wafer never dries, spray every die with an acetone spray bottle. If there are pieces of photoresist remaining on the wafer they will produce a wake in the acetone stream. Target those pieces with the acetone, spraying until they are removed. When satisfied, sonicate the wafer for another minute and repeat the acetone spraying procedure. At this point all of the photoresist should be gone but if there are still remaining pieces, target them with the spray and then repeat the one minute sonication step. When the wafer looks clean, switch to spraying it with IPA and spin dry. Implementing this photoresist procedure had dramatic results on the final cleanliness of the devices.